PORTABLE MULTIMODAL MICROSCOPY FOR QUANTITATIVE MALARIA DIAGNOSIS AND MONITORING AT THE POINT OF CARE

A Dissertation

by

PAUL DAVID GORDON

Submitted to the Office of Graduate and Professional Studies of
Texas A&M University
in partial fulfillment of the requirements for the degree of

DOCTOR OF PHILOSOPHY

Chair of Committee,	Gerard L. Coté
Committee Members,	Kristen Maitland
	Alexandra Walsh
	Susanne U. Mertens-Talcott
Head of Department,	Michael J. McShane

May 2021

Major Subject: Biomedical Engineering

ABSTRACT

Malaria is a parasitic disease that affects millions around the globe annually and is one of the greatest public health challenges in human history. While much has been accomplished towards eradication of the disease, numerous challenges such as novel drug resistances underscore the need for improved diagnostic and monitoring technologies, especially for use in remote locations without existing healthcare infrastructure. This work proposes that a portable multimodal microscopy system may provide an effective tool to provide better diagnostic information and improve drug resistance monitoring efforts at the point-of-care. To accomplish this, two portable microscope prototypes were constructed that leverage combinations of brightfield, fluorescence, and cross-polarized imaging to provide information that may facilitate such advances.

Sample preparation techniques were improved by optimizing microfluidic smear-generating cartridges for use with the portable microscopy system. These optimizations included the replacement of 1-millimeter thick slide glass substrates with 0.25-millimeter thick polycarbonate sheet material and the development of a one-step, in-tube fluorescence staining procedure. Polycarbonate was verified as a viable cartridge substrate by confirming its thermal stability, optical properties, and bonding potential throughout the manufacturing process. In-tube staining using Acridine Orange was shown to allow *Plasmodium falciparum* parasites to be distinguished from red blood cells and background when imaged in microfluidic smears.

A novel aspheric lens fabrication technique was developed during the course of microscope development that leverages principles of fluid dynamics to create an exceptionally smooth concave parabolic surface in spinning polymers. When cured, it is possible to create plano-concave, plano-convex, and meniscus parabolic polymer lenses with infinitely variable radii of curvature. The theory and characterization of these lenses were explored along with the merits and drawbacks of the manufacturing technique.

Two prototype portable microscopes were constructed, with the first utilizing a tri-modal brightfield, fluorescence, and cross-polarized approach to image malarial parasites in thin blood smears. The device can interface with a range of portable electronic devices. The microscope successfully resolved red blood cells using brightfield imaging, parasites using fluorescence imaging, and the malarial pigment hemozoin using cross-polarized imaging. It was eventually determined that cross-polarized imaging had little diagnostic or monitoring utility, and the modality was removed from the second-generation portable microscope. The second-generation microscope was optimized to utilize low-cost optical components to quantitatively measure parasitemia in thin blood smears. It is hypothesized that drug resistance monitoring may be possible at the point-of-care by using these measurements to calculate parasite clearance rates from the blood after treatment. The microscope was successful in achieving a linear correlation between its parasitemia measurements and those from a benchtop microscope with $R^2 = 0.939$ and a limit of detection of 0.2 parasites per 100 red blood cells. These results indicate that the microscope is capable of quantitatively measuring parasitemia using thin blood smears, and further testing may prove it to be useful for *in vivo* data collection in remote locations.

DEDICATION

To my family.

ACKNOWLEDGEMENTS

First and foremost, I would like to thank my committee chair, Dr. Gerard Coté, for allowing me to join the OBSL to complete my Ph.D. Thank you for supporting, mentoring, and challenging me and for the chance to pursue and develop my passion for global healthcare. I hope to emulate your diligence, professionalism, and conduct in my own career, and I couldn't have asked for a better advisor for my graduate studies.

Thanks also to my committee members, Dr. Kristen Maitland, Dr. Susanne Talcott, Dr. Javier Jo, and Dr. Alexandra Walsh, for your advice and support along the way.

Thank you to Dr. Mary McDougall for being an excellent mentor-teacher and a superb compatriot throughout the great COVID Craziness that was spring semester 2020.

Thank you to Dr. Vikram Kinra for leading the Graduate Teaching Fellowship program and for your refreshing bluntness in asking us all tough questions during lunch.

Thank you especially to all of my friends in the OBSL, SPIE, and department, for being encouraging, for making me laugh, for covering my desk with wrapping paper, and for just being excellent people. I couldn't have made it through without you all.

Thanks to the McCutcheons, Joe Leier, and everyone else for starting me down this path back in 2013, for sharing your lives, and for modeling selfless love.

Thank you to my friends, who have challenged my perspectives, asked me hard questions, loved me unconditionally, and encouraged me to take risks.

And, most of all, thank you to my wife, Amanda, for your unwavering support, encouragement, and smile, no matter how things were going. Because it is ***our*** Ph.D.

CONTRIBUTORS AND FUNDING SOURCES

This work was supervised by a dissertation committee consisting of Dr. Gerard Coté (chair), Dr. Kristen Maitland and Dr. Alexandra Walsh of the Department of Biomedical Engineering and Dr. Susanne U. Mertens-Talcott of the Department of Nutrition and Food Sciences.

Additional contributions to make this work possible were provided by: Dr. Serge Dogbevi, for the design and creation of microfluidic channels to create thin smears and for contributing towards the in-tube staining studies. McCrae Wattinger, for initiation of the rapid lens prototyping project, development of mathematical models, and iteration of the manufacturing methodology. Masih Ghorayshi, for assisting in the development of cell staining techniques. Kimberly Branan, for contributions to microfluidic cartridge construction, the modification of substrate materials, and cell staining experimentation. Vinicius Venancio, for growing *Plasmodium* cultures and for guidance regarding malarial infections and important experimental techniques. Kevin Kiefer, Courtney De Ville, Taila Kawano, and the Talcott lab group for the essential growth of *Plasmodium* cultures. Cody Lewis and Richard Horner, for their assistance in developing control mechanisms and software for the prototype microscope systems. Ibukunoluwa Falana and Amanda Gibbens, for their assistance with literature review and conducting microscopy and microfluidic smear experiments. Dr. Cody Chalker and the Batteas lab group, for facilitating AFM surface roughness measurements of polymeric lenses and experiments to test the feasibility of metal surface deposition to create mirrored surfaces. Dr. Tomasz

Tkaczyk, Dr. Michal Pawlowski, and Gregory Berglund of Rice University, for their support in collecting interferometric lens measurements. Dr. Wayne Hung, for his assistance in profiling polymeric lenses on short notice.

All other work for this dissertation was completed independently by the student.

Funding was provided in part by a Texas A&M College of Engineering Graduate Merit Fellowship and the National Science Foundation; Award no(s). 1402846, 1648451, 2017240275; Funder ID https://doi.org/10.13039/100000001.

NOMENCLATURE

ACT	Artemisinin Combination Therapy
AFM	Atomic Force Microscopy
AO	Acridine Orange
BF	Brightfield
FL	Fluorescence
LMT	Liquid Mirror Telescope
NA	Numerical Aperture
PCR	Polymerase Chain Reaction
PDMS	Poly(dimethylsiloxane)
*pf*HRP2	*Plasmodium falciparum* histidine-rich protein II
PID	Proportional, Integrative, and Derivative
*p*LDH	*Plasmodium* Lactate Dehydrogenase
POC	Point of Care
PSF	Point Spread Function
RDT	Rapid Diagnostic Test
RBC	Red Blood Cell
R_{curv}	Radius of Curvature
RMS	Root-Mean-Square
USAFT	United States Air-Force Target
WHO	World Health Organization

TABLE OF CONTENTS

LIST OF FIGURES

LIST OF TABLES

CHAPTER I

INTRODUCTION AND BACKGROUND*

Disease Pathology

Malaria, a disease which results from a blood-borne parasitic infection with any of several *Plasmodium* species, has remained one of the greatest human global health crises for centuries. The disease has had a significant impact on the development of human civilization; it is undoubtedly one of the oldest and most lethal illnesses in recorded history [1]. There exist many documented cases of malaria in antiquity, with Hippocrates famously noting in approximately 400 BCE that those who drank swamp waters were especially prone to bouts of "quartan" periodic fevers, a characteristic description of the cyclic febrility associated with parasitic life cycles [2]. Archaeological discoveries have even been able to identify the existence of avian malaria in amber-preserved mosquitos originating as early as 15-45 million years ago [3]. As the disease continued to develop in primate and human hosts, many errant etiological theories have been proposed, most notably an attribution to poisoning via miasma, which was thought to be a harmful vapor or mist that occurred near marshes and swamplands. Thus, the term *mal'aria*, meaning "bad air", was eventually introduced into the English medical lexicon in the 19th century. This bad air attribution theory held well into the late 1800's, even after Laveran discovered in 1880 that the disease was the result of mosquito-borne parasites [4, 5].

---

* Portions of this chapter are reprinted from: Gordon, P., Venancio, V. P., Mertens-Talcott, S. U., & Coté, G. (2019). Portable bright-field, fluorescence, and cross-polarized microscope toward point-of-care imaging diagnostics. Journal of Biomedical Optics, 24(9), 096502. with permission from SPIE.

Today, over 3.7 billion people live in regions at-risk for malaria, with 1.1 billion living in high-risk regions and an estimated 16 million currently living in active outbreak foci [6]. Numerous global disease trends are well summarized from the World Health Organization's (WHO) annual World Malaria Report publications (2015 & 2019) [6, 7]. Incidence rates have decreased since the turn of the century; in the year 2000 it was estimated that 262 million cases and 839,000 deaths occurred, but that number fell to 228 million cases and 405,000 deaths by 2018. The African continent accounts for the vast majority of global malaria morbidity and mortality, with 213 million cases (93% of global total) and 380,000 deaths (94% of global total) estimated in 2018. It is estimated that another 7.9 million cases occur annually in South-East Asia, 4.9 million cases in the Eastern Mediterranean, 2.0 million cases in the Western Pacific, and 0.9 million cases in the Americas. Of the four separate individual species of *Plasmodium* known to commonly infect humans (*P. falciparum, P. vivax, P. ovale*, and *P. malariae*), *P. falciparum* is by far the most prevalent, accounting for over 96% of all global cases. *P. vivax*, which is the primary species of infection in the Americas and accounts for approximately half of all infections in South-East Asia, is responsible for 3.3% of global cases. The remaining species, along with rare fifth and sixth zoonotic simian species, *P. knowlesi* and *P. simium*, make up a negligible number of human cases [6-8].

Plasmodium are a genus of blood-borne protozoan parasites whose life cycles necessitate incubation and transmission between an insect vector and a vertebrate host (Fig. 1, adapted from CDC published diagram [9]). In cases of human infection, female *Anopheles* mosquitos ingest parasitic gametocytes during a blood meal, carry the parasites

between hosts as they incubate the sporogonic reproductive cycle, then transmit sporozoites into new human hosts through their saliva during successive blood meals. Once in a vertebrate host, sporozoites will migrate through the vasculature to the liver, where they invade hepatic cells and multiply as dormant hypnozoites. After growing for a time and reaching a critical population, the hypnozoites are released into the bloodstream as merozoites. This mass migration of parasites from the liver into the vasculature begins the asexual-reproduction-stage, or "blood stage", of the disease. During the asexual reproductive cycle, parasites invade, consume, multiply within, and bursting forth from the interior of red blood cells. This cycle is typically well synchronized throughout the infective population, and it is this cyclic reproduction that gives rise to the periodic fevers for which the disease is so well known.

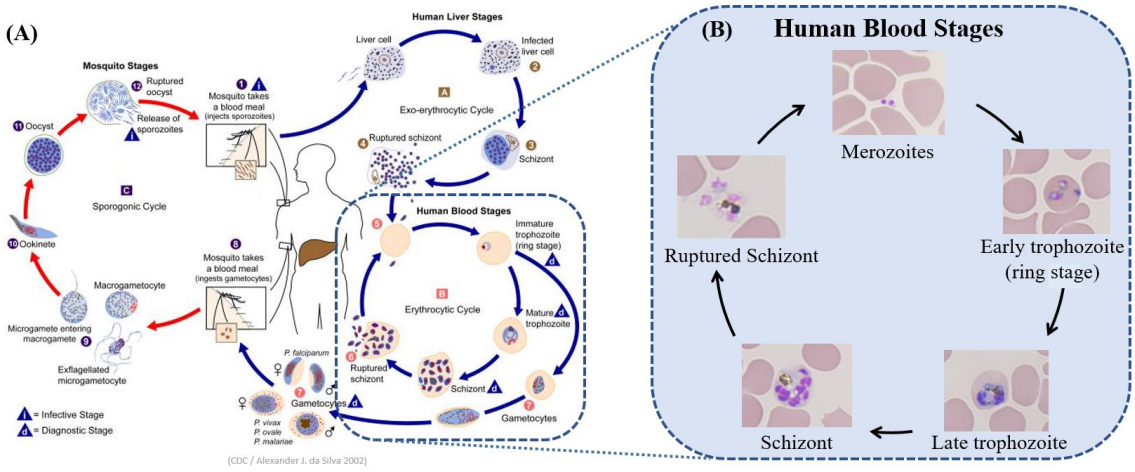

Figure 1: (A) Complete *Plasmodium* life cycle; adapted from CDC public domain image [9]. (B) Stages of *P. falciparum* erythrocytic asexual reproductive cycle.

This reproductive cycle is driven by the metabolism of hemoglobin, which the parasites convert to the crystalline byproduct hemozoin. Depending on the species of *Plasmodium* causing the disease, the erythrocytic reproductive and corresponding fever periodicity can vary between 48, 72, and 96 hours. Eventually, sexualized gametocytes will develop in the blood stream, and these gametocytes those which, when ingested by mosquitos, will further perpetuate the epidemiological process. The fully developed gametocytes are the most distinctive morphologies between the various *Plasmodium species* and are traditionally used to identify the species of infection [9]. Because the blood-stage of parasite growth is typically when symptoms such as fever begin to develop, it is during the progression of this phase that diagnosis is typically performed.

Contextual Awareness

Malaria diagnostics have relied heavily on lab-based microscopy for over one hundred years, and current point-of-care diagnostics fail to provide some quantitative diagnostic information important for complete diagnosis, treatment recommendations, and disease monitoring. Eradication of the disease may be aided by new tools that improve the quality of information provided by in-field diagnostic and monitoring efforts. To this end, this research presents research toward low-cost, portable multimodal microscopy systems designed to collect quantitative diagnostic and monitoring information at the point-of-care. Such systems may enable the diagnosis and monitoring of malaria as well as other conditions that rely on microscopic diagnostic procedures such as tuberculosis, sickle-cell anemia, and others in remote regions around the world.

While a plethora of novel malaria diagnostic systems have been researched and proposed throughout the past century, surprisingly few have had a significant impact on the standard of care around the world, with the notable exception being the recent proliferation of lateral-flow-based rapid diagnostic tests (RDT's). In how many other medical domains has the technology-of-choice remained stagnant for over half-a-century? While it is to be expected that the product development "valley of death" between technology research and commercialization will contribute to significant technological attrition, the failure rate for novel malaria tools is staggeringly high. This could be, in part, because there is a large contextual gap between those developing new solutions in wealthy nations and those who will use them to solve actual problems in remote locations. Keeping this in mind, and with the hope of increasing that this research might actually have some positive impact on patient outcomes, this research has sought to base its technological innovations on a thorough understanding and awareness of the clinical, epidemiological, and translational context and unmet needs of global malaria eradication efforts, which are explored here in some depth.

Diagnostic Practices and Procedures

Correctly diagnosing patients who are suspected of having malaria is critical for both patient outcomes and global disease eradication efforts. Infections begin as "uncomplicated", meaning that patients are in a relatively safe disease state and retain primary bodily functions. If left unchecked, however, infections can rapidly progress to the dangerous "complicated" state, during which the patients can become severely anemic,

febrile, and catatonic. The fear of progressing to this complicated state, along with the widespread presence of antimalarial medications, make it common for any fever-stricken subject in malaria-endemic areas to be presumptively given anti-malarial medications without any actual diagnosis [10]. The literature suggests that, in the absence of high-quality diagnostic tools, the use of symptoms or sub-standard microscopy can lead to over-diagnosis and misdiagnoses [11-13]. This presumptive administration can lead to significant over-medication, wasted resources, ignorance of other maladies, skewing of disease monitoring efforts, and the increased risk for the development of antimalarial drug resistance in *Plasmodium* populations [14-16]. Unfortunately, the overdiagnosis trend is also common for those who report to clinics for treatment; with some studies reporting in-clinic overdiagnostic errors between 36% - 85% [17, 18]. Thankfully, the rate of presumptive diagnosis has significantly decreased over the past ten years, largely due to the increased availability and use of RDT's to screen for and diagnose infections. In 2010, approximately 40% of all suspected malaria cases in Sub-Saharan Africa were tested by any means, with around a third of diagnoses (~33 million) performed via RDT and two-thirds of diagnoses (~17 million) performed via microscopy. By 2018, the percentage of suspected cases who were tested had risen to approximately 85%, with RDT's accounting for around 80% (~170 million) of all tests administered and microscopy accounting for around 20% (~50 million) [6].

According to the 2015 WHO Guidelines for Treatment of Malaria, the main objective in treating severe malaria is to prevent a patient from dying, while secondary objectives include the prevention of disabilities and any recrudescent infections. When

treating uncomplicated malaria, the risk of death is decreased, and the most important goal is to prevent the patient from progressing to a severe disease state. When diagnostic testing is performed, it generally seeks to answer three questions in order to recommend the proper course of treatment [19]. These three "diagnostic pillars" are: (1) whether parasites are present, (2) which species of parasites are responsible for the infection, and (3) what is the parasitemia, or concentration of parasites in the blood. The first pillar – finding evidence of *Plasmodium* parasites – is relatively straightforward and is used to screen patients who truly need antimalarial treatment from those who don't. This screening can be accomplished using microscopy, RDT's, or polymerase chain reaction (PCR) tools, with RDT's being the most commonly used. RDT's are especially suited to this task because they provide a binary determination of the presence or absence of parasites in the bloodstream. Occasionally, RDT use can lead to misdiagnoses when infections are caused by parasites that have mutated to omit the target analyte *pf*HRP2. In general, however, RDT quality and availability are rapidly progressing, making them an excellent choice to screen for infections in a rapid, low-cost, and portable way [15, 20, 21].

The second diagnostic pillar, knowing the species of infection, is important for prescribing appropriate medications that will prevent recrudescence, especially in cases of *P. vivax* or *P. ovale* infections that can leave behind latent hypnozoites in hepatic cells [19]. The necessity for speciation as a part of diagnosis is highly dependent on the geographical region of infection. In Sub-Saharan Africa, infections are nearly homogenously *P. falciparum*, whereas most cases in the Americas are caused by *P. vivax*. Infections found in Southeast Asia, the Eastern Mediterranean, and Oceania are the most

likely to contain mixtures of multiple *Plasmodium* species and thus most necessitate speciation as a part of diagnosis [6]. Traditionally, speciation would be determined only by the observation of gametocyte morphology during microscopic analysis, but advances in the synthesis of species-specific nucleic acids and monoclonal antibodies allow PCR and some new RDT's to differentiate between *Plasmodium* species as well.

The final diagnostic task is to assess parasitemia, or the concentration of parasites in the blood. While the term "parasitemia*"* is medically defined as "the confirmed presence of parasites in a patient", within the context of malaria diagnosis the term is more commonly used to indicate the quantitative measurement of the number of parasites in the bloodstream, usually expressed as the number of parasites per microliter of blood. An alternative expression of quantitative parasitemia is the percentage of red blood cells that contain parasites. Microscopy is again the conventional diagnostic technique used to assess parasitemia; microscopists will perform a counting procedure as they examine blood smears while searching for and identifying parasites during initial diagnosis. Notably, RDT's do not provide quantifiable parasitemia information, making it difficult to obtain the information for patients in remote areas. In some cases, results can be obtained by shipping smears from remote areas to centralized imaging facilities, but oftentimes the time delay and cost associated with transportation can make the process prohibitive. The result is that parasitemia assessment is often unavailable for many patients in the most malaria endemic regions.

Failure to assess parasitemia can negatively impact patient outcomes because it is used by clinicians to assess infection severity, estimate the risk of rapid progression to a

complicated state, and monitor how patients are responding to treatment, especially for *P. falciparum* infections, which are considered to be especially dangerous [22]. Patients who are determined to be at a higher risk of progressing to a severe state may be monitored more closely and placed onto a more aggressive form of treatment such as higher-dosage, more effective, or even intra-venous medications, whereas a more conservative form of treatment may be prescribed for patients deemed to be low-risk due to the low numbers of parasites in their bloodstream [23]. High parasitemia in the absence of incapacitation is an indicator that the disease may be more likely to progress rapidly to a complicated state, especially in the presence of risk factors such as pregnancy, being below the age of 6-10, HIV infection, malnutrition, or anemia [23]. Death from severe malaria often occurs within hours of admission to a hospital or clinic, so it is essential that therapeutic concentrations of a highly effective antimalarial drug be achieved as soon as possible. While the idea of prescribing proper treatment may seem straightforward, there are many decisions that must be made including the combination of therapies and method of administration, a summary of which can be found in Table 1 along with the recommended use cases for each type of malaria treatment.

Table 1: Recommended treatments for various presentations of malaria.

	Treatment *(administration)*	**Use Case**
Uncomplicated	Artemisinin Combination Treatment [ACT]. Five options based on region and availability. *(oral)*	Uncomplicated falciparum (default) Unknown species (default) Uncomplicated Vivax, Ovale, Malariae, Knowlesi (resistant & non-resistant) Mixed infections
	ACT & Primaquine *(oral)*	Uncomplicated falciparum (non-immune) Unknown species (non-immune)
	Chloroquine *(oral)*	Uncomplicated Vivax, Ovale, Malariae, Knowlesi (non-resistant) 1st trimester pregnancies (non-resistant)
	Primaquine *(oral)*	Uncomplicated Vivax, Ovale, Malariae, Knowlesi (non-resistant) 1st trimester pregnancies (non-resistant)
	Quinine & Clindamycin *(oral)*	1st trimester pregnancies for chloroquine resistant vivax
	Sulfadoxine-Pyrimethamine [SP] *(oral)*	Preventative for 2nd-3rd trimester pregnancies in Sub-Saharan Africa Preventative for African children
Complicated	Artensunate *(parenteral)*	1st choice for complicated or high-risk infections
	Artemether *(parenteral)*	2nd choice for complicated or high-risk infections
	Quinine *(parenteral)*	Co-3rd choice for complicated or high-risk infections
	Chloroquine *(parenteral)*	Co-3rd choice for complicated or high-risk infections

Malaria Eradication Goals

Global guidance for malaria eradication strategies are primarily coordinated by the World Health Organization (WHO), which evaluates public health, research, and political trends to make recommendations and lobby for effective policy. In 2015, the WHO

published a 15-year strategic plan for malaria eradication with detailed goals and milestones between the years 2016 – 2030 [24]. This plan targets at least a 90% decrease in the global mortality rates by the year 2030 when compared to 2015 numbers. While ambitious, this 15-year target demonstrates a worldwide dedication to the effort, giving legitimate hope that it may be possible to entirely eradicate the disease during this century. Whenever such full eradication does happen, it will assuredly be celebrated as one of the most significant public health achievements in human history. At the time of the 2015 publication, overall malaria incidence rates were on a consistent downward trajectory since the beginning of the 21st century, but that continued progress has begun to stall in the years since, such that global incidence has actually reversed its downward trend and begun increasing in many of the countries with highest endemicity. This trend reversal is the result of several emerging challenges to eradication efforts that must be overcome with new practices and technologies if eradication efforts are to continue their success.

At a high level, malaria eradication strategies rely on combined efforts to provide high quality vector control, diagnostics, antimalaria medications, and preventive therapies. The heterogeneity of social, biological, and economic factors in malaria endemic regions dictates that local strategies must be tailored to meet the specific needs of the community. This need for specificity, along with the necessity of high-fidelity information to inform policy, underscores the importance of maintaining accurate surveillance and monitoring systems. The WHO has identified the expansion of quality-assured diagnostic testing as a key component of their strategic response program, which seeks to confront numerous emerging challenges to malaria eradication including persistent demographic trends,

urbanization, *pf*HRP2 deletion, climate change, and emerging drug resistance. Improvements must also be made in disease monitoring programs in order to better inform policy and research directions to combat these emerging challenges. In-depth summaries of projected challenges to malaria eradication can be found in the Malaria Eradication Guide (2020) and the Global Technical Strategy guide (2015) published by the WHO [24, 25]. As noted previously, the current lack of parasitemia data from remote diagnoses is a potential need that could be filled to fulfill the goal of expanded quality-assured diagnostic and monitoring systems.

Antimalarial Drug Resistance

The proliferation of novel resistances to antimalarial medications is perhaps the direst threat to eradication efforts. The fact that *Plasmodium* are evolving to be resistant to the therapeutics used as the current standard of care is especially concerning when recent history is considered. When it was first introduced in 1934, chloroquine quickly became known as an effective therapeutic and prophylactic medication for malaria, a reputation it held unquestioningly for over three decades as it became the medication of choice to treat and prevent the disease by clinicians around the globe [26]. By the early 1960's, however, the development of resistances to the medication in *P. falciparum* was being recognized by the World Health Organization, and as the 1900's drew to a close chloroquine resistance was believed to have migrated from its origins in South and Southeast Asia to nearly every region of the world with endemic malaria [27]. Reduced efficacy of the most prominent malaria treatment had the potential to be devastating to

global disease morbidity and mortality, fortunately new therapeutics based on artemisinin derivates concurrently emerged as a highly effective treatment option. Now the most widely recommended treatment for malaria, artemisinin combination therapies (ACT's) co-administer long-acting antiparasitic agents along with fast-acting artemisinin derivatives to provide excellent treatment that have been shown to decrease the probability of novel drug resistance development [28]. Even so, numerous isolated loci of ACT resistant *P. falciparum* have begun to emerge in Southeast Asia, beginning what could become a spread of drug resistance that parallels to the spread of chloroquine resistance sixty years ago. It is not difficult to imagine the potentially devastating consequences such an occurrence would have on global malaria eradication efforts [14, 29]. To combat the spread of these newest waves of anti-malarial drug resistance, the regional efficacy of ACT's must be monitored so that new populations of resistant parasites can be isolated and given especial attention to prevent their proliferation.

PCR and genetic sequencing are the best tools currently available for definitive confirmation of specific mutations leading to ACT drug resistance. While this level of confirmation is irreplaceable in monitoring efforts, it is theoretically possible to identify resistant infections by measuring the parasitic clearance rates during treatment. This monitoring methodology has the potential to act as a cost-effective screening tool that could be widely implemented in at-risk areas with lower barrier to entry than either PCR or genetic sequencing. Nominal clearance rates for ACT in Southeast Asia have been reported to be approximately 10^{-2}/24 hours, or a 100-fold reduction in the number of bloodborne parasites over 24 hours after initial treatment [30]. Resistant strains of

parasites, however, express reduced clearance rates that can range from nominal clearance down to 10^{-2}/48 hours, indicating a doubling of time needed to reduce the concentration of parasites in the bloodstream by a given amount [31]. The data needed to measure clearance rates are provided by the third diagnostic pillar, the quantitative measurement of parasitemia. These data are provided by microscopic analysis of patient blood samples, meaning that if a point-of-care microscopy device that quantitatively measures parasitemia could discern the difference between these two clearance rates during periodic monitoring of patients, it would be theoretically possible for it to detect a drug resistant strain and be a viable candidate for providing the scientific community with an additional tool to detect and prevent the spread of ACT resistance *Plasmodium* species.

Malaria Microscopy and Point-of-Care Technologies

Few tools are as ubiquitously useful for medical diagnoses as the benchtop microscope, making the lack of microscopy services in many remote areas a significant restriction to the quality of care [32, 33]. For over one hundred years, the gold-standard test to diagnose malaria has been to use high-magnification benchtop brightfield microscopy to examine thick and thin Giemsa-stained peripheral blood smears to identify and quantify the presence of *Plasmodium* parasites [34, 35]. To perform this test, two drops of patient blood must be placed on a clean microscope slide, with one being used to create a thick smear and the other spread to create a monolayer of cells for the thin smear. After air-drying, these smears are fixed and stained using methanol and a Romanowsky-based stain that accentuates parasites in the blood with characteristic pink, purple, and

blue hues (Fig. 2). The smears are examined using 1000x magnification using a benchtop microscope with 100x oil-immersion objective by a trained microscopist to determine the presence, concentration, and species of *Plasmodium* in the bloodstream [34].

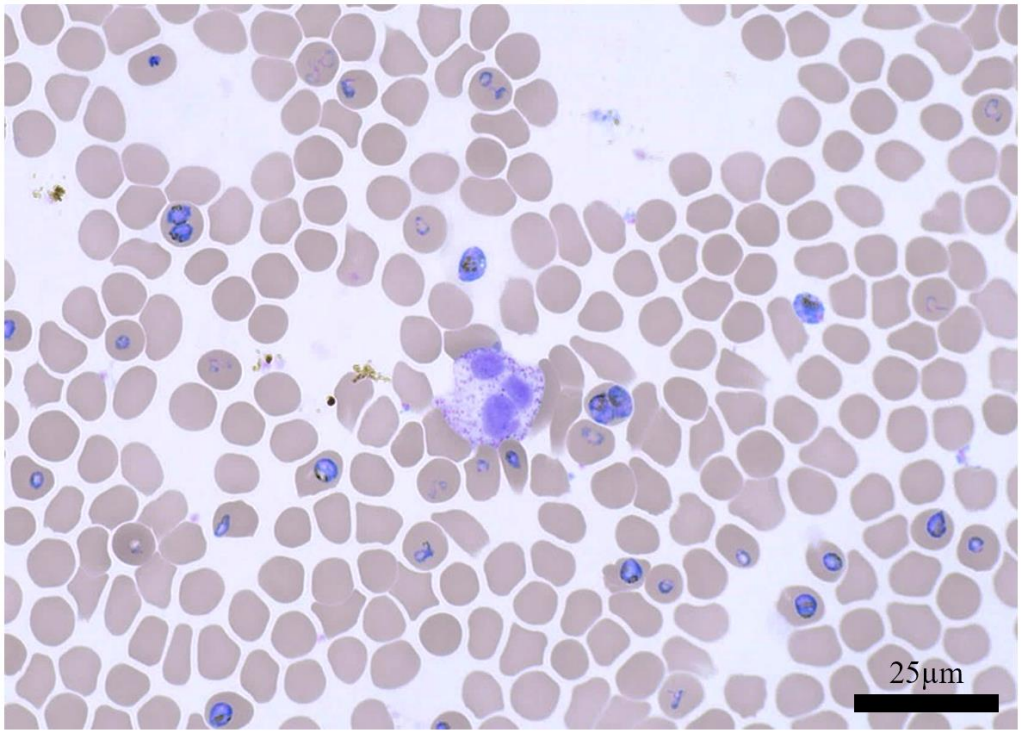

Figure 2: Gold-standard brightfield micrographic image of a thin blood smear with Giemsa-stained red blood cells, *P. falciparum* parasites, and white blood cell.

Taking microscopy out of a central lab to improve patients' access to care is not a new proposition. Seminal works by McArthur in the 1930-1950's describe and demonstrate the benefits of point-of-care brightfield microscopy [36-38]. Since then, numerous iterations of portable microscopes have been proposed and commercialized [39-41]. A recent, popular approach leverages advances in smartphone technology – their

network access, processing power, onboard cameras, and other built in sensors – to construct either intrinsic or extrinsic diagnostic devices [42]. Intrinsic devices can be defined as those that use pre-existing integrated optics, while extrinsic devices are those that use dedicated, standalone optics. While intrinsic microscopy systems that are built around cellphones can reduce costs and device complexity, the wide variety of smartphone models and ever-changing camera optics make quality assurance and the control of imaging performance difficult. Additionally, most proposed intrinsic and smartphone-based microscopes are restricted in their resolution limit due to the low possible numerical aperture (NA) and high aberration coefficients of the lenses used in their simplified, condensed imaging systems [43]. Extrinsic devices, such as the one presented in this work, detect pathologic biomarkers using dedicated external hardware and can be capable of transmitting data to personal electronic devices for review and processing [42]. Extrinsic configurations offer the advantages of using customizable optics with dedicated hardware that will vary less with time or region compared with cellphone-based systems, and they allow for more advanced automated processing options due to the range of possible interconnected personal electronic devices.

Any portable microscopy system used for diagnosis will be measured against both benchtop microscopy and the predominant option for point-of-care malaria diagnosis, RDT's. Rapid diagnostic tests are lateral flow based systems, similar in principle to the more well-known home pregnancy test strips. In malaria RDT's, a drop of blood is placed on the inlet pad of a paper strip, and the application of a buffer compound initiates wicking along the length of the strip to an area where the sample interacts with bio-recognition

elements that selectively bind to malaria-indicative biomarkers in the blood (Fig. 3, adapted from WHO/CDC report [11]). The most commonly detected biomarkers are *Plasmodium falciparum* histidine-rich protein II (*pf*HRP2), *Plasmodium* lactate dehydrogenase (*p*LDH), which can be either pan-specific or species specific, and pan-specific aldolase [44]. The biomarker *pf*HRP2 is specifically a biomarker of *p. falciparum* and has been shown to be more sensitive than *p*LDH, which can be species-specific for multiple species and has a better specificity [45]. If *Plasmodium* are present, their biomarkers are conjugated with recognition elements and will be caught in a detection pad further along the strip, initiating a visible color change that is readable by the naked eye. Numerous variations of RDT's have been commercialized, with most primarily for the detection of only *P. falciparum* and a minority also able to differentiate between *P. falciparum* and *P. vivax*. Typically, RDT's are sensitive enough to detect infections at or above 200 parasites/μL of blood, as can be found in the WHO quality assurance verification testing report for commercially available RDT's [46].

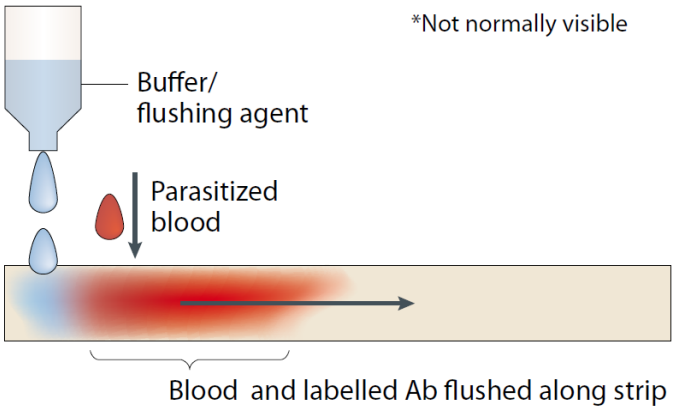

Figure 3: Principle of RDT use. Photo public domain under terms of US Code Title 17, Chapter 1, Section 105. Reprinted from [11].

Values for the sensitivity and specificity of both microscopy and RDT's can vary in the literature, especially for microscopy services, underscoring the technique's dependence on infrastructure and technician skill. Consequently, there is a need for automated, controllable alternatives that improve both access and reliability. According to a 2016 study by Mahende et al. that compared both lab-based microscopy and RDT's to ground-truth PCR in Tanzania, the sensitivity and specificity of microscopy for malaria diagnosis were 91.1% and 100.00%, respectively, while sensitivity and specificity of *pf*HRP2-based RDT's were 88.6% and 97.8%, respectively [47]. It was found that there were greater disparities between measurements taken using the two methods in regions of low transmission rates. A similar study, conducted by Batwala et al., found that results of microscopy did not vary greatly whether it was conducted by "experts" or in regional health centers, with expert sensitivity and specificity measured at 46.1% and 97.2%, respectively, and health center sensitivity and specificity measured at 47.2% and 93.4%,

respectively [48]. Meanwhile, RDT's again displayed more consistent results with sensitivity of 91.0% and specificity of 86.3%. Clearly, so long as adequate quality assurance measures are taken, automated processes such as RDT's can perform more reliably when compared to those that significantly rely on human skill such as benchtop microscopy.

The costs associated with diagnostic and monitoring technologies can significantly affect their accessibility and successful use in remote areas, especially given frequent co-occurrence between malaria endemicity and economic impoverishment that results in reduced funding available for medical care. A useful metric when balancing both cost and efficacy is the incremental cost-effectiveness ratio (ICER), which is defined as the difference in cost between two possible interventions divided by the difference in their efficacy. The result is an adjusted value that is more useful when considering investment in widespread use, as technologies that are more expensive but provide better outcomes can ultimately provide better value. For reference, ICER values for both RDT's and microscopy are provided in Table 2 (data reprinted from [18]), with values and high-transmission and low-transmission regions differentiated because of potentially significant efficacy differences in each of those areas.

Table 2: Diagnostic incremental cost-effectiveness ratio in Uganda.
Data reprinted from [18].

Diagnostic Technique	Cost (ICER, USD)
Gold-Standard Microscopy (overall)	$9.61 / correct treated case
Rapid Diagnostic Test (overall)	$5.0 / correct treated case
Gold-Standard Microscopy (low transmission)	$7.63 / correct treated case
Rapid Diagnostic Test (low transmission)	$5.85 / correct treated case
Gold-Standard Microscopy (high transmission)	$12.98 / correct treated case
Rapid Diagnostic Test (high transmission)	$4.38 / correct treated case

Multimodal Microscopy Approach

In designing a portable microscopy system, multiple imaging modalities may be considered. Brightfield microscopy is the definitive standard for historical malaria diagnosis, but it is by no means the only microscopic mode that has been proposed or demonstrated for the task. Conventional brightfield microscopes pass broadband (white) light through a sample and gather information based on the light that is attenuated by the sample due to scattering and absorption. In stained thin blood films, contrast is generated primarily by refractive index changes at cell membranes and absorption due to the binding of chromophores to various morphological features of the parasites, especially the "malarial pigment", hemozoin [49-51]. High magnification is needed to directly observe parasitic micro-morphology that is used to identify and characterize the disease. The skill needed to prepare, examine, and interpret these morphological features make it difficult

to implement at the point-of-care, with the result that patients in the most at-risk, low-income regions can lack access to high standards of diagnosis and care [52-54].

Fluorescence microscopy has also garnered much interest in recent decades for its potential to selectively stain parasitic DNA within red blood cells with high contrast [55-59]. In principle, fluorescence microscopy generates signal by illuminating a sample with a short wavelength of light, then selectively allowing only photons that are re-emitted from the sample at a longer wavelength to be imaged. By introducing target-selective agents to the sample that cause this Stokes-shift to occur, the contrast of desired features can be enhanced greatly. Numerous studies have iterated and evaluated the potential for fluorescence imaging to improve the quality of microscopic malaria diagnosis, with most indicating that the use of fluorescent stain enhances the speed of diagnosis with minimal loss of sensitivity for even low-parasitemia smears [41, 55-68].

More recently, various specialized microscopy methods have also been proposed to detect the contrast of the malarial metabolic byproduct, hemozoin [50, 69]. Hemozoin, also known as “malaria pigment”, is a crystalline structure formed in the parasite food vacuole from lingering heme molecules after hemoglobin digestion. The crystalline structure of hemozoin gives rise to unique physical properties that can be detected using a number of methods including paramagnetic concentration, photoacoustic and harmonic resonance, signature scattering behaviors, characteristic absorption spectrum, electrophoretic flow rate, and selective depolarization of light [49, 53, 70-79]. Hemozoin can be easily seen using a conventional brightfield microscopy by placing crossed polarizers on each side of the sample plane, causing the all photons to be attenuated that

have not had their e-field plane rotated by the birefringent hemozoin crystals [80, 81]. By nature, hemozoin accumulates primarily during late-stage infections after significant hemoglobin has been metabolized from the bloodstream, making it unreliable for early stage disease microscopy diagnosis [82-86]. Despite its current limitations, hemozoin remains an intriguing subject of research due to its unique properties, species specific structure, adaptability to various detection strategies, and role in antimalarial drug development [70, 87].

CHAPTER II

SAMPLE PREPARATION AND STAINING*

Introduction

Peripheral blood smears are essential to the characterization, diagnosis, and monitoring of various diseases such as malaria, anemias, sickle cell diseases, thrombocytopenia, thrombocytosis, leukemia, lymphoma, and iron deficiency [88-91]. These smears can be used to diagnose, characterize, and monitor diseases either manually or using automated microscopic techniques to observe cell morphology and differential blood cell counts [88, 90-92]. The general use of peripheral blood smears involves three primary steps: 1) formation; 2) fixation/staining; and 3) examination. Smear formation is the process of physically manipulating a blood sample to form a thin layer of cells with proper thickness, shape, and density, and this procedure is the recommended practice for sample preparation for the microscopic diagnosis of malaria. Fixation and staining use various chemicals to accomplish some combination of sample inactivation, permeabilization, adhesion to a substrate, and augmentation with a contrast-enhancing stain prior to examination. This research investigates various sample preparation and

* Portions of this chapter are reprinted from: Branan, K., Gordon, P., Dogbevi, K. S., & Coté, G. L. (2020, February). Thin-film plastics used in microfluidic channels for microscopy imaging in low resource settings. In Optics and Biophotonics in Low-Resource Settings VI (Vol. 11230, p. 112300M). International Society for Optics and Photonics. with permission from SPIE.

staining protocols used to enhance the contrast of both gold-standard and novel, microfluidic-based automatically generated smears, with the goal of maximizing utility for malaria diagnosis and monitoring in remote locations and at the point-of-care.

Dry Smear Creation and Staining

To prepare a conventional thin smear, a small drop of patient blood is deposited onto a microscope slide, where it is immediately "wiped" across the surface of the glass to form a monolayer of cells using a second slide [22]. After the film has been formed and dried, it will be fixed using either physical or chemical techniques [93]. Fixative chemicals include formaldehyde, glutaraldehyde, acetone, ethanol, methanol, or combinations; while physical methods include heating, microwaving, and cryo-preservation (freeze-drying) [93-96]. Most typically, the smear will be submerged in 100% methanol for 30-60 seconds immediately prior to staining to effectively permeabilize, preserve, and prepare the sample for stain uptake [97]. Some stains, such as Leishman Stain, include fixative agents in their composition and allow for a single-step fixation/staining procedure [98]. Exact fixation protocols can vary to account for differences in stain concentration, temperature, osmolarity, and materials used [99]. A proper fixation technique will result in smears that preserve cellular morphology and allow for stain uptake by the sample to produce the desired contrast [95, 99].

While various types of stains may be used to enhance features of peripheral blood smears, this work focuses primarily on the adaptation of Romanowsky-type brightfield stain and Acridine Orange (AO) fluorescence stain for use at the POC. Variations in

traditional staining protocols arise from variables such as staining compounds, time, concentration, buffers used, pH balance, and age, all of which must be controlled to produce smears with the desired contrast enhancements [88, 100]. Romanowsky and Giemsa-Romanowsky stains are fundamentally a combination of eosin and methylene blue derivatives which create a wide range of blue, purple, and pink hues. Some common examples of these stains include Giemsa, Field's, JSB, Wright's, and Leishman stains, which can be used in numerous distinct ways depending on the sample type and desired effect [96, 98]. It is important to note that the presence of multiple staining compounds is required to create the compound purple hues in what is known as the "Romanowsky effect" within the granules of neutrophils, chromatin, and other cellular matter. Azure B, a methylene blue derivative, is a small molecule and can stain quickly, while eosin, the pigment mainly responsible for the red color, is three-times bigger and takes longer to diffuse across the cell's membrane, creating a time-hue interdependency that must be considered [96]. When used in peripheral blood smears, the Romanowsky effect is especially visible wherever DNA is present, which causes *Plasmodium* parasites to appear with high contrast due to the lack of DNA in erythrocytes.

Similarly, the use of fluorophores in peripheral blood smears has been shown to be viable for parasitic contrast enhancement within red blood cells (RBCs), with some studies claiming greater sensitivity with the use of fluorescent stains when compared to brightfield-chromophores [55-57, 62, 67]. Acridine Orange is a cell-permeant stain that bonds to DNA and RNA via intercalation with emission peaks of 526nm and 650nm, respectively. It has been used previously in malaria research and diagnosis due to its

combination of function, cost, and stability. SYBR Green-1 is another fluorophore with similar excitation and emission spectra to AO that expresses significant fluorescent enhancement when bound to DNA, giving it a greater signal-to-background ratio than many other fluorophores that emit strongly when unbound.

Use of both brightfield and fluorescent stains require that a balance is achieved between maximization of stain-target binding and saturation of the sample such that binding specificity and contrast are lost [88]. In Romanowsky stained blood smears, under-staining results in highly transparent samples with poor contrast, and over-staining results in nearly homogenous light absorption throughout entire cells such that little to no chromatic variance between targets and the cellular background can be seen. Fluorescently labelled smears, when under-stained, do not emit sufficient photons to generate a discernable signal, and over-staining results in excessive fluorescence being seen in sample background, cellular membranes, and condensed debris, creating washed-out images. The complexities of staining protocols and diversity of applications thus require that customized protocols be adapted for each unique circumstance.

Poor smear preparation, fixation, and staining should be avoided whenever possible to mitigate diagnostic errors which can lead to improper drug prescription, increased morbidity & mortality, and undue socio-economic burden [89, 100-104]. Since diagnostic errors oftentimes are attributed to smear quality, several automated smearing devices have been developed (e.g. automated slidemakers and paper fluidic devices), but most are typically unsuitable for use at the point-of-care because they tend to be cumbersome and expensive [105]. One automated slidemaker device designed by Horning

et.al is different in that it is less expensive and reasonably well suited for fluorescence imaging, however, it lacks optical transparency for bright field imaging [100]. Thus, there is a need for an automated or semi-automated smear generation and staining platform technology and simple protocols that can incorporate a diverse set of sample stains for use at the POC [88, 100]. Dogbevi et al. have recently demonstrated the use of microfluidic channels capable of creating homogenously distributed thin blood smears, and the channels' potential utility within a portable microscopy system will here be investigated along with necessary alterations to their construction and staining protocols for use at the POC.

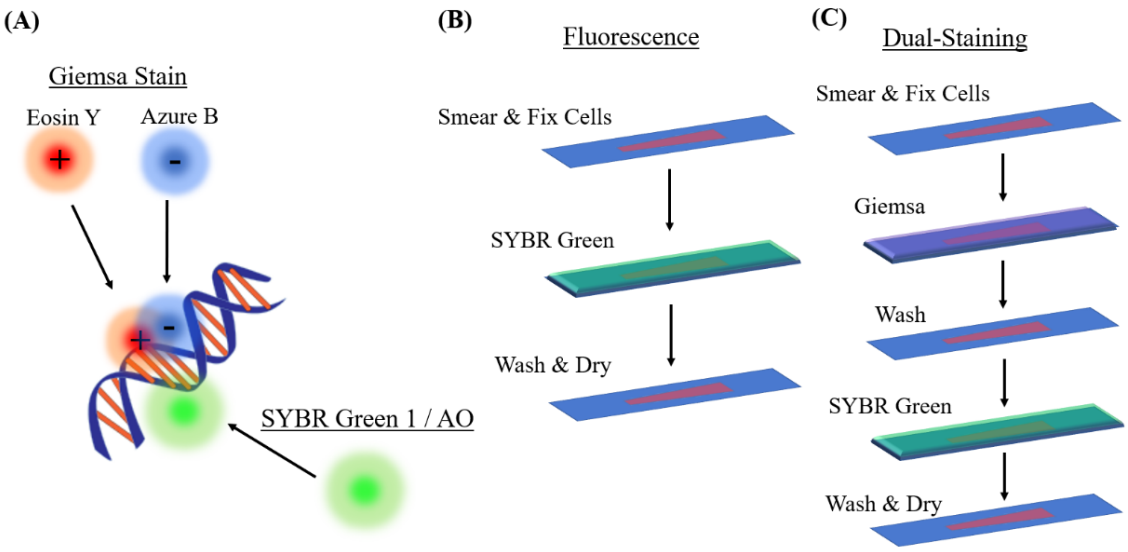

Figure 4: (A) Diagrammatic representation of Giemsa and fluorescent stain binding via DNA intercalation. (B) Steps required to stain a dry smear with fluorescent stain. (C) Steps required to dual stain a dry smear with both Giemsa and fluorescent stains.

Conventional Giemsa staining protocols for malaria microscopy can be applied to previously created smears so long as they have been fixed in 100% methanol and stored in a dry, clean environment. To stain, slides are submerged in freshly prepared 1x Giemsa stain for 45 minutes, and they are afterwards dipped in Giemsa buffer several times to remove excess chromophores prior to air drying. An excellent set of full smear creation and staining procedures used in these works are provided by the United States Center for Disease Control [106, 107]. SYBR Green-1 was found to be the preferable fluorophore for the staining of dry thin smears compared to Acridine Orange due to its higher signal to background ratio. To stain a previously created thin smear, the smear is flooded with approximately 500 microliters of 1:8,000 dilution of SYBR Green-1 in 1x Tris-HCL buffer pH 8 and allowed to incubate for five minutes in the dark. Afterward, smears should be rinsed for approximately 10 seconds with DI water and air dried in the dark (Fig. 4b). When using Acridine Orange stain, the same procedure is repeated using a solution of AO 12 µg/mL in 1x PBS pH 7.4, and the smears should be subjected to an additional submersion in DI water for several minutes to more fully rinse unbound fluorophores from the smear prior to final air drying. An additional dual-staining methodology published in the literature by Guy et al. was implemented because of its theoretical ability to enhance both brightfield and fluorescence contrast [57]. This technique involved the primary staining of the sample using a modified Giemsa staining method, followed by subsequent washing and SYBR Green staining procedures (Fig 4c). Although numerous iterations of the technique were attempted, it was found to not provide sufficient contrast to enhance detection of parasites in either brightfield or fluorescence imaging, likely due to the

competition of chromophores and fluorophores for DNA intercalation binding sites (Fig. 4a). Results of these experiments are given in Chapter 4.

Modification of Microfluidic Channels Used to Prepare Thin Smears

The process of manual smear creation requires significant practice and skill, and there is variability in the quality of smears created both with a single technician on different days and between different technicians [108]. The inconsistencies associated with this process underscore the need for a system of improved reliability when creating blood smears. In low resource areas, microfluidic channels have become new platform for diagnostic devices due to their robustness and cost effectiveness and have been used in conjunction with brightfield, phase contrast, and fluorescence microscopy to image cells and organelles [109-112]. Hypothetically, by combining a smear-generating microfluidic cartridge with a portable microscope, a low resource imaging platform can be created for disease diagnostics.

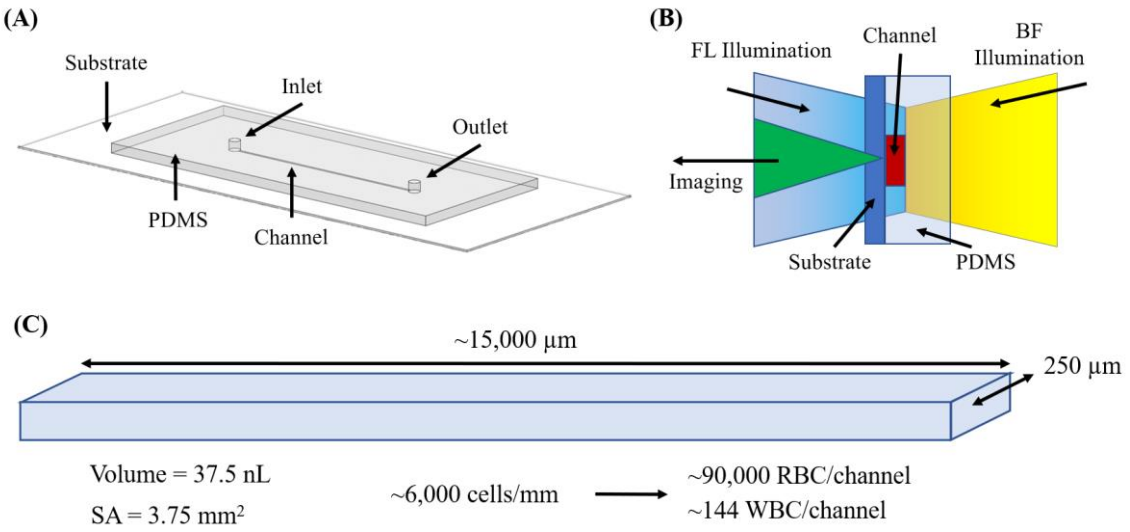

Figure 5: (A) Microfluidic chip overall construction. (B) Cross-sectional view of cartridge showing light paths during use in a multimodal microscopy system. (C) Microfluidic channel internal dimensions along with volume and expected number of cells when filled with human blood.

When creating a microfluidic cartridge, one manufacturing method is the use of soft lithography to stamp a microchannel into PDMS [109, 113]. The PDMS channel is then bonded to a microscope slide using oxygen plasma treatment. After plasma bonding, the cartridges are thermally cured at 110°C for one hour to finalize channel-substrate bonding, creating a complete microfluidic cartridge (Fig. 5a). Glass is traditionally used as the substrate for polydimethylsiloxane (PDMS) channels because of its optical favorability, however its cost and mechanical properties make it less than ideal for use with a portable microscopy platform. Significant optical aberrations can be created when imaging through the typical thicknesses of microscope slides (1 mm) unless expensive optics are used to compensate, while thinner glass slides such as coverslips (~174 µm) become too fragile for reliable use. Therefore, a thin optically transparent plastic becomes

a favorable low-cost substitute binding substrate. Clear plastics typically have a refractive index slightly higher than that of conventional crown or soda-lime glass (Table 3), but the differences should provide minimal differential potential for inducing aberrations if the material thickness can be minimized. As an example of the costs associated with plastics and glass substrates, one sheet (610 mm X 1219 mm) of Clear Makrolon Tuffak Lexan Polycarbonate (ePlastic) at a thickness of 0.254mm costs ~$6.10 which can be cut into about 619 cover glass sized (50mm X 24mm) pieces. Cover glass comes in sets of 66 for ~$36 (Fisherbrand Cover Glasses: Rectangle) making each slide ~$0.55 while each plastic slide would be ~$0.01. It is easy to see that plastic substrates can be more cost-efficient and durable when compared with their glass alternatives.

Table 3: Candidate microfluidic substrate materials and refractive indices.

Substrate Materials	**Refractive Index at λ= 0.5 μm**
Soda-lime glass	1.518
Quartz glass	1.4623
NBK7 borosilicate crown glass	1.5214
Polycarbonate	1.5970
PET	1.657
PDMS	1.4359

A series of plastics such as polycarbonate (PC), polyester (PET), and polyvinylchloride (PVC) were chosen as potential substitute substrate materials based on a combination of their material and optical characteristics. Studied material characteristics include coefficients of thermal expansion, refractive index, optical clarity, and the bond strength resulting from plasma bonding with PDMS. Table 4 displays a combination of the optical and material characteristics that were used to determine appropriate options for a plastic substrate. Because the microfluidic manufacturing process used both plasma bonding and a baking cycle at 110°C, sample cartridges were constructed with each substrate material and subjected to normal fabrication protocols to assess their compatibility with the process.

Table 4: Material and optical characteristics of different transparent plastics.

Type of Plastic	**Optical Specifications**			**Material Specifications**	
	Transmission %	Refractive Index	Haze %	T_g (°C)	Contact Angle (°)
Polycarbonate (PC)	89 – 91	1.584 – 1.586	0.2 – 2.7	150.0 – 200.0	82
Polyester (PET)	87 – 92.1	1.575	0.20 – 5.1	73.0 – 78.0	72.5
Polyvinyl Chloride (PVC)	< 97	1.381	2.5	60.0 – 100.0	85.6

The strength of the bond each plastic formed when bonded to the PDMS channel was subjectively tested by attempting to manually delaminate the two materials after plasma bonding. It was evident using this subjective test that polyester has the strongest bond strength of all materials, but that polycarbonate also bonded sufficiently well to be a

potential candidate. When post-baking the test cartridges to finalize substrate bonding, it quickly became evident that material stability throughout the 110°C baking process was critical, as some chips began to warp considerably. This result is not surprising; any significant difference in thermal expansion or contraction between the substrate and PDMS would cause the entire cartridge to warp as the surface areas of each change. To assess the best candidates in terms of thermal stability, samples of each available thickness of plastic sheet material were baked at 110°C, and the changes in surface area and material thickness were measured. Results indicate that polycarbonate was the most stable at the time and temperatures used, as its change in overall surface area was less than 0.5% for all thicknesses, while PET shrank by over 1%, and PVC by more than 2.5% (Fig. 6). These results were confirmed by observing that cartridges bonded to polycarbonate substrates warped less in the oven than those bonded to the other candidate materials.

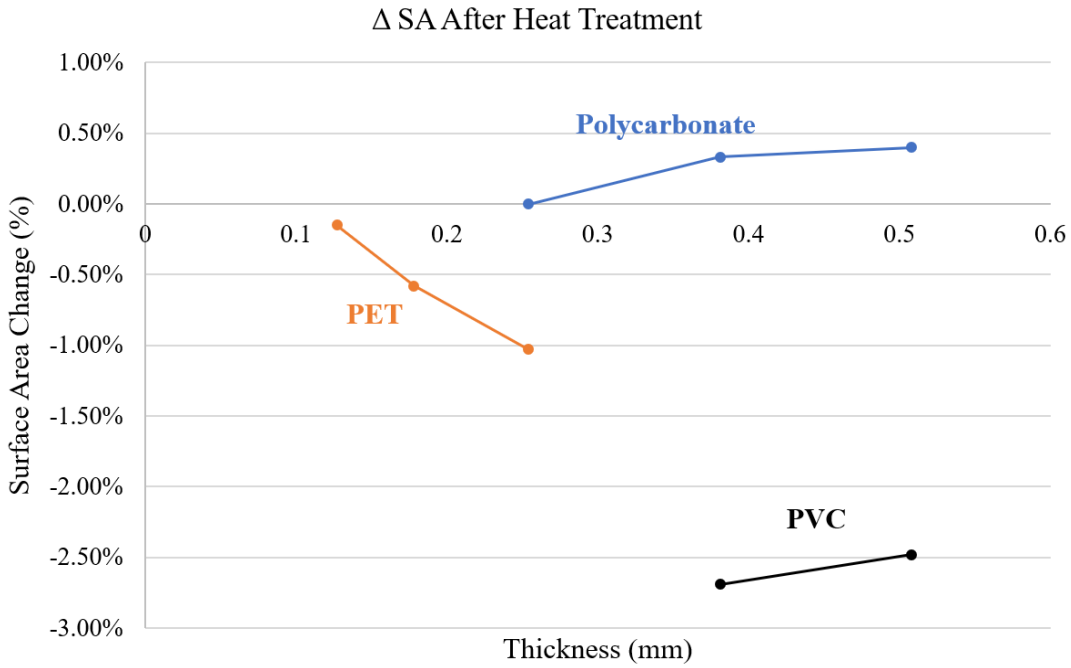

Figure 6: Changes in surface area for various thicknesses of candidate plastic substrate materials after heat treatment.

In-tube Fluorescence Staining

As a closed system, it is difficult for smears in microchannels to dry between liquid reagent steps as in most standard staining protocols. Thus, such protocols are not feasible for use with smears generated in microchannels. In this work, the development of wet fluorescence staining protocols that facilitate the diagnosis of hematological diseases such as malaria using multimodal brightfield microscopy through microfluidic cartridges at the POC are described. These staining procedures allow for sample analysis in under 20 minutes, with results comparable to those achieved using traditional dried smear staining protocols.

Materials and Methods

Cultures of *P. falciparum* were grown asynchronously *in vitro* to a parasitemia of approximately 5% in human RBC's. Samples of the cultured cells suspended in growth media were centrifuged for 2 minutes at 2,000 rcf to form a loose pellet of parasitized RBC's in the base of the tube. The supernatant media was removed, and the process repeated twice more to form a loosely packed, un-lysed pellet of parasitized RBC's. This pellet was resuspended 1:1 by volume in fresh human blood plasma, and the resulting resuspended culture was mixed 1:1 with whole human blood to create a physiologically representative sample of human blood doped with *P. falciparum*. Control smears from each stage of sample reconstitution were created and examined to ensure that cellular morphology and hematocrit were preserved.

Acridine orange (AO) was chosen as the fluorophore for use with an in-tube staining procedure because of its thermal stability and precedence of use for malaria diagnosis [61]. AO stock solution was made as a 96 µg/mL suspension in PBS pH 7.4. Further dilutions of fluorescent stains at 6 µg/mL and 12 µg/mL were created by further diluting the stock solution to the desired concentrations in 1x PBS. Gold-standard reference smears for fluorescence stains were created on glass microscope slides according to published procedures [22, 56, 57, 61, 62]. While the gold-standard staining methods use previously dried and fixed thin smears, staining for use in a microchannel-generated thin smear requires staining to be done in liquid-phase suspension.

To create stained blood samples, stain solutions were mixed with reconstituted parasitized blood in 1:2 (stain:blood) ratios by volume in 2mL centrifuge tubes. The

combined sample and stain were mixed by hand for 30 seconds then set aside under a light-shielding covering for 10 minutes to incubate at room temp. After 10 minutes, 0.5µL of sample was deposited at the inlet of the micro channels and allowed to flow from the inlet to the outlet of the channel, creating a thin monolayer of cells. After the stained blood stopped flowing inside the channel (flow times were 4.31 ± 0:39 min.), a Nikon Eclipse Ti-2 microscope with 60x oil-immersion objective was used to take images of the cells from the outlet to the inlet at 0.5 mm increments, and the images were catalogued for later analysis.

Results

Image analysis was performed to compare staining quality, which was defined as the quantitative feature separability of parasites from both intracellular and extracellular backgrounds. Fluorescence images were monochromatic, with parasites, red blood cell, and background features segmented using intensity thresholds that were commonly applied to all images taken for each staining procedure. Processing was performed using Nikon BR Elements software to assess the feature separability and repeatability. The quantitative variance of stained features was used to assess overall repeatability both within and between images gathered from each individual smear. Throughout all portions of image analysis, cellular morphology was qualitatively assessed to ensure that no crenation, lysis, or significant morphological deformations occurred at any point during the staining process.

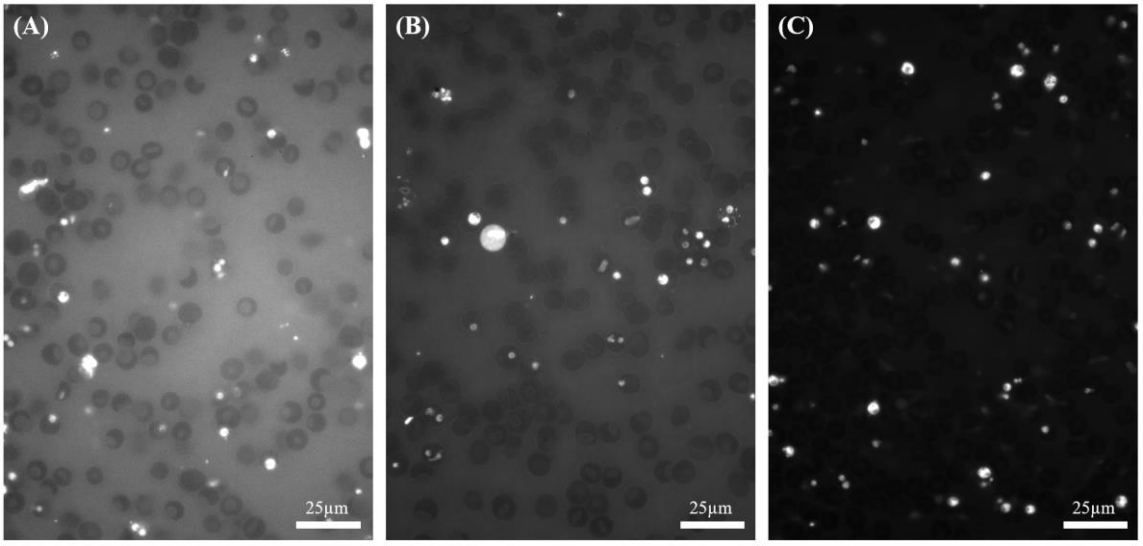

Figure 7: Monochromatic images of in-channel samples fluorescently stained using (A) 6µg/mL, (B) 12µg/mL, and (C) 96µg/mL Acridine Orange. Greater contrast between parasites and background can be seen with higher stain concentration. Images shown with linear contrast enhancement for visibility.

Channels stained using 6 µg/mL, 12 µg/mL, and 96 µg/mL Acridine Orange were collected, along with a gold-standard control on microscope slides to assess staining quality for several concentrations of stain. One sample of each concentration was imaged for the 6 µg/mL, 96 µg/mL, and gold standard stains, with the 6 µg/mL sample containing 10 FOV and 839 parasites, the 96 µg/mL sample containing 7 FOV and 1042 parasites, and the gold-standard containing 7 FOV and 415 parasites. Three separate samples at the concentration of 12 µg/mL were created, with 10, 10, and 9 FOV containing 1671, 1044, and 1141 parasites, respectively. Images from each concentration of fluorophore showed that the uptake of AO by parasites was sufficient to allow them to be clearly seen above the RBC and background signals (Fig. 7). Results show a correlation between increased stain concentration and increased fluorescent signal intensity, with the parasitic signal

from the highest concentration of stain averaging around 17,000 counts in a 16-bit image, comparable to the parasitic signal intensity in gold-standard images (Fig. 8). Parasitic features stained with 6 µg/mL and 12 µg/mL AO in microchannel smears displayed smaller intensities near 4,000 counts.

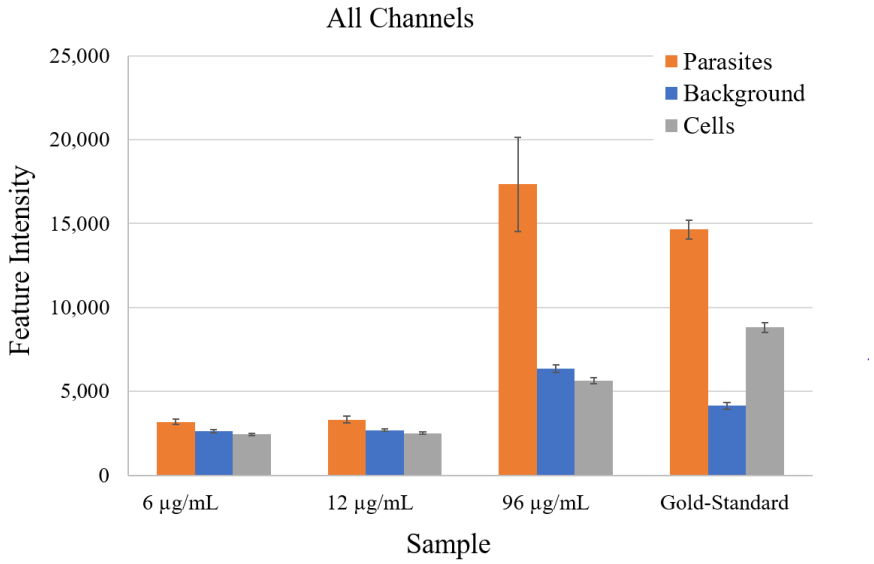

Figure 8: Average values of fluorescence features for various Acridine Orange stain concentration and smear types.

Although the overall fluorescence intensity of parasites was lower for those stained using 6 µg/mL and 12 µg/mL AO, the signal to background ratio of the latter still allowed for clear feature separability from RBC's and background, which is evident when feature intensities are normalized to parasite signal (Fig. 9). In smears generated in the microchannel, the RBC's appear darker than the channel background, while in the gold-standard images they appear brighter than the background (Fig. 10). This is likely due to

the ability of excess fluorophores to be washed away from glass-mounted gold-standard smears but not from microchannel smears.

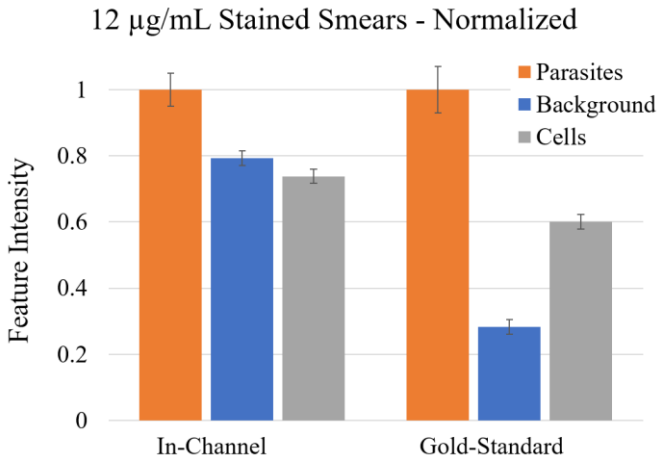

Figure 9: Normalized feature and background intensities for in-channel and on-glass (gold-standard) smears, each stained using 12 µg/mL Acridine Orange.

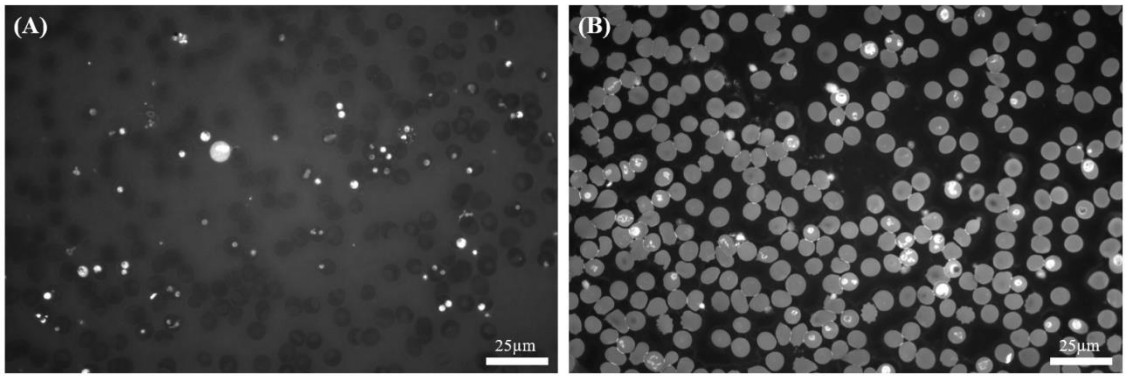

Figure 10: Monochromatic images of samples stained using 12µg/mL Acridine Orange (A) in the microchannel; and (B) on a glass slide (gold-standard). Images are shown with linear contrast enhancement for visibility.

Three independent repetitions of the entire in-tube staining and smear creation process were performed for the 12 µg/mL stain concentration to assess repeatability from channel to channel. As shown in Fig. 11a, average relative feature intensities of parasites, background, and RBC's remain consistent throughout the channel (error bars represent standard deviation of the variance in average feature values image-to-image). To better assess staining quality as defined by feature separability, intensities in each FOV were normalized to the intensity of the background to eliminate linear baseline drift that occurred as a gradient along the channel.

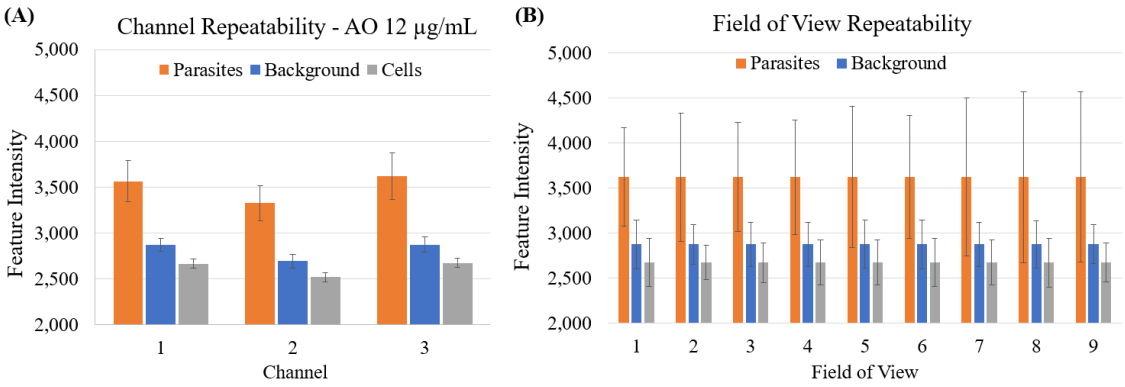

Figure 11: Variance of fluorescence staining. (A) Repeatability between separate, independent channels. (B) Repeatability of multiple fields of view within a single channel.

Feature intensity variance was also compared within and between individual fields-of-view (FOV) within the same channels (Fig. 11b). Across eight images taken consecutively down the channels, features displayed similar relative intensities across all FOV (error bars represent standard deviation of the variance of intensity values object-to-

object within each FOV). Due to the differential uptake of stain by parasite morphological features across various stages of development, a large standard deviation can be observed in the average intensities of populations of parasites from each FOV. However, the precision afforded by sampling multiple FOV allows for the clear separation between the average intensities of parasites, RBC's and background in all three channels. Despite this consistency in relative feature intensities within each channel, it was found that variance occurred between gross feature intensities. Most of the variance occurred as a baseline drift along the length of the channel, with the staining intensities appearing to increase linearly as the location in the channel became closer to the microchannel inlet (Fig. 12).

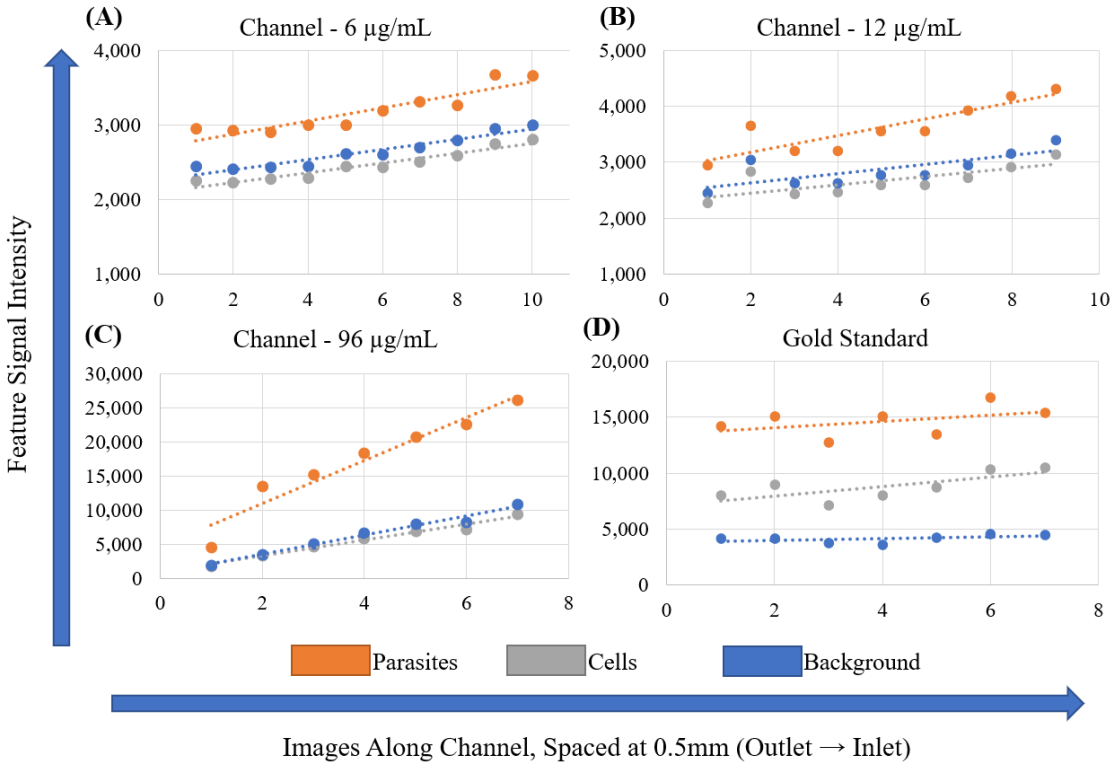

Figure 12: Change in overall signal intensities within individual channels for various stain concentrations: (A) 6 µg/mL, (B) 12 µg/mL, (C) 96 µg/mL, and (D) gold-standard dry smear, with each FOV being taken laterally along length of the smear.

Like most fluorophores, AO will photobleach as it is exposed to light during imaging, limiting the useful time in which imaging should be completed. To assess the rate of photobleaching that occurs in the imaging of channels, videos at 1 frame/second were collected for previously un-exposed FOV in every channel. Excitation light intensity was set to its maximum exposure power to ensure consistency. This exposure power was significantly higher than was used during channel imaging, and any reduction in exposure intensity will slow the rate of decay. The photobleaching rate observed in the channels follows an expected exponential decay trend (Fig. 13). Despite overlap in the standard

deviations of the parasite and background decay rates, there remained clear separability between parasitic and background intensities within each channel as far out as one minutes after photobleaching begins. Interestingly, as the concentration of stain increased, there was a reduced rate of decay in the signal-to-background ratio as photobleaching occurred, with 96 µg/mL actually showing maximum relative contrast approximately ten seconds after exposure began (Fig. 13c).

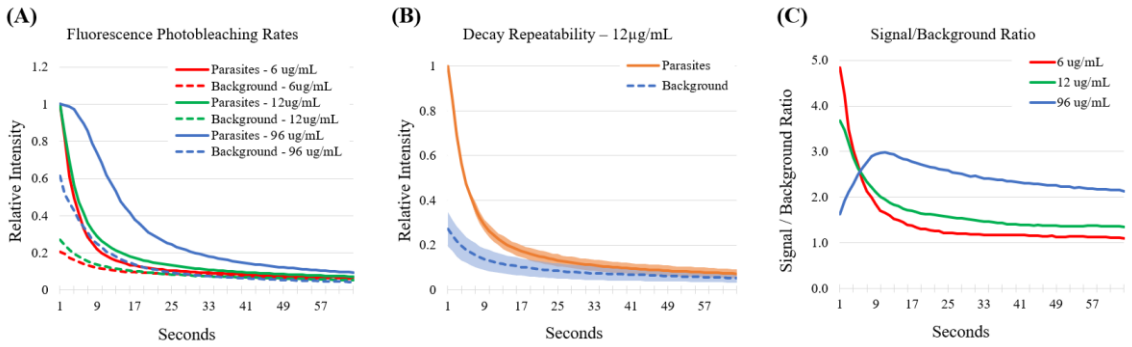

Figure 13: Photobleaching rate of fluorescent samples in-channel. (A) Photobleaching rates for various stain concentrations shown for parasites (solid lines) and background (dashed lines). (B) Parasitic average intensities (blue) and background fluorescent intensities (orange) with standard deviations plotted for 12µg/mL samples. (C) Signal to background ratio for each stain concentration plotted over time.

Discussion and Conclusions

In this work, various methods of peripheral human blood and *P. falciparum* staining were investigated using a novel, microchannel-based thin smear generation platform and traditional dry smear creation techniques. In-tube, wet staining techniques were employed and compared to the traditional gold-standard techniques of dried smears on glass to allow samples to flow inside of microfluidic channels instead of the traditional

dry blood staining. Staining quality was assessed quantitatively using intensity-based feature differentiation when imaged on a benchtop microscope, and results confirm that successful differentiation of *P. falciparum* malarial parasites from red-blood cells and blood plasma background is possible using staining in the microchannel and microscopic imaging. Clear relationships between stain concentrations and signal intensities were observed, and quantitative analysis of imaging results gave clear evidence that the results are repeatable.

While these initial results are encouraging, several potential drawbacks of utilizing microfluidically generated blood smears for portable microscopy were observed. Firstly, in their current state, the channels do not allow for cells to be immobilized at any point after the smear is created. While cells will usually cease to move as the capillary forces in the channel reduce and pressure is equalized, the smear will rapidly degrade if blood clots are not formed at the inlet and outlet of the channel to seal the fluid inside. Oftentimes, the smears will never reach a state homeostatic state, and cells will never cease moving for long enough to allow for images to be captured, making analysis of that entire sample untenable. Additionally, slight perturbations to the channel during use will induce a rapid shifting of cells within the channel, which is especially problematic when consecutive multimodal images are attempting to be collected for the same FOV.

Additionally, improvements must continue to be made to channel architecture if they are to be usable at the POC. Despite the presence of pillar structures that support the channel “roof” and aid in cell dispersion, it is common for cell density gradients to occur within the length of the channel, again making some samples useless if the anticipated

monolayer of cells is not achieved. These pillar features also do not consistently prevent the channels from collapsing, and it is common for the upper channel to bear down on the smear several minutes after creation, forcing cells towards the channel walls. This was especially prone to happen in cases when clotting did not occur rapidly enough at inlet and outlet. In line with this, success in operating the channels was highly dependent on the skill in depositing the sample at the exactly correct position within the sample inlet, a skill that proved difficult to master. An alternative to using a pipette to initiate smear creation clearly is needed.

Despite these drawbacks, it is believed that the combination of staining procedures and smear generation in a microchannel platform has the potential to improve the consistency and accessibility of high-quality blood films in both laboratory and remote settings, if the challenges can be overcome. As will be shown in Chapters 4 and 5, portable microscopy systems were successful in imaging successfully created microfluidic smears, indicating that the optical properties of the cartridges are favorable for use with POC microscopic malaria diagnosis and monitoring efforts.

CHAPTER III

NOVEL RAPID FABRICATION METHOD FOR LOW COST ASPHERIC PARABOLIC LENSES*

Introduction

In the course of researching possible low-cost lenses that could be used in the illumination system of a portable microscope, a novel, rapid fabrication method for aspheric lenses was discovered. While many modern engineers have access to rapid prototyping using in- house equipment such as 3D or circuit board printers, the optical engineer is typically relegated to much slower options for either prototypical or end-use applications. Additive techniques for rapidly generating lenses have been proposed in the literature, but typically require extensive polishing processes similar to traditional lens manufacturing techniques. This polishing sub-process can be prohibitively tedious and expensive for a rapid prototyping technique [114]. Rapid micro-lens production has been proposed by holding and curing a volume of liquid polymer in the desired shape using material surface tension and pressure to create lenses with maximum diameters typically of several millimeters [115, 116]. These systems range from single droplet extrusion [117], to leveraging the interface of two immiscible fluids [118], to the simultaneous production of full lens arrays

* Portions of this chapter are reprinted from: Wattinger, M., Gordon, P., Ghorayshi, M., & Coté, G. (2019). Method and system for the centrifugal fabrication of low cost, polymeric, parabolic lenses. Optics express, 27(15), 21405-21419. with permission from OSA.

(order of microns in aperture diameter) [119, 120]. While these micro-lens techniques avoid the need for any post-polishing processes, their reliance on forces of surface tension and sample pressures limit the theoretically maximum diameters possible, restricting applicability for many systems.

For a rapid lens fabrication system to be useful, it must be capable of producing lenses over a wide range of diameters and focal lengths, with controllable selection of the desired surface profile. It should produce lenses without a lengthy post-polishing step, in less than a day, with minimal costs, and should be useful with a variety of materials to allow for customization of the lens index of refraction. In this work, one such system is proposed, prototyped, and tested for potential utility as a lens rapid prototyping method.

Investigation of the Fabrication Principle

The proposed system builds from the operating principle of liquid mirror telescopes (LMT's). LMT's were first reported in 1909 by astrophysicist Dr. Robert Wood, who proposed and demonstrated a technique for shaping liquid metal into a highly uniform telescopic mirror [121]. LMT's are built using a rigid, cylindrical container filled with a reflective fluid that is rotated about its axis of symmetry at a steady velocity. The resulting surface is a very smooth paraboloid, which can be used as a collection mirror in telescopic systems with a large range of aperture diameters [122]. The surface roughness of these mirrors are in the same neighborhood as spin-coated objects, which avoid the need for any polishing steps [123]. The production of liquid mirrors for aerospace and

astrophysics applications has now been in development for over one hundred years [124-127].

This same general principle can be used to produce lenses of three distinct geometric forms, each with at least one parabolic surface whose curvature is regulated by angular velocity. To accomplish this, a rotating chamber is filled with uncured, optically clear polymer, which is then shaped by centrifugal force and cured while at a steady-state rotational velocity. The range of possible diameters is dependent only on the cavity diameter of the rotating chamber, which makes the aperture diameter arbitrary to the fabrication engineer. In some ways this process is similar to spin-casting from a mold, which is often used to produce meniscus contact lenses [128]. A model for lens production using this technique is presented along with corresponding experimentally manufactured lenses. A number of evaluation processes are used to evaluate the merit of the technique, and a final discussion addresses the limitations of the method.

The criterion for a lens to be classified as an asphere is dependent on the mathematical form of its surface height as a function of radial position, *r*. In particular, the surface height *z(r)* must take the form

$$z(r) = \frac{r^2}{R_{curv}\left(1+\sqrt{1-(1+\kappa)\frac{r^2}{R_{curv}^{\ 2}}}\right)} + \sum_i \alpha_i r^i \quad , \qquad \text{(Eq. 1)}$$

where $z(r)$ is an even polynomial with coefficients αi, when the i^{th} term has a degree greater than two. R_{curv} is defined as the vertex radius of curvature, and κ is the conic constant. The conic constant classifies $z(r)$, for various values of κ [129].

Physics of the Fabrication Technique

The system operates upon two physical mechanisms. The first is known as Bernoulli's rotation of fluid in a static cylinder, which is solely responsible for the aspheric nature and parabolic profiles of the lenses [130]. A derivation of the profile starts with the Naiver-Stokes equation (the fluid analog of Newton's second law), which describes the pressure field (P) of a body of fluid in terms of fluid density (ρ), its motion subjected to gravity (g), and acceleration due to rotation (a_{rot}),

$$\vec{\nabla} P(r,z) = \rho\left(g\hat{z} - a_{rot}\hat{r}\right). \qquad \text{(Eq. 2)}$$

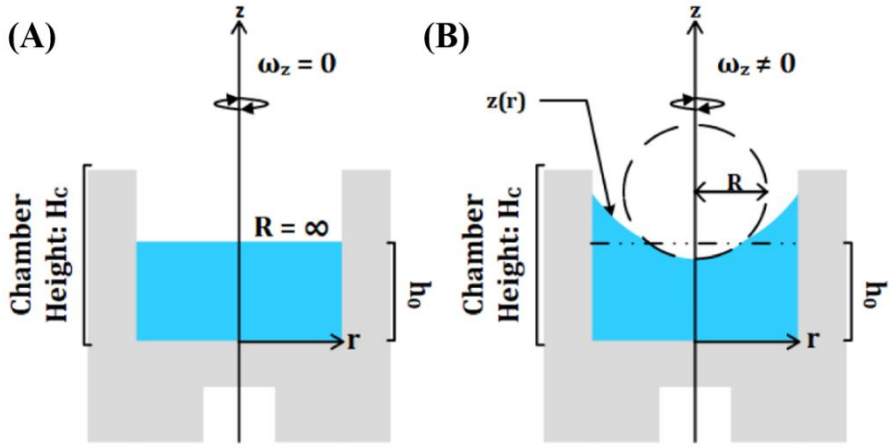

Figure 14: (A) Physical sketch of static layout, and (B) sketch of bodies undergoing rotation.

At a time prior to rotation, the fluid is static, as depicted in Fig. 14a. Rotation of the chamber results in a centripetal force directed inward at the axis of rotation. The cartoon in Fig. 14b, displays the fluid's opposing reaction, pushing the fluid toward the wall of the crucible. The resulting void is filled with atmosphere and causes a pressure gradient with the change in depth, resulting in the following equations of motion [130],

$$\frac{\partial \rho}{\partial r} = \rho \omega^2 r \ , \qquad \text{(Eq. 3)}$$

$$\frac{\partial \rho}{\partial z} = -\rho g. \qquad \text{(Eq. 4)}$$

Solving the second equation for ρ, and moving all the partial differentials to one side yields a single differential equation in z, and integration of this equation produces a single profile function $z(r)$, characteristic of the fluid height in the cylinder under steady state rotation [130],

$$z(r,\omega) = h_0 - \frac{D^2}{16R_{curv}(\omega)} + \frac{r^2}{2R_{curv}(\omega)}. \quad \text{(Eq. 5)}$$

In this equation, D defines the crucible diameter. R_{curv} takes on a physical relationship with the motor's angular velocity of rotation ω in units of radians per second and the gravitational constant [129],

$$R_{curv}(\omega) \equiv \frac{g}{\omega^2}\ ; \quad \text{(Eq. 6)}$$

$$\Delta R_{curv} = 2R_{curv}\left(\frac{\Delta\omega}{\omega}\right). \quad \text{(Eq.7)}$$

The uncertainty in R_{curv}, as it varies with speed is also defined in Eq. (7). Variances in the speed of rotation yield changes in the parabolic surface. Fig. 15 later depicts several different surface profiles that can be achieved for different rates of rotation. The

gravitational constant takes on the value 9800 mm-s^{-2}, adjusted from m-s^{-2} for the appropriate scale of the optics.

It should be emphasized that this work's focus is on the centrifugal lens production technique as a novel manufacturing method and thus uses the radius of curvature as one of the primary metrics of interest for evaluating the lenses. Other characteristics of lens quality such as wavefront error and aberration coefficients [131] are obviously more insightful parameters for evaluating lens quality, however they are left for future analysis as the goal of this paper is to prove the use of the described physical concepts toward lens-making. The R_{curv} is used because it highlights connections to the surface geometry of the lens, the velocity of the fabrication, and is used to build into other optical properties like focal length, etc.

This form of asphere is parabolic in nature. To determine the type of asphere this surface represents, simply substituting -1 for κ into Eq. (1) yields

$$z(r) = \frac{r^2}{2R_{curv}} + const. \qquad \text{(Eq. 8)}$$

Comparing the result to Eq. (5) verifies that the surface generated by this particular application is indeed an asphere of parabolic form. If higher order terms from vibrations and off-axis rotations are minimized, the profile should theoretically be axially symmetric. The possible effects of perturbations on the lenses will be revisited in the error analysis portion of the discussion.

The second mechanism to be considered is surface wetting that occurs at the boundary between the chamber, air, and liquid polymer. Surface tension continues to act on the fluid interface, but the strength of its interaction is dependent upon the speed of rotation. Vlado A. Lubarda treats this speed dependence rigorously in [132]. It is necessary to define a ratio between the standard capillary length (due to gravity) and an effective capillary length due to rotation of the fluid. This ratio is defined below and altered to represent the problem in terms of R_{curv},

$$\left(\frac{l_o}{l_\omega}\right)^2 = \frac{D\omega^2}{2g} = \frac{D}{2R_{Curv}}. \qquad \text{(Eq. 9)}$$

where l_o represents the standard capillary length due to gravity and l_ω represents the capillary length due to gravity.

The interpretation of this ratio (via Lubarda's results), implies that surface tension will be a contributing factor to the surface shape when the ratio is much larger than one. In other words, small diameter chambers at high speeds, or large diameter chambers at slower speeds will introduce variations in the surface profile via the effects of surface tension. As such, this study shall focus on the cases in which the rotational forces dominate over surface tension, for the sake of simplicity. This also means the minimum of the parabola should be at least 1-2 mm above the chamber bottom, for the same reason. One could certainly attempt to control the combined surface effects from surface tension and fluid rotation to produce variations from the ideal parabolic surface described by Eq. (8).

Accounting for the added complexity requires altering Eq. (5), an example of this process is demonstrated in [133]. To reiterate, when Eq. (9) is much greater than 1, the surface variation from Eq. (5) due to surface tension will be non-negligible. This would reduce an effective aperture of the fabricated lens well below the industry standard of 90 percent [134].

Theoretical Lens Performance

The high-end rotational velocity limit for lens production was selected based on the limiting amount of liquid in the crucible, derived in [130]. This upper bound on velocity can be thought of as a spilling limit as any motor velocities higher than this would result in fluid climbing up the walls and out of the container. For a given volume or initial fluid height, this maximum fluid volume can be modeled as

$$\nu_{\max} = \frac{2\sqrt{h_0 g}}{\pi D} = \frac{4\sqrt{gV}}{\left(\pi D\right)^2}. \qquad \text{(Eq. 10)}$$

Parabolic profiles described by Eq. (8) can form either concave or convex faces, depending on the manufacturing technique employed. For plano-convex cases, additional insight into capabilities of the manufacturing technique were gained through studying the lens R_{curv}, numerical aperture, and diffraction limits over the range of possible combinations of fabrication variables. Varying both the R_{curv} and focal length of this lens with motor velocity is described in Fig. 15b. These variances can be modeled using the

lens-maker's equation, which can be simplified by assuming that the second sides of the concave and convex lenses are planar, such that the second radius of curvature is infinite, thereby reducing the second radius term to zero. Thus, knowing that the R_{curv} varies with the inverse square of angular velocity, the focal length (f) of the lens can be related in much the same way using

$$\frac{1}{f} = \frac{(n_{mat} - 1)}{R_{curv}(\omega)} = (n_{mat} - 1)\frac{\omega^2}{g}. \qquad \text{(Eq. 11)}$$

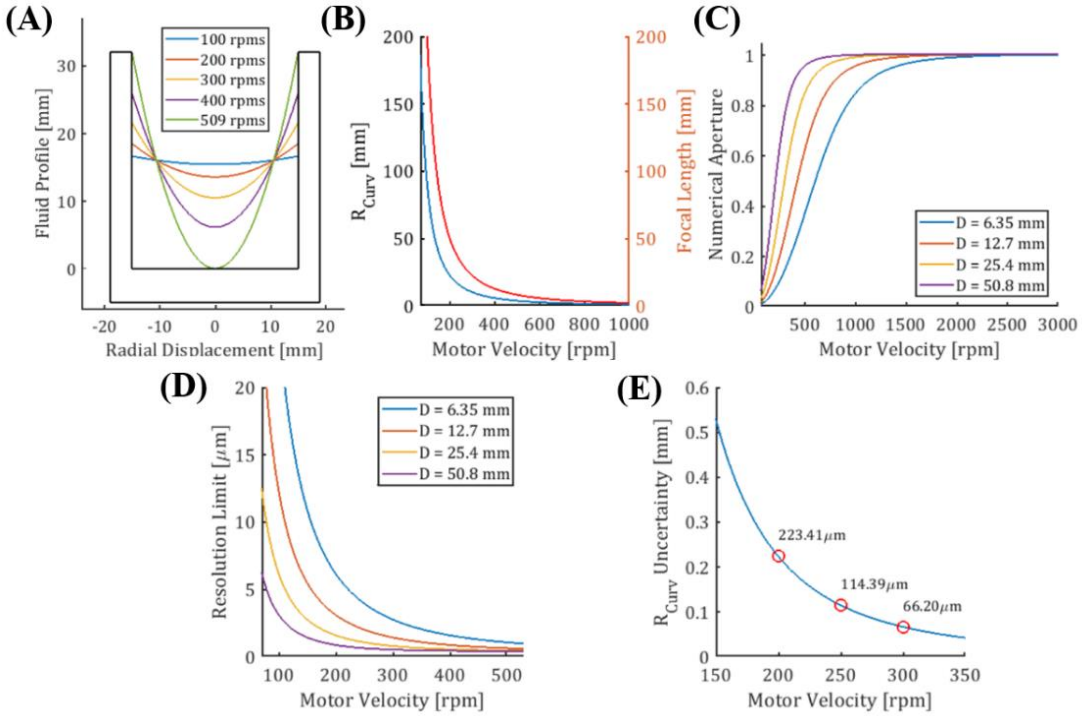

Figure 15: Mathematically derived lens properties: (A) surface profiles for a several motor velocities at a volume of 3 mL, (B) focal length and R_{curv} vs. motor velocity (C), NA vs. velocity (D), diffraction limit vs. velocity (E), and R_{curv} uncertainty vs motor velocity.

The diameter of the lens-spinning crucible and thus the diameter of the produced lenses may be freely chosen, establishing another degree of freedom within the lens selection process. Effects of variances in the lens diameter are analyzed using multiple curves to describe both the theoretically maximal numerical aperture (NA) and corresponding diffraction limit of each lens (each curve corresponding to a unique diameter) in Fig. 15(c) and 15(d). The NA of each lens is described as

$$NA = n_{air} \sin\left(\arctan\left(\frac{\omega^2 \left(n_{mat} - 1 \right) D}{2g} \right) \right). \qquad \text{(Eq. 12)}$$

Examining Fig. 15c for changes in NA with motor velocity, it should be noted that different volumes of liquid polymer in the chamber can shift each curve to the left or right. A confirmation for the accuracy of each combination of volume and motor speed is seen in the fact that each speed lies within the range of possible combinations dictated by the spill velocity in Eq. (10). Going one step further, it is predicted that the spill velocity represents the fastest lens per chamber diameter and liquid volume pair. Figure 15d summarizes the theoretical single lens diffraction limit capabilities of this manufacturing system. Using Rayleigh's criterion for defining the diffraction limit of this asphere requires two physical dimensions of the lens – aperture diameter and focal length [135]. By expressing the focal length in terms of rotational velocity, the diffraction limit is described as,

$$\ell_{\lim} = \frac{1.22 f \lambda}{D} = \frac{1.22 g \lambda}{\omega^2 \left(n_{mat} - 1\right) D} \qquad \text{(Eq. 13)}$$

where λ is the wavelength of light used for analysis.

System Design

The main requirements for physical system design were maintenance of constant motor velocity with small uncertainty, data collection, and minimizing axial disturbances during rotation. The system is composed of a LabVIEW graphical user interface, the electronics required to control the motor and collect data, a crucible which may be detached from a vertically rotating drive shaft, drive train connecting the drive shaft to an electric motor, and crucible heating component (a heat gun, in this case). The crucible consists of an aluminum cylindrical cavity with several small ejection ports in the base and a polished disc-shaped insert that is deposited into the bottom of the crucible prior to lens manufacture. The polished disc simultaneously provides a polished surface to mold lenses against and the ability to eject lenses from the crucible once they are cured. The arrangement of the system is depicted in Fig. 16a.

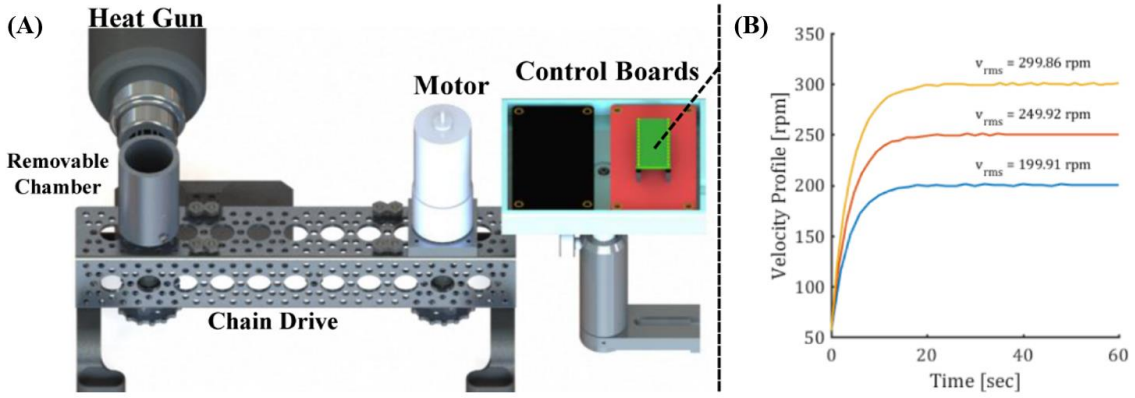

Figure 16: Prototype fabrication system: (A) CAD model of the fabrication system. (B) Experimental motor velocity data gathered over time using 8-bit speed encoder.

For motor velocity control, a proportional, integrative, and derivative (PID) feedback control scheme was implemented [136]. After locating the proper PID coefficients, a sweep of viable motor speeds was performed to verify that the RMS speed was constant over the range of 200 to 300-rpms as depicted in Fig. 16b. **C**onstant motor velocities were achieved between 80-1000-rpm. Over the range of velocities from 70 to 300-rpms, the PID tuning achieved a minimal variation in root-mean-square (RMS) velocity of ± 1 rpm, corresponding to the velocity profiles captured in Fig. 15e.

Fabrication Process

Sylgard 184 polydimethylsiloxane (PDMS) was chosen to demonstrate the system capabilities although the system has applicability for a variety of materials. The thermo-set polymer was prepared externally from the system by combining the standard of 10 to 1 base to curing agent in volumes that correspond to a desired lens thickness. Once prepared, a thin layer of PDMS may be deposited and cured onto the still base surface of

the polished disc to provide a smoother planar surface to mold lenses against. Uncured PDMS for the lens is then deposited into the aluminum cylindrical chamber, which initiates the fabrication process. The crucible is accelerated by the motor until the desired angular velocity is reached. Once steady state velocity is achieved, a uniform parabolic surface manifests across the liquid polymer, as a direct consequence of the centrifugal pressure field generated at the PDMS-air interface.

The heat gun is then turned on, and the crucible reaches a constant temperature profile of approximately 150ºC after four minutes. The duration of this heating varies depending on the volume/thickness of lenses desired. After heating is over, the heat gun is turned off, and the crucible is removed from the motor shaft and allowed to cool on a large metal countertop for 10-12 minutes to room temperature (approximately 21ºC). The removable aluminum platform and cured lens are elevated up and out of the chamber. The lens is then carefully detached from the face of the removable aluminum platform and is thereafter only handled by the sides of the cured elastomer, as shown in Fig. 17c. This process yields a single planar-convex aspheric lens, over the span of about a half hour in total (not including material prep), most of which is spent heating and cooling the chamber. Each step of the process is illustrated in Fig. 17.

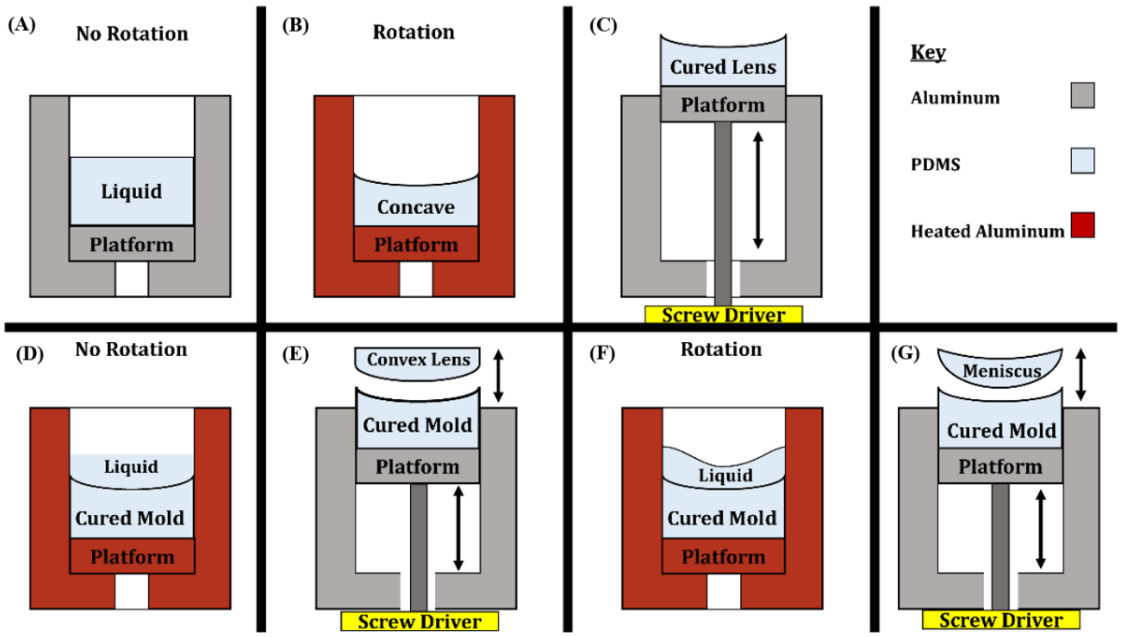

Figure 17: (A) Cross section of lens fabrication process: concave lens prep (B), concave lens cure step (C), and concave lens ejection. (D) Alternative process: convex lens cure, (E) convex lens ejection and removal from mold. (F) Alternative process: meniscus lens cure, (G) meniscus lens ejection and removal from mold.

The described procedure yields a plano-concave lens. Procedures for generating plano-convex and meniscus geometries use the planar-concave lens as a casting mold. After the mold is prepared, uncured PDMS for the second lens is injected into the chamber-mold ensemble. To produce plano-convex lenses, the chamber is kept static (not rotating), and a homogeneous heating condition is applied to initiate lens curing. Heterogeneous heating during this step was found to produce surface irregularities in the planar face due to thermal expansion. It was also found that lower temperatures and longer curing times reduced incidence of such abnormalities when casting PDMS lenses. To create a meniscus lens, the entire crucible containing cured mold and uncured PDMS is

instead rotated and cured using the heat gun as previously described for the plano-concave case. After the secondary lenses are cured, they can be carefully peeled from the concave molds, generating a perfect casting of the concave surface on a now convex surface. Vapor-deposited mold release may be used to improve the ease of lens separation, but it was found to compromise surface roughness and was not necessary to separate lenses from each other.

At this point, it may be considered what effects of viscosity and spatial thermal gradients within the liquid polymer play into the thermoset curing process. Because the rotating fluid is ideally a hydrostatic problem (see Eq. (2)), viscosity does not explicitly appear in Eq. (5). Viscosity's role arises when any mechanical vibrations or eccentricity (chamber axis tilt) occurs, causing fluid to flow. In this case higher viscosity is favorable, since it dampens small amplitude vibrations, preventing them from appearing on the lens surface. Slow, homogenous heating throughout the PDMS is preferable to prevent surface irregularities which may arise due to uneven curing and thermal expansion. A Seek thermal imaging camera was used to observe the heat propagation within a curing lens and to reposition the heat gun to ensure homogenous sample heating.

Fabrication Results

The independent variables controlled for this technique were the liquid polymer volume, rotational velocity, heating profile, and lens geometry. The curing temperature of the heat gun was held constant at 150 ºC, cavity diameter held constant at 25 mm, and liquid PDMS volume held constant at three milliliters. Five lenses made for each planar-

concave and resulting planar-convex case according to the parameters laid out in Table 5. It is important to note that each concave mold was produced for every repetition of a planar-convex lens in order to see how repeatable the system was in generating desired optical characteristics. Samples of both concave and convex lenses for each speed are shown in Fig. 18.

Table 5: Lens fabrication test cases and relevant metrics.

Motor velocity (rpm)	Radius of curvature (mm)	Convex lens thickness (mm)	Focal length (mm)
200	22.341	7.825	55.853
250	14.298	8.789	35.746
300	9.929	9.967	24.823

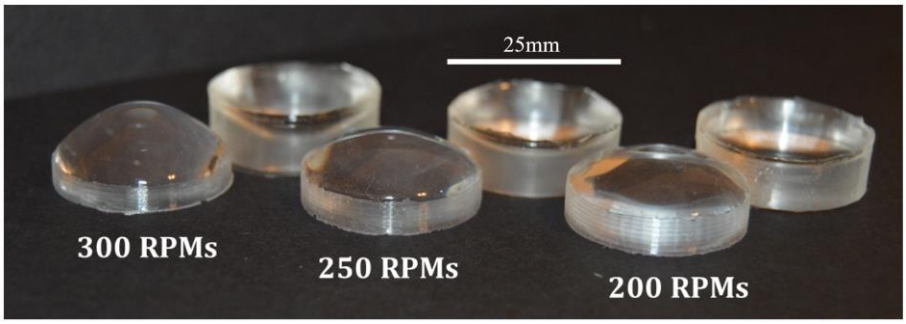

Figure 18: Showcase of fabricated lenses. The planar-convex lenses are situated in the front row, each cured under static conditions, with the adjacent planar-convex mold/lens responsible for its production in the back row to its right.

Lens Quality Measurements

To assess lens R_{curv}, a Zygo white light interferometer was used. Several caveats for the interferometric method must be addressed. Firstly, surfaces of parabolic form have

steep surface gradients, causing fringe density to increase very rapidly with radial distance from the vertex until it exceeds the resolution of the imaging system. The result is that the scannable area of these lenses is confined to a maximum of 1.5 mm^2 across the apex of the lens, limiting the amount of information that can be gathered for the overall lens profile. However, it does provide high-confidence validation of R_{curv} and thus confirmation of the theoretical model and overall method of lens manufacture. To gather information for the shape of the entire lens surface, a Mitutoyo PH-A14 profile projector was also used to project a focused shadow of the lens onto an electronic coordinate measuring system. The system's lateral resolution was 2.54 microns, and surface profile height was collected every 254μm across two orthogonal profiles for each lens. This method provides bulk profiles spanning the full diameter of the lens, and while having less sampling precision than an interferometer, the data can be accurately fit to an aspheric equation used to solve for R_{curv} and the conic constant of the lens.

A Bruker Dimension Icon atomic force microscope (AFM) was used to characterize the RMS surface roughness of the lenses. The point of this measurement is to identify the typical surface roughness produced at each interface in aggregate over several lenses with the same fabrication conditions. Two unique surface types are of interest for surface roughness – statically cured and dynamically cured surfaces. It was shown that PDMS surfaces molded against another take on the same surface roughness as the original surface. If intrinsically low surface roughness can be demonstrated for these lenses, undesirable post-polishing steps may be avoided. The RMS roughness of each interface is then compared to industry standards. The equation for surface roughness is defined as,

$$R_q = \sqrt{\frac{1}{NM}\sum_n \sum_m \left(z(n,m) - \bar{z} \right)^2}. \qquad \text{(Eq. 14)}$$

Where z-bar is the average surface height of a grid of discrete heights z(n,m), such that n is the row index, and m is the column index. N and M make up the total number of rows and total number of columns in the grid respectively.

Lens quality and performance was also assessed by collecting images that will show changes in magnification and resolution capabilities for each lens that result from the varying focal distances and radii of curvature. Images of a negative contrast 1951 US Air Force Target (USAFT) were collected, using each fabricated convex lens as a single-unit objective. Polymeric lenses from the study were fitted into lens tubes and attached as replacement objectives for an inverted brightfield microscope, and images of the AFT were collected using a 16-bit monochromatic sCMOS camera. Measurements for R_{curv} were taken for each of the convex lenses across all three rotational velocities in order test the correlation between angular velocity and the respective optical parameters as theorized. For each of the three speeds, five lenses were tested for repeatability. Fig. 19 contains information for R_{curv} as well as a sample of the bulk profilometry results.

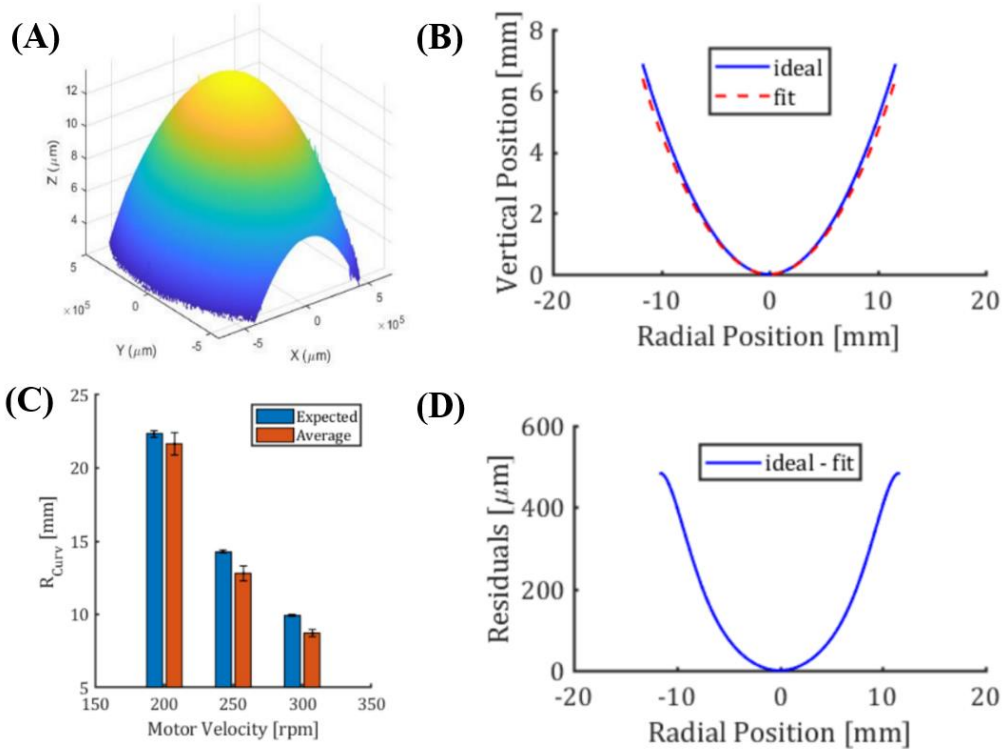

Figure 19: Lens vertex profile and R_{curv} measurements: (A) 200-rpm lens apex profile found using interferometer, (B) average of measured R_{curv} against theoretically predicted values, (C) aspheric fit line and theoretical profile for 300 rpm projected profile, with conic constant k=-0.99960 and R_{curv} = 10.5310, (D) and the error (absolute difference) between the aspheric fit line and the ideal profile.

Fig. 19a shows an interferometrically measured lens apex depicting excellent surface roughness and uniformity across the region. Each fabricated lens was measured and the Zygo software computed R_{curv} for each profile. Figure 19c contains the average R_{curv} values over a set of five lenses of the same motor velocity compared to the corresponding theoretically expected values. The error bars in the expected cases are the theoretical uncertainty in R_{curv} displayed in Fig. 15(e). The error bars associated with the averages are the standard deviation in radius of curvature of lenses fabricated from a single

speed. The deviation across different speeds decreased according to the trend predicted in Fig. 15(e). In all cases the measured R_{curv} were systematically smaller than what the model predicted, with the differences between experimentally measured and the theoretically predicted R_{curv} being 0.8604 mm, 1.4905 mm and 1.1216 mm for the 200, 250 and 300 rpm cases, respectively. The larger-than-expected deviations and smaller radii of curvature suggest the presence of minor variables in the fabrication prototype not accounted for by the theoretically perfect physical model of the system.

Each bulk profile slice gathered using the profile projector was processed in MATLAB to acquire a well-conditioned aspheric fit. The conic constant, radius of curvature, and the first three higher order even polynomial coefficients were obtained using MATLAB's built in least squares regression curve fitting employing the Levenberg-Marquardt algorithm. Pre-processing the data (prior to fitting), consisted of translating the coordinate system to align the origin to the parabolic apex and truncating the last 2-3 points on either side of the profile to ensure equal length between ±X distances. The aspheric parameters for each profile are listed in Table 6.

Table 6: Aspheric fitting parameters of 2D lens profiles (shadow measurements).

Speed (RPMS)	Lens Number	Orientation (Degrees)	R_{CURV} (mm)	κ	α_4 (r^4)	α_6 (r^6)	α_8 (r^8)
200	1	0	25.2468	-0.99720	1.22 E-05	-2.40 E-07	2.18 E-09
		90	22.9102	-1.00300	-9.16 E-05	1.42 E-06	-6.26 E-09
200	2	0	23.3990	-1.00420	-5.55 E-05	7.82 E-07	-2.48 E-09
		90	22.9208	-0.99670	-8.78 E-05	1.23 E-06	-4.24 E-09
250	1	0	14.3235	-1.00060	-1.21 E-04	1.51 E-06	-5.99 E-09
		90	15.0187	-1.00190	-2.89 E-05	1.70 E-07	6.30 E-11
250	2	0	15.8829	-0.99860	4.65 E-05	-9.35 E-07	5.13 E-09
		90	16.1768	-0.99980	3.53 E-05	-4.94 E-07	2.52 E-09
300	1	0	9.9468	-0.99870	-1.66 E-04	2.22 E-06	-9.06 E-09
		90	10.5313	-0.99960	-3.70 E-06	-2.72 E-07	1.93 E-09
300	2	0	10.4332	-0.99940	-2.92 E-05	2.26 E-07	-5.58 E-10
		90	10.1842	-0.99970	-9.04 E-05	1.07 E-06	-4.40 E-01

Each of the 2D profile slices produced a conic constant of negative one, indicating that the slices are indeed parabolic, as predicted by Eq. (5). This result was only achieved once the fitting algorithm incorporated the additional even polynomials, which increased the fitting constrains of the problem. The measured radius of curvature values varied in the opposite trend from Fig. 19b; in this case they were almost always larger than the expected value, although the error between the expected and measured values did decrease

with the increase in speed (as expected). Also, between profiles from the same lens (0 to 90 degrees), the radius of curvature varied, suggesting either systematic error in the measurement technique or lens astigmatism not shown by the interferometric measurements. It is hypothesized that minor axial tilt (even on the micron scale) affects the computed radius of curvature values. These data validate the fabrication technique's ability to produce the desired parabolic profiles across the lens surfaces.

RMS surface is another important parameter for overall lens quality and was assessed using atomic force microscopy for both static and dynamic surfaces. Examples of the surface profiles per interface are described in Fig. 20 below. Each profile samples a square with a side length of 10 µm. Lens results compared to commercially available lens surface roughness can be seen in Table 7 (data adapted from Edmund Optics technical specifications [137]).

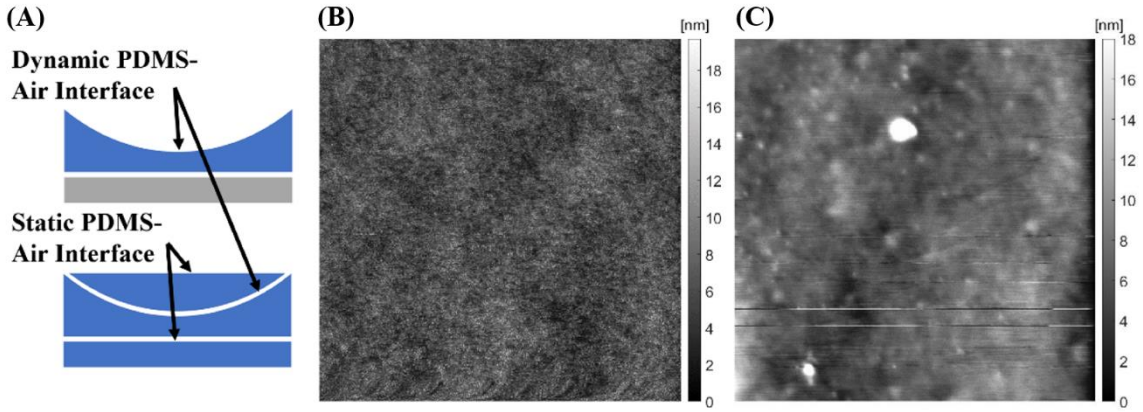

Fig. 20: (A) Diagram of surface interface varieties, (B) Surface roughness map for dynamic air-PDMS interface with area of 10x10 µm, (C) Surface roughness map for static air-PDMS interface with area of 10x10 µm (c).

Table 7: RMS roughness measurements and industry standards. Adapted from Edmund Optics technical specifications [137].

Lens Surface	RMS Surface Roughness (nm)
Edmund Optic – Typical Lens	5.0
Edmund Optic – Precision Lens	2.0
Centrifugal PDMS Lens - Dynamic	2.3
Centrifugal PDMS Lens - Static	1.58

Convex lenses molded inside the spun concave lenses were used to image the USAFT in order to demonstrate their utility towards single-lens imaging and to validate their performance. ImageJ was used to select the smallest resolvable group element on the target. Fig. 21 contains images from typical lenses for 200rpm, 250 rpm and 300rpm lenses, in which the resolving ability and magnification clearly increase as the rotational speed increases. This validates the theory described earlier which indicates that R_{curv} and focal length will decrease with increasing speed, leading to higher NA lenses and, thus, better resolution.

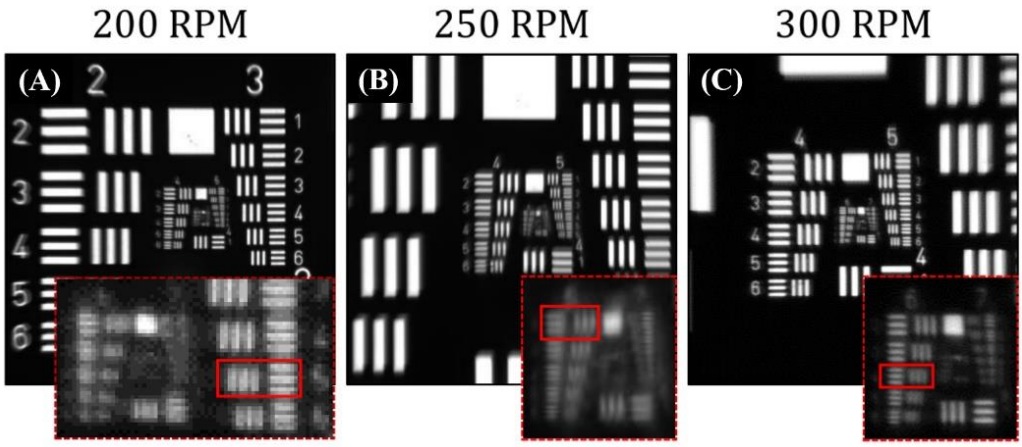

Figure 21: USAFT images for (A) 200-rpm, (B) 250-rpm, and (C) 300-rpm, which resolve elements 5-5, 6-2, and 6-5, respectively. Uncropped images presented, with magnified subsets below each.

Sources of Error

Lens R_{curv} displayed good agreement with parabolic profiles as predicted by the theoretical models. It was shown that the precision of R_{curv} decreased as the fabrication velocity increased, as predicted by the uncertainty defined in Eq. (7). However, discrepancies exist between predicted R_{curv} values and experimental measurements from the interferometer. All measured values of R_{curv} are consistently less than the model-predicted values for the corresponding speeds, which suggests that either the model is overly simplistic or there is a systematic error occurrence during fabrication.

Possible sources of error identified within the system are velocity control of the motor, misalignment between crucible and drive shaft axes of rotation, control of volume of uncured polymer deposited in the crucible, and possible thermal gradients present within the material. As previously discussed in the system design section, the uncertainty of the RMS motor velocity for all 3 speeds was measured at 1 rpm. Using propagation of

error, it was found that any misalignment between the chamber and the rotating shaft can introduce precession for the container. This effect has already been modeled in [138], and its effects can be captured by analyzing influence on the rotational velocity. The effect of the eccentricity on the rotation speeds can be summarized by Eqs. (15-17), upon the condition that the angular displacements occurring during precession are no larger than 3-5 degrees (so the small angle approximation can be employed).

$$\omega_z \cong \omega \tag{Eq. 15}$$

$$\omega_r \cong \varphi\omega \tag{Eq. 16}$$

$$\frac{\Delta R_{curv}}{R_{curv}} = 2\sqrt{\left(\frac{\Delta\omega}{\omega}\right)^2 + \left(\Delta\varphi\right)^2} \tag{Eq. 17}$$

The tilt in φ of the radial axis can affect the magnitude of the uncertainty. At a maximum angular displacement of 5 degrees, the second term dominates, and produces an uncertainty 4-5 times R_{curv} for a particular speed. The actual angular displacements witnessed during the precession of this particular chamber were roughly 1-3 degrees off-axis, which could account for R_{curv} discrepancies between theoretical and measured values.

Inspection of cured lenses revealed an occasional anomaly in the fabrication results. Several lenses display a rotationally symmetric discontinuity that varies in

diameter and uniformity across samples. Examples of lenses both with and without this "ring" can be viewed in Fig. 22. The leading hypotheses for ring appearance are based on suspected inhomogeneous heating of uncured polymer during fabrication. This could affect lens quality by inducing the phenomena known as vorticity rings, which can occur as thermal gradients cause convection-flow that drives fluid up and radially outward towards the walls of the crucible, giving rise to a toroidal vortex within the polymer [139]. Another possibility is that the uneven heating of fluid causes subtle abnormalities in the lenses due to the thermal expansion of the PDMS. Further tests to control internal thermal gradients are needed to test this hypothesis.

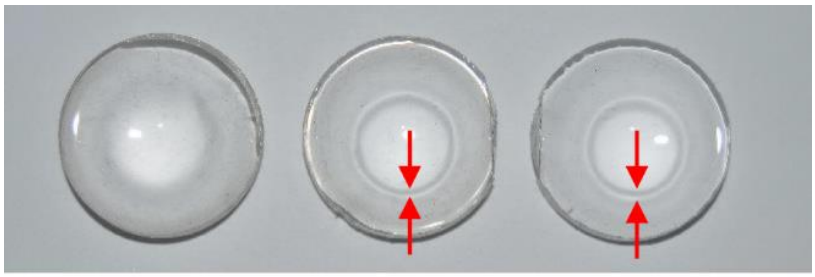

Figure 22: Top view of three convex lenses all fabricated at 300 rpms demonstrating the presence of rings. Leftmost lens is an example without a ring. The middle and rightmost lenses contain the ring feature, indicated by the arrows.

Discussion

The lenses produced appear to exhibit excellent clarity across their entire width. Obviously, the overall clarity and refractive properties are largely dependent on the material used to fabricate the lenses. Although only PDMS was used to demonstrate the system capabilities, other compounds including other thermoset polymers as well as

photo-cure or chemically cured materials could just as easily be used. Use of photo-curable polymers offer promise because they can avoid possibly detrimental effects of material thermal expansion during curing. Each PDMS lens costs an estimated 40 cents/lens to produce, with the possible cost of any lens produced tied directly to its bulk material cost. The polymeric lenses exhibit flexibility when compared to glasses, but mechanical properties could be easily manipulated to suit the appropriate needs by varying the material composition. Indeed, the deformability of lenses may have intrinsic value for adaptive optics applications. It is also worthy of note that care must be taken to prevent dust from adhering to the lens surfaces due to static charge accumulation.

Overall, the surface qualities produced by this method exhibit excellent RMS surface roughness. Results of the AFM measurements show that the dynamic air-PDMS interface has a higher RMS roughness than the static air-PDMS interface, which seems logical, as the dynamic case adds opportunities for mechanical vibrations or axial asymmetries of rotation to perturb the surface as it is curing. The typical roughness value for microscope precision optics is on the same order of magnitude as the typical roughness induced from the prototype fabrication system, without the need for any precision polishing, which is a significant advantage for lenses generated using this method.

Conclusions

In this study, a method and system for the production of polymeric aspheric lenses in concave, convex, and meniscus forms with a range of customizable parabolic profiles was demonstrated. The physical phenomenon was modeled mathematically and

implications on lens R_{curv}, focal length, diffraction limit, and numerical aperture were described. Lenses were produced for several test cases, with results that generally validate the constructed models. The surface quality of the lenses was assessed via RMS roughness using an atomic force microscope, with statically and dynamically cured surfaces showing surface roughness values comparable to those reported for precision tier optics in industry. Lens profiles showed consistently parabolic conic constants with some variability in radii of curvature. In some lenses, a surface anomaly was observed, and a source was hypothesized to be thermally driven curing abnormalities.

Overall, the proposed lens manufacturing technique has potential to be able to rapidly produce aspheric lenses with comparable quality to current manufacturing technologies, but more sophisticated mechanical and thermal control are merited to improve the precision and consistency of lenses produced. Although they do not meet the exact specifications needed for use in the illumination of the portable microscopy systems as described in Chapters 4 and 5, the lenses could theoretically be used in future optical systems, especially for non-imaging applications where the ring artifact would not induce significantly noticeable degradation in lens performance.

CHAPTER IV

PORTABLE BRIGHT-FIELD, FLUORESCENCE, AND CROSS-POLARIZED MICROSCOPE TOWARD POINT OF CARE IMAGING DIAGNOSTICS*

Background

To broaden the functionality of point-of-care devices towards diagnostic utility and translational potential, this work presents a new configuration of a portable microscope capable of gathering images in brightfield, fluorescence, and cross-polarized modes and transmitting the data wirelessly to any web-browser enabled device for viewing and processing. Numerous portable microscopes have previously reported bimodal functionality, most commonly pairings of either brightfield/darkfield or brightfield/fluorescence imaging [41, 140-146]. However, combinations of three or more imaging modalities have been almost exclusively relegated to sophisticated benchtop instruments [147-152]. On the benchtop, combinations of brightfield, fluorescence, and cross-polarized imaging have been validated, yet never translated into portable configurations for use at the point-of-care [153, 154]. This system, designed using off-the-

* Portions of this chapter are reprinted from: Gordon, P., Venancio, V. P., Mertens-Talcott, S. U., & Coté, G. (2019). Portable bright-field, fluorescence, and cross-polarized microscope toward point-of-care imaging diagnostics. Journal of Biomedical Optics, 24(9), 096502. and Branan, K., Gordon, P., Dogbevi, K. S., & Coté, G. L. (2020, February). Thin-film plastics used in microfluidic channels for microscopy imaging in low resource settings. In Optics and Biophotonics in Low-Resource Settings VI (Vol. 11230, p. 112300M). International Society for Optics and Photonics. with permission from SPIE.

shelf optical components, is easily adaptable to the needs of a variety of imaging tasks, making it, to the authors' knowledge, the first published example of a portable, customizable, tri-modal microscopy platform. It is designed with the potential for automated imaging and processing of thin-smear samples that may be produced in microfluidic cartridges to achieve consistency in sample preparation, a necessary step to making point-of-care microscopy robust and repeatable with minimally trained workers in the field [155]. Thus the proposed microscope attempts to create a point-of-care technology that partially satisfies the World Health Organizations ASSURED criteria [156]. Indeed, it is hoped that disclosure of this tool may facilitate investigations of an integrated tri-modal microscopy approach to malaria diagnosis.

The proposed microscope will be designed to maximize the amount of useful diagnostic information that is able to be collected in low-resource settings by minimally trained healthcare workers by using a low-cost, automated approach. Disease confirmation can be determined by observing the presence of trophozoites in the blood, which can be done in either brightfield or fluorescence contrast mode. It is expected that the sensitivity of parasite detection will be determined not by the optical system, but rather by the sample preparation, as the limit of detection for thick vs. thin blood smears has been well documented in the literature [157-159]. Parasitemia will be assessed by mapping the cell boundaries using brightfield mode, then detecting the presence of DNA in the bloodstream using fluorescent imaging mode to detect fluorophores that are bound to double-stranded nucleic acids. The total number of red blood cells found to contain DNA will be divided by the total number of red blood cells surveyed to measure parasitemia, and false-positives

due to DNA in white blood cells will be ignored by the image processing software due to the greater size and uniformity of DNA in white blood cells when compared to *Plasmodium* parasites.

Typically, species differentiation is done by observation of gametocyte morphology in the gold-standard test, but other pathological differences can also be used to discriminate between species in a multi-modal detection scheme. *P. falciparum*, the most common and deadly species of infections, produces dual-rings in red blood cells with higher rates than other species, and also has a higher rate of red blood cell sequestration in peripheral blood vessels [34, 160]. Additionally, there are characteristic differences between erythrocytic schizogony synchronization between each species, and each species produces hemozoin crystals with characteristic sizes and shapes, differences which may be detectable using cross-polarized imaging [50, 72, 73, 77, 87]. It may also be possible to tag species-specific chemical biomarkers such as histidine-rich-proteins so that the species of infection could be determined by measuring spectral differences in images of blood smears [161].

The final potential advantage of using a tri-modal microscopy approach is that it may be possible to better inform how likely a patient will be to progress rapidly to a complicated state of infection, potentially saving lives for those whose need for urgent high-dosage treatment might not be readily apparent from a parasitemia measurement alone. Malaria can progress at very different rates in individuals depending on their level of immunity and other risk factors [162]. Some patients who are immune have long-standing latent infections and would not be a candidate for complicated interventions.

Such a person might be more likely to have an accumulation of hemozoin crystals in their bloodstream, whereas a non-immune individual would express symptoms much sooner in the disease progression, meaning that a lower-than-average amount of hemozoin in the blood stream for a given parasitemia and fever could indicate that a patient may progress to a complicated state more rapidly and should therefore be transported to a health facility [23]. These differences in hemozoin accumulation could be detected by the cross-polarized imaging of the multi-modal microscope.

The microscope will be designed to communicate wirelessly with any web-enabled personal electronic device, on which automated image processing software can analyze images and provide results to the user, minimizing the amount of skill necessary to operate the diagnostic system. If, however, after the microscopy system is developed, it is unable to provide the detection sensitivity or speciation reliably, it may still provide value as a low-cost augmentation of RDT-based diagnosis, where the RDT is used for detection and speciation, while the multimodal imaging system provides parasitemia information and informs the risk of complication in the patients [66].

Optical System Configuration

The overall microscope configuration is depicted in Fig. 23. Both epi and transmission illumination are available, depending on the imaging mode desired. A 3-D printed housing holds elements of the simplified Köhler transmission illumination system, in which light from a warm-white LED (XREWHT-L1-R250-009F7, Cree, USA) is collected by a singlet asphere condenser lens(ACL25416U, Thorlabs, USA), transferred

through a field diaphragm, and, after being folded 90° by a plane mirror (PFSQ10-03-P01, Thorlabs, USA), is passed through a linear polarizer sheet (PS030-R15, MidOpt, USA) and condenser aperture before being focused onto the sample plane by a second identical asphere, with NA of 0.79.

In epi-illumination mode for fluorescent imaging, light from a blue 485nm LED (XPEBBL-L1-0000-00301, Cree, USA) is collected by a similar singlet asphere, passed through an excitation filter (#67-028, Edmund Optics, USA), reflected off of a dichroic mirror (#67-080, Edmund Optics, USA), and condensed onto the sample plane through the microscope objective. Both LEDs are driven at 3V forward voltage, resulting in expected luminous flux output of 80 lumen from the white and 45 lumen from the blue. From the sample, image-encoded light is collected by the objective, passed through the dichroic mirror and one of three available filters in infinity space, then focused onto the camera by a tube lens with 100mm focal length (TTL100-A, Thorlabs, USA). A third-party, reduced focal length tube lens was chosen to reduce optical system path length and because such a lens is more likely to be useful with objectives from a variety of manufacturers. Both the imaging and transmission illumination paths are folded using planar mirrors to reduce the overall footprint of the system, and Zemax raytracing software was used to confirm lens choice and system layout dimensions.

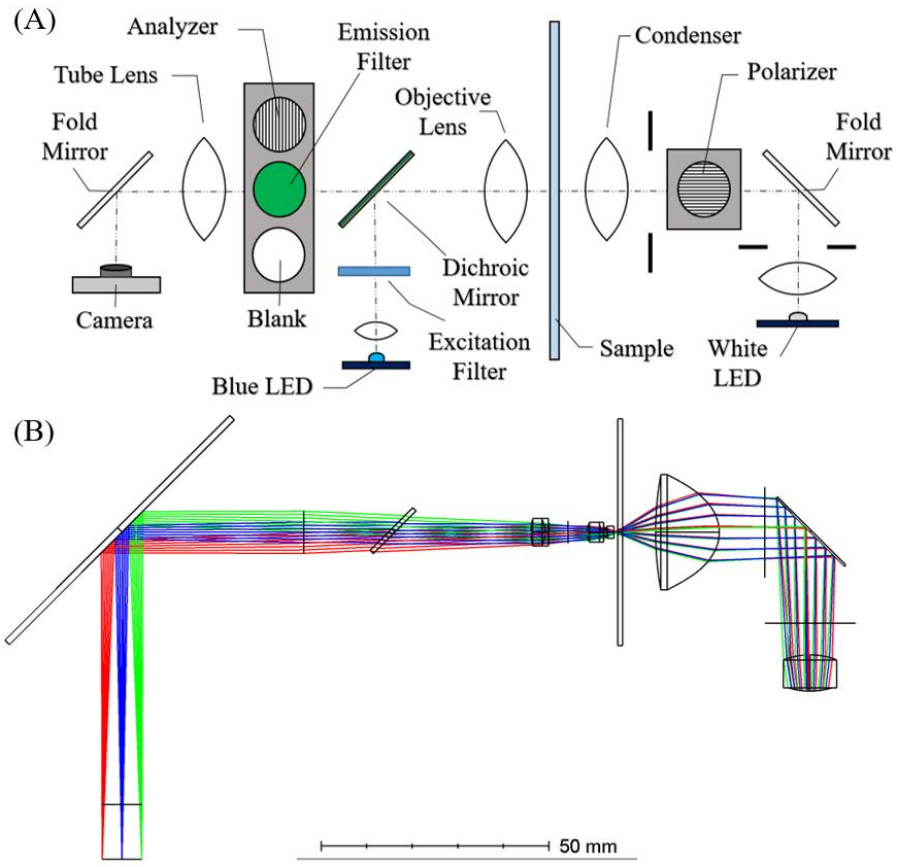

Fig. 23: Design overview of portable microscope system. (A) System layout diagram, (B) Zemax raytracing of folded optical system.

Generation of Multimodal Contrast

In this configuration, the microscope can gather images in different contrast modes without moving the sample focus or alignment. In order to select which mode of imaging is used, the only changes necessary are to activate the appropriate LED source and select the proper filter from the sliding filter deck. To generate brightfield images, the transmission illumination, warm-white LED is activated and a blank space in the filter deck is selected. The polarizing filter and dichroic mirror are by default kept in the optical path, which pre-filters all light reaching the sample in brightfield imaging to be linearly

polarized and filters all light reaching the camera to be of wavelengths longer than the dichroic cutoff. This places an inherent limitation on the amount of chromatic information available in brightfield imaging but can be compensated by using simple post-processing to recreate images in a traditional color-space by interpolating information from missing color channels. Alternatively, if the information contained in wavelengths shorter than the dichroic cutoff is critical for a particular test, the dichroic filter can easily be removed from the system but must be replaced prior to collection of fluorescent images. In fluorescence imaging mode, a board mounted blue monochromatic 485nm epi-LED is activated and fluorescent emission filter (#67-031, Edmund Optics, USA) selected from the filter deck. These excitation and emission bands were selected because most prevalent fluorophores used in malaria diagnosis utilize FITC excitation/emission wavelengths with cut on/off at 500nm, although any visible excitation and emission bands may be used [56]. For cross-polarized imaging, the transmission LED is activated and analyzing filter selected from the deck. When transmission illumination is used, all light passing through the system is also linearly polarized by default, as the polarizing filter is permanently kept in the Köhler illumination system.

It was discovered, both in literature and experimentally, that the dichroic mirror will reduce the cross-polarized signal intensity unless the polarizer and analyzer are carefully aligned with the orthogonal vertical or horizontal axes of the dichroic mirror to minimize imparted elliptical polarization states by the mirror [122, 163]. The full range of possible polarizer and analyzer rotations relative to the dichroic mirror were tested at 5-degree increments to determine the optimal orientation of all three elements that affect

polarization contrast (Fig. 24). It was found that alignment of the linearly polarized illumination to within 0.5 degrees of either orthogonal or parallel with the reflection plane of the dichroic was required to generate an adequate extinction ratio image hemozoin in samples.

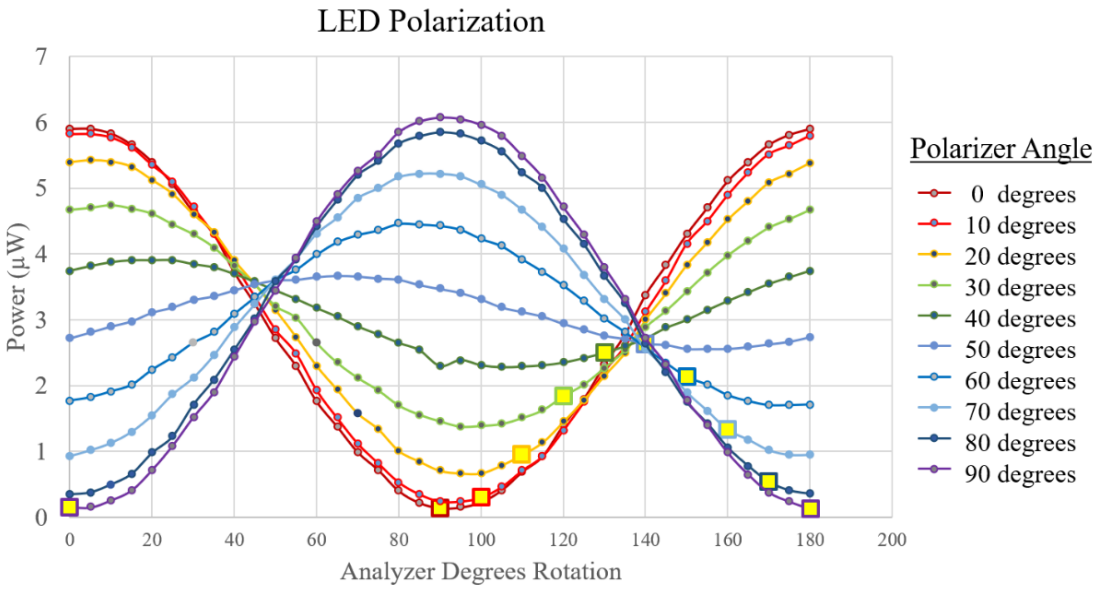

Figure 24: Transmission of broadband LED light for varying combinations of polarizer and analyzer angular alignment. Yellow square markers indicate alignments at which polarizer and analyzer axes were orthogonally aligned.

Electronic and Optomechanical Components

A Raspberry Pi 3 was selected as the data collection, storage, and transmission module for the microscope due to its low cost, ease in prototyping, and simple integration with commercially available camera sensors. A complementary 8 MP Picam v.2 with Sony IMX219PQ sensor (3.674 x 2.760mm, 1.12 µm pitch) with lens removed was selected for its small pixel size, resolution, low cost, and highly controllable acquisition parameters.

To control sample translation and focusing, four mini stepper motors (28BYJ-48, Kiatronics, NZ) with 4096 step increments/rotation receive driving currents from a custom motor driver circuit. Two motors control focal depth, one controls X-axis sample translation, and one controls Y-axis translation. Power is provided to the microscope by two lithium-ion battery packs that can be recharged by plugging the microscope into a power outlet. The optomechanical mounts for the prototype microscope were either 3-D printed or incorporated as off-the-shelf parts. All components of the multimodal imaging system are self-contained in a durable plastic enclosure measuring 11” x 6” x 5”, with auxiliary components such as the Raspberry Pi, motor control board, and rechargeable battery packs fully integrated into the unit (Fig. 25). The unit is capable of operating without any external power supply from on-board battery packs or may be plugged into an external 5-volt power supply for operation and battery recharge.

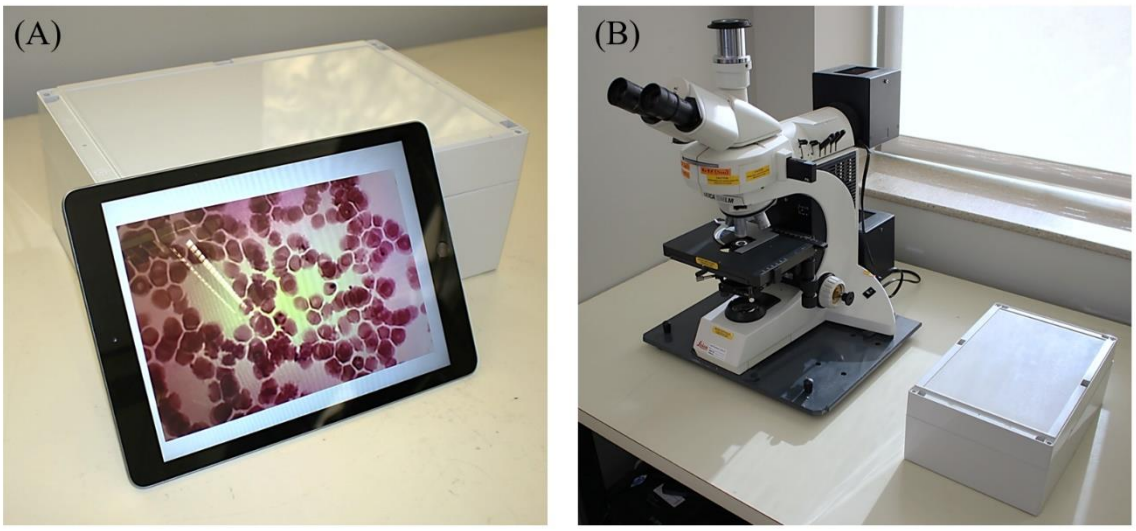

Figure 25: Image of the final portable system: (A) in use with an iPad, and (B) next to a comparable benchtop microscope.

Operational Procedure

To operate the microscope, a thin sample fixed to a standard 25×75mm microscope slide is inserted into the stage via access port opened from the side of the case. Wet samples with coverslips may also be used, although it is recommended to affix the coverslip to the slide to prevent slippage while in the stage. The microscope is powered on, and any portable device with web-interface can be connected to the microscope via a device generated Wi-Fi network. After connection, an SSH-portal interface can be used to access controls for sample translation, focal control, and imaging mode. A graphical representation of microscope operational procedures is shown in Fig. 26. Adjustments to the sample position or focus can be made if necessary, or an alternative imaging modality can be selected without altering the sample position. A new field of view may be found by using the interface to move to any immediately adjacent field-of-view using pre-programmed commands. After pictures are captured, they can be automatically uploaded to any database structure desired, to onboard memory, or directly to the user's personal device. To demonstrate the capability of the multimodal microscope to interface with personal electronic devices, images were captured using a Windows-based laptop PC, an Android-based smartphone, and an Apple iPad (Figure 2). On all platforms, the command interface was able to successfully control microscope function and collect multimodal data.

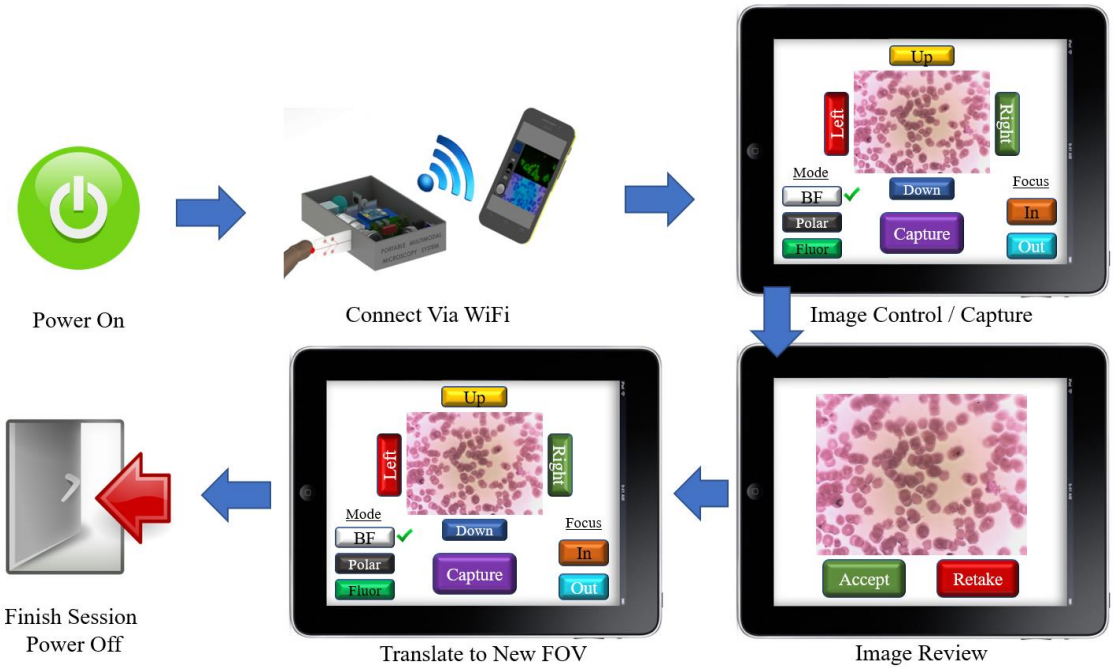

Figure 26: Operational procedure for portable microscope. After device is powered on, it can be connected to any portable WiFi enabled device. Once connected, an SSH client can be used to control microscope functions including illumination, sample translation, and camera control.

Experimental Results

Performance Characterization

To assess the multimodal functionality of the portable system, a control phantom was created by fluorescently staining lanuginose fibers from the underside of a sericeous tree leaf using SYBR Green-1 nucleic acid stain (Sigma, USA) for twenty minutes, then embedding the fibers in a thin film of degassed polydimethylsiloxane (PDMS, Sylgard 184, USA) on the surface of a microscope slide. A Zeiss AxioVert-A1 fluorescence microscope with high-power broadband LED source and FITC filter cube was used as the

fluorescence control, and a Leica DMLM compound microscope was used for both brightfield and cross-polarized controls. The embedded fibers express absorption in white light, birefringence under cross-polarization, and strong fluorescence at the excitation and emission wavelengths of the portable system. To demonstrate the ability of the microscope to be used in diagnostic applications, images were captured of blood smears of *in vitro* cultured *P. falciparum* which were stained with either SYBR Green-1 dye or a dual Giemsa/fluorophore technique described by Guy et al. and as described in Chapter 2 [57]. The two staining methods were compared as possible sample preparation options to ascertain which would provide the optimal balance of biomarker contrast across all three contrast modes, which has not been previously addressed in the literature.

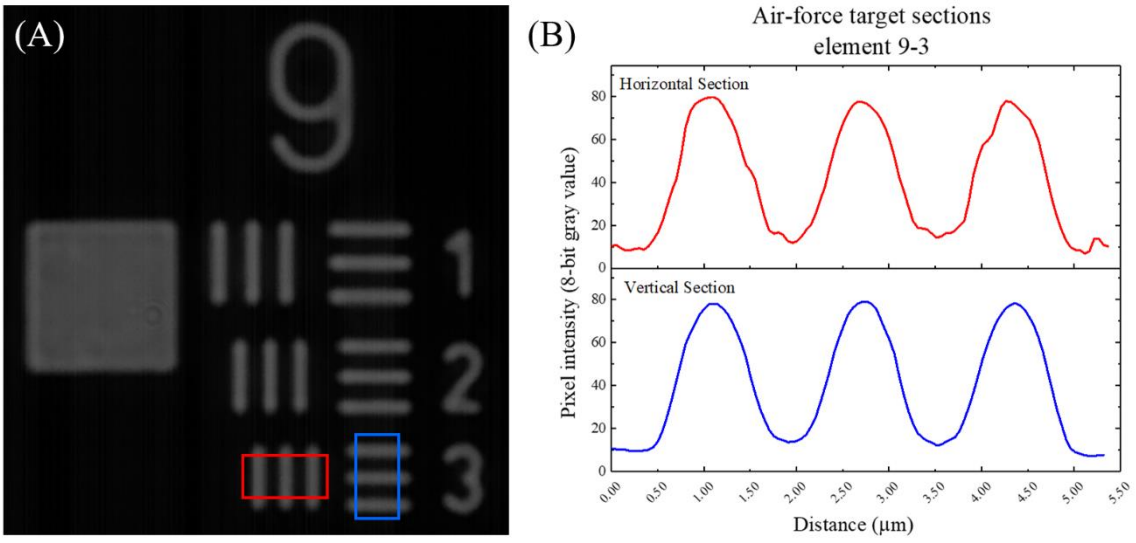

Figure 27: Resolution capability of the system as shown by imaged 1951 US Air Force Target. Line contrasts were averaged over the vertical and horizontal elements using boxed regions as shown using ImageJ software.

To assess system resolution capabilities, a negative high-resolution 1951 Air Force Target (transmissive line elements) was first used to test the resolving capabilities and magnification of the system. As can be seen in Fig. 27, element 9-3 (775nm line width) of the target is fully resolved using full-width-half-max criteria, easily satisfying both Rayleigh's and Sparrow's criteria for these features. Using known line widths and camera pixel pitch, images of the Air Force Target were used to experimentally calculate the net optical system magnification to be 27.8x. Images of the multimodal control phantom used to assess multimodal function are shown in Fig. 28, with the same field-of-view imaged both on the portable microscope and gold-standard benchtop systems.

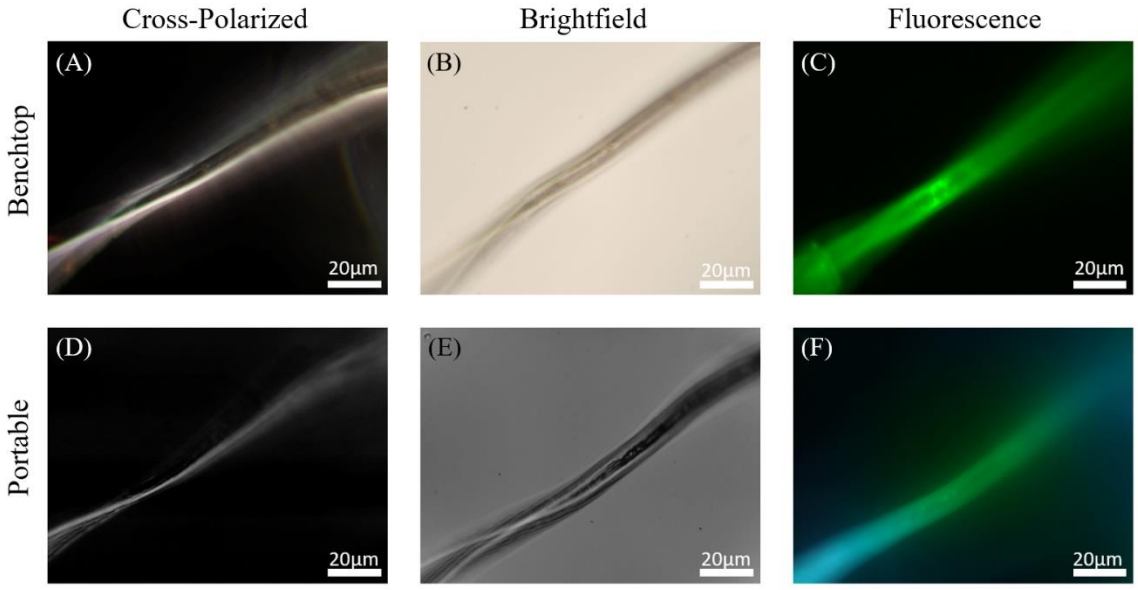

Figure 28: Images of a multimodal phantom collected on (top) individual benchtop instruments and (bottom) the portable microscopy system. The same feature is imaged in each image.

Multimodal P. falciparum *Imaging*

Thin films of blood cultured with *Plasmodium falciparum* were stained using either dual-staining or SYBR Green-1 methods as previously referenced, and images of these smears collected using the portable microscope were analyzed to assess signal strengths for each preparation protocol across each mode. Fig. 29 shows the average pixel intensity of various parasitic morphological features from grayscale images of this comparative study. Sample variance was defined as the standard deviation of the population of signal values surveyed. Brightfield images clearly show cell membranes and intracellular malaria pigment using either staining technique. Dual-stained images express a slightly darker background than those stained with SYBR Green-1 alone, however no significant difference was found for the absorption of light in trophozoites between the two staining methods (Fig. 29a). Fluorescence images reveal no significant difference in background intensity between the two staining techniques, although samples stained only with SYBR Green-1 showed significantly higher signal in trophozoites and schizonts, which is desirable for signal collection efficiency with low-cost photodetector arrays (Fig. 29b).

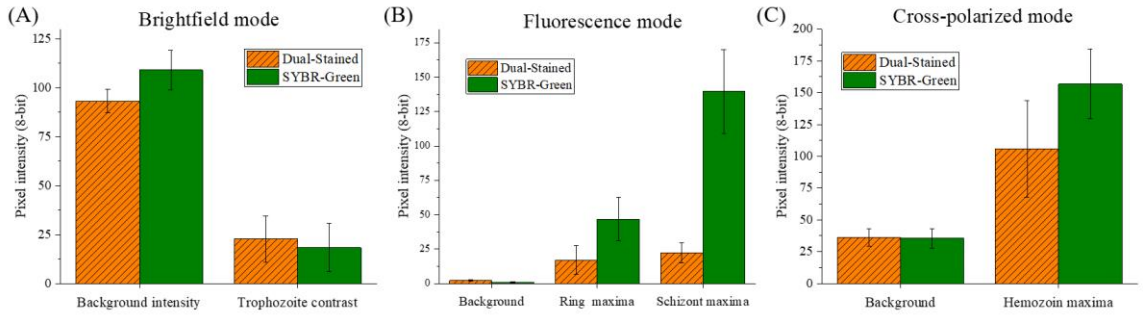

Figure 29: Metrics from sample preparation tests to optimize multimodal information available from *P. falciparum* cultured blood smears in (A) brightfield, (B) fluorescence, and (C) cross-polarized images.

In cross-polarized images, the signal strength from light depolarization in birefringent hemozoin crystals was found to be higher on average for SYBR stained samples than for those from dual-stained samples (Fig. 29c). Lower average cross-polarized signals in dual-stained samples were not expected, although the occurrence of these phenomena may be explained by the fact that Giemsa stain, which is part of the dual-staining technique, frequently precipitates salt crystals from its ionic components, which would add to the total number of depolarization events detected in the dual-stained sample and lower the average signal intensity if said precipitate crystals express weaker retardation than hemozoin. This effect, in combination with higher fluorescence signal intensities, imply that use of AO, SYBR Green 1, or other comparable fluorophores appears to be a logical choice for maximizing the amount of useful information that can be gathered from the portable multimodal microscopy system, although the specific preparation techniques must necessarily vary depending on the specific sample and test to be performed [164].

Thin smears of *P. falciparum* stained with SYBR Green-1 were imaged using the portable microscope and a benchtop Nikon Eclipse inverted microscope as a gold-standard control. Images from all three modalities of the portable system were successfully collected in succession and wirelessly transmitted to a personal electronic device for analysis. Results of multimodal imaging shown in Fig. 30 show that the portable instrument is capable of producing images of comparable image quality to benchtop instruments for each contrast modality. Diagnostically relevant morphological features were able to be observed in images from all three modes on both systems. All images were converted to grayscale during analysis, which was done primarily for aesthetic purposes, as it minimizes confusion resulting from chromatic shifts that appear when blue-channel data is removed from the brightfield color images, and fluorescence and cross-polarized images could then be false colored to heighten contrast in the displayed images.

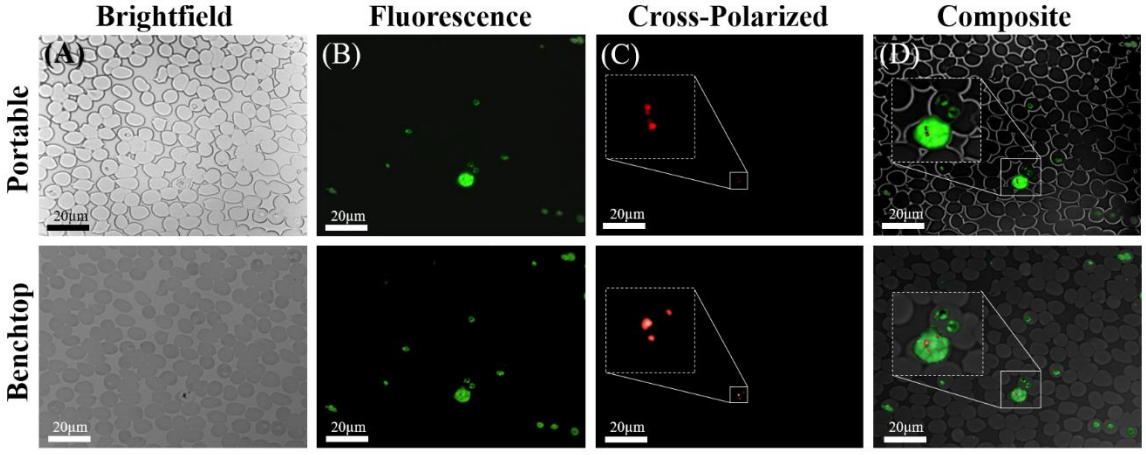

Figure 30: Multimodal images of various *Plasmodium* morphological forms from a single field of view: (A) brightfield images, (B) fluorescence images, (C) cross-polarized images, and (D) composite images of all three modes. Images have been contrast and gamma-level enhanced to improve clarity.

Portable brightfield images clearly show cell boundaries and intracellular parasites, although they do not display the same level of contrast between the intracellular space and background as is seen on benchtop images. In fluorescent images, the portable system can clearly resolve dual chromatin dots in ring-stage trophozoites, which are characteristic of *P. falciparum* infections. In cross-polarized mode, the portable system reveals the presence of hemozoin within a schizont, however it was unable to detect as many crystals as the benchtop microscope, indicating that the portable system suffers from a loss of contrast in this mode. In general, it was found that the system is able to resolve intra-erythrocytic parasites in all three imaging modalities, though with decreased contrast ratios when compared to benchtop systems using similar magnification. The portable multimodal images show various small parasitic features such as intracellular vacuoles, chromatin dots, ring stage and mature trophozoites, schizonts, and large hemozoin crystals.

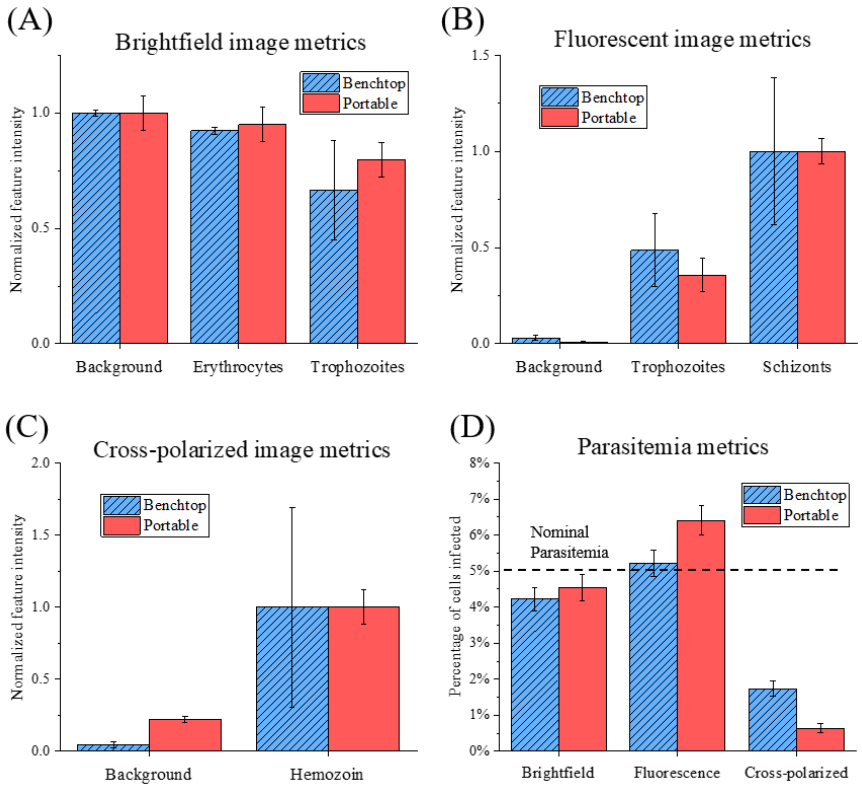

Figure 31: Comparative metrics for common malaria diagnostic biomarkers for (A) brightfield, (B) fluorescence, and (C) cross-polarized images, with (D) measurements of quantitative parasitemia shown for each mode.

From images collected on both the portable and gold-standard systems, image quality metrics and parasitic counts were collected to quantify the performance of the portable system. Fig. 31 presents bar graphs showing the mean intensity of various morphological features in images of each modality, with data normalized to the mean of the feature with highest intensity in each to compensate for differences in exposure intensities and times between the portable and benchtop systems. Between 3,000-3,500 cells were surveyed using each system. For parasitemia analysis, the infected proportion of cells was treated as a Bernoulli distribution, with binary determination of either

"infected" or "uninfected" made for each cell and variance expressed as the binomial proportion confidence interval. Full cell and parasite counts are displayed in Table 8, with "BF" indicating brightfield images, "FL" indicating fluorescence images, "Pol" indicating cross-polarized images, and percentage of the total number of cells given in parentheses.

Table 8: Parasitic features measured per FOV using each imaging modality.

FOV	Cell Count	Infected Cells, BF	Infected Cells, FL	Extra-cellular, FL	Infected Cells, Pol	Extra-cellular, Pol
1	44	5	4	3	2	2
2	37	4	2	0	1	0
3	33	3	4	0	0	0
4	30	1	1	0	0	0
5	32	4	3	0	2	0
6	31	3	6	1	1	0
7	28	4	4	2	0	0
8	30	2	2	0	0	0
9	20	2	2	1	0	0
10	26	4	5	0	1	2
11	23	2	2	0	0	1
Total	**334**	**34 (10%)**	**35 (10%)**	**7 (+2%)**	**7(+2%)**	**5 (+1%)**

Both systems present general agreement of feature signal contrast across all three modes, and measured parasitemia generally agreed with the nominal value of 5% of cells containing parasites. In brightfield images normalized to the background intensity, the portable system displays similar values but higher variance than the benchtop control for background and intracellular regions, which is expected given the lower quality of camera and optical components utilized. However, this trend is reversed when trophozoites are

examined, with the benchtop images displaying significantly higher variance of contrast compared to the portable system. This trend will be repeated across images from all three modes, with the portable system displaying higher signal variance for homogenous image regions such as the background or intracellular spaces, while benchtop images reveal higher signal variance for heterogeneous features. It is believed that this occurs because the benchtop system provides greater modulation of the high spatial frequencies found in fine, heterogeneous features, allowing the full range of feature intensities to be captured.

In contrast, while the optical system of the portable microscope can resolve such small features, it does not modulate the high spatial frequencies as effectively, leading to a loss in the dynamic range of signals. Images of trophozoites and schizonts in fluorescence images display this pattern as well. It must be noted, however, that fluorescence parasitemia data show that the portable system may be registering false positives in approximately 1.5% of cells, meaning that artifact registration may skew the feature intensity averages presented in Fig. 30b. Hemozoin signals from benchtop cross-polarized images likewise show significantly higher variance, with the cause attributed also to the higher number of small crystals that are able to be seen above the image noise floor, which is supported by analysis of the number of cells observed to contain the biomarkers in Figure 30d.

Interpretation of Results

The portable microscope is able to collect images in each modality with feature resolution below 775nm, which is sufficient to detect biomarkers for many cellular

samples. Indeed, examination of composite images collected from *P. falciparum* samples clearly show morphological features necessary to detect infections, quantify parasitemia, and distinguish mature parasites containing hemozoin, all of which are diagnostically important metrics currently not available from a single standard point-of-care device. Morphological feature recognition was performed by authors with several years of experience examining malaria smears in a research laboratory environment. This imparts subjective bias into the process of recognizing and cataloging morphological features in images, and further analysis by either independent trained experts in malaria hematology or by automated feature recognition software is necessary to improve the level of absolute confidence in the ability of the microscope to resolve parasitic morphology.

Limitations of system optics must be acknowledged, including the loss of some chromatic information in brightfield images due to inclusion of the dichroic mirror, reduced contrast in high spatial frequency information, increased exposure times necessary for fluorescence images due to use of a non-cooled, color camera sensor, and reduced extinction ratios in cross-polarized mode when compared to a gold standard benchtop instrument. Additionally, the presence of apparent false positives in fluorescence images is yet uncharacterized and must be studied further, after which it is hoped that image processing techniques may be able to separate artifacts from the true positives in datasets. Despite these limitations, the system represents an advancement in the quality and flexibility of microscopy systems designed for use at the point of care and may certainly have applications beyond those described in this work.

Imaging of Microfluidically Generated Smears

Materials and Methods

After the microscope's ability to image samples on dried smears was assessed, a separate investigation was conducted into the system's ability to resolve features inside microfluidic cartridges. Cartridge modifications were made to promote durability and cost savings as described in Chapter 2, and their optical properties were measured using the tri-modal microscope here. In order to complete the imaging investigation, however, a 20x Plan objective was substituted in the system so that a longer focal length could pass through the microfluidic cartridge substrates. Polycarbonate with a thickness of 0.254mm was compared with 0.17mm thick cover glass and a 1mm thick microscope slide by placing each material on top of a 1951 U.S. Air Force Target (USAFT) and then imaging elements 9.1, 9.2, and 9.3 which have a 0.98μm, 0.87μm, and 0.78μm linewidth respectively. Each image was taken on both a Nikon benchtop microscope along with the portable system, and collected images were analyzed by taking 10 lines of intensities across each of the investigated features to determine if the material hindered the system's capability to resolve each of the features (Fig. 32). Each group of intensities was analyzed by computing the full width half max (FWHM) of each line in each element.

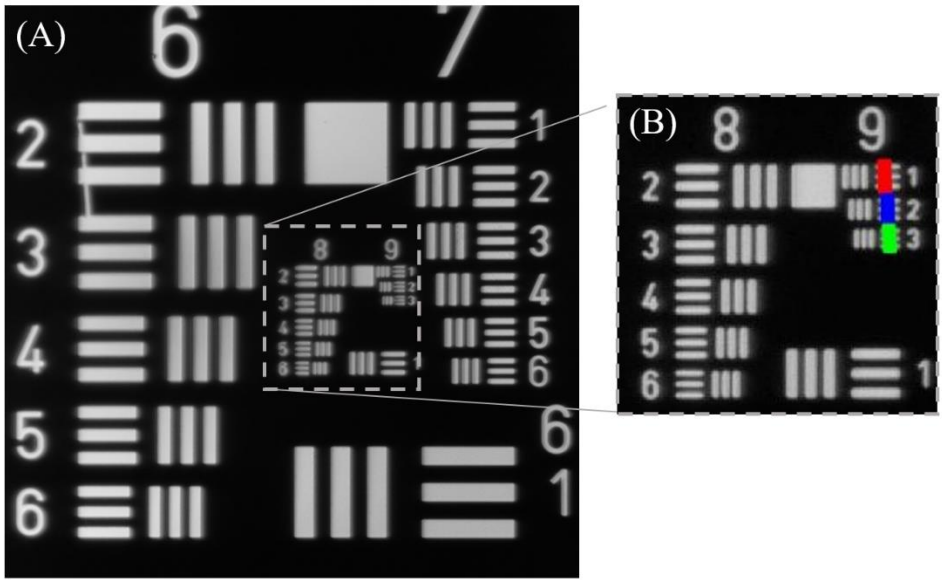

Figure 32: (A) Image of the air force target taken on the benchtop microscope. (B) Elements 9.1 (red), 9.2 (blue), and 9.3 (green) with the determined lines of intensities marked in their respective color.

A culture of *P. falciparum* was grown and combined with whole blood which was used to create a blood smear on both a piece of cover glass and polycarbonate plastic[3]. Once the smeared dried, images of RBCs and malaria parasites were taken on the benchtop and portable systems. The images were acquired by viewing through the material as if it were the substrate for a PDMS microchannel. From the images, individual RBCs and malaria parasites were identified and intensity values of each of the features were extracted to determine whether the system could resolve the features despite a layer of material to image through. Intensity lines were taken radially around the RBCs with and without malaria parasites at increments of 10° for 170° and averaged together (Fig. 33). The averaged intensities were then used to determine the features of the RBC along with the

features indicative of the malaria parasites by measuring the FWHM of the elements within the cross-sectional profile.

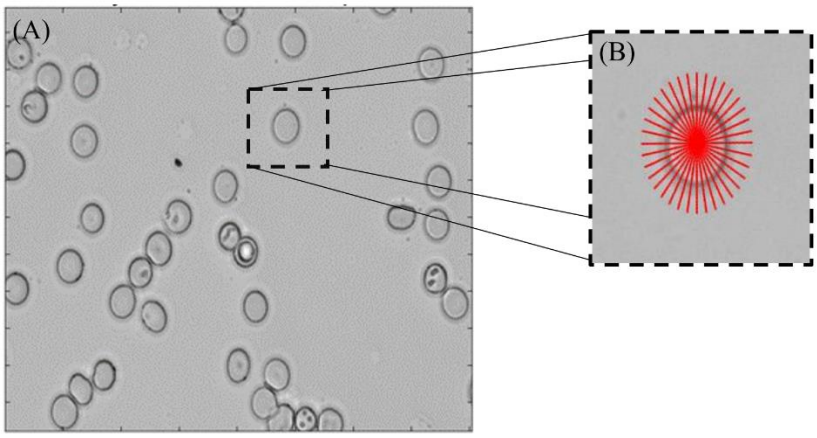

Figure 33: (A) Image of blood smear on cover glass taken on the benchtop system. (B) One RBC with radial intensity lines (red) drawn through it.

One microliter of the malaria infused blood was then inserted into the inlet of each a polycarbonate-PDMS channel and cover glass-PDMS channel. Each sample was allowed to flow to the end of the channel, and once all movement ceased, images of the RBCs and malaria parasites were captured on both the portable and benchtop systems.

Results

With red blood cells being about 7 microns in diameter and malaria parasites ranging from 1 to 20 microns in diameter, it is crucial to be able to resolve the smallest three elements on the USAFT[6]. Determining whether the FWHM of each of the intensity profile seen in Fig. 34 could be resolved showed whether the three smallest elements could

be resolved when imaging the USAFT through cover glass, PC, and microscope glass. The benchtop microscope could resolve all elements when imaging the USAFT through all materials. When placing glass (1mm thick) on top of the USAFT, the portable microscope couldn't resolve any of the three elements, proving a thinner material is necessary for the substrate in the microfluidic cartridge. When imaging the USAFT bare, with cover glass, and polycarbonate plastic on top of it, element 9.2 (0.87 µm linewidth) was the smallest element that could be resolved on the portable system. This confirms that the polycarbonate substrate is comparable with cover glass when imaging through it, making it a viable alternative to cover glass.

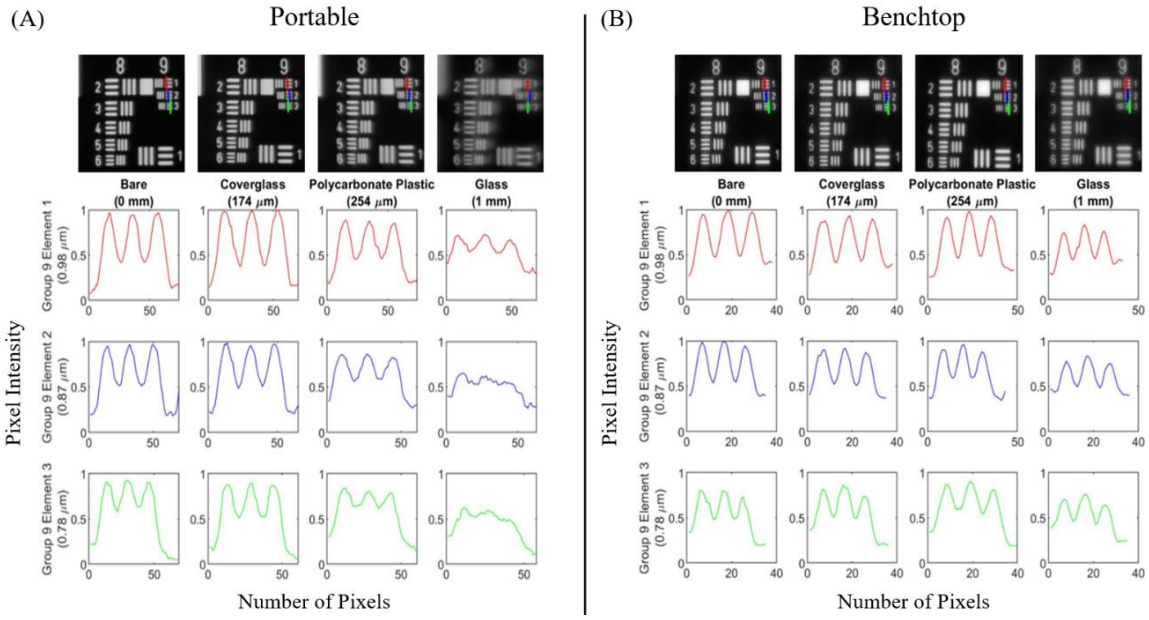

Figure 34: Intensity profiles of group nine elements on the 1951 USAFT when imaging through various substrate materials. (A) Images from portable system. (B) Images from benchtop system.

The first set of images to be analyzed were from thin smears conventionally made on a glass slide, but through varying types of layered substrate materials. Extracting intensity profiles of isolated RBCs helped determine whether distinct features of the RBC, such as the cell wall, could be resolved along with the whole RBC itself. This also provides a control when viewing cells with malaria parasites within them. Seen in Figs. 35a 35b, all images show the cell wall along with the whole RBC being resolved through both materials on both systems, using the FWHM measurement. Figure 35c shows a distinct intensity trough between two other smaller troughs which represents the malaria parasite populating the cell. Figure 35d shows a high intensity peak indicative of the malaria parasite within the cell compared to the intensity troughs of the cell walls. From these results, the parasite can be clearly resolved and distinguished from the RBC when comparing the malaria parasite to the background intensity. The similarities in profiles across the imaging systems ensures the portable microscope is comparable to the benchtop system when analyzing the resolution capabilities. Since the RBC wall and malaria parasites could be resolved through both materials and on each system, it can be concluded that using PC can give similar results to cover glass within a thin smear.

RBCs and malaria parasites were then imaged through the cover glass or PC substrate of the microfluidic cartridge. When imaging in a cartridge, effects of PDMS on the illumination side of a sample in a transmission mode microscope are assumed to have a negligible impact on image quality changes induced by varying substrate materials on the imaging side of the sample. So long as the PDMS “behind” the sample maintains homogeneous optical clarity and thickness across the sample and is imaged in Köhler type

illumination, it is expected that the PDMS will allow for even filling of the numerical aperture of the objective by illumination light, providing maximal theoretical image quality. Figs. 36a and 36b show a single RBC where the cell walls could be fully resolved according to the FWHM criterion. However, in Fig. 36b there is noise in the profile when using the portable system and the cell walls couldn't be resolved. On the benchtop system, the cell walls along with the whole RBC could be resolved, showing that PC is comparable to cover glass when resolving RBCs. In Figs 36c and 36d the malaria parasite within each of the cells was resolved when viewing it through both materials and on both systems. Fig 36d has a larger trough to the left of the profile due to the malaria parasite in the left region of the RBC. The cell wall closest to the malaria parasite couldn't be resolved due to the resolution limits of both the systems, but the furthest portion of the wall could be resolved.

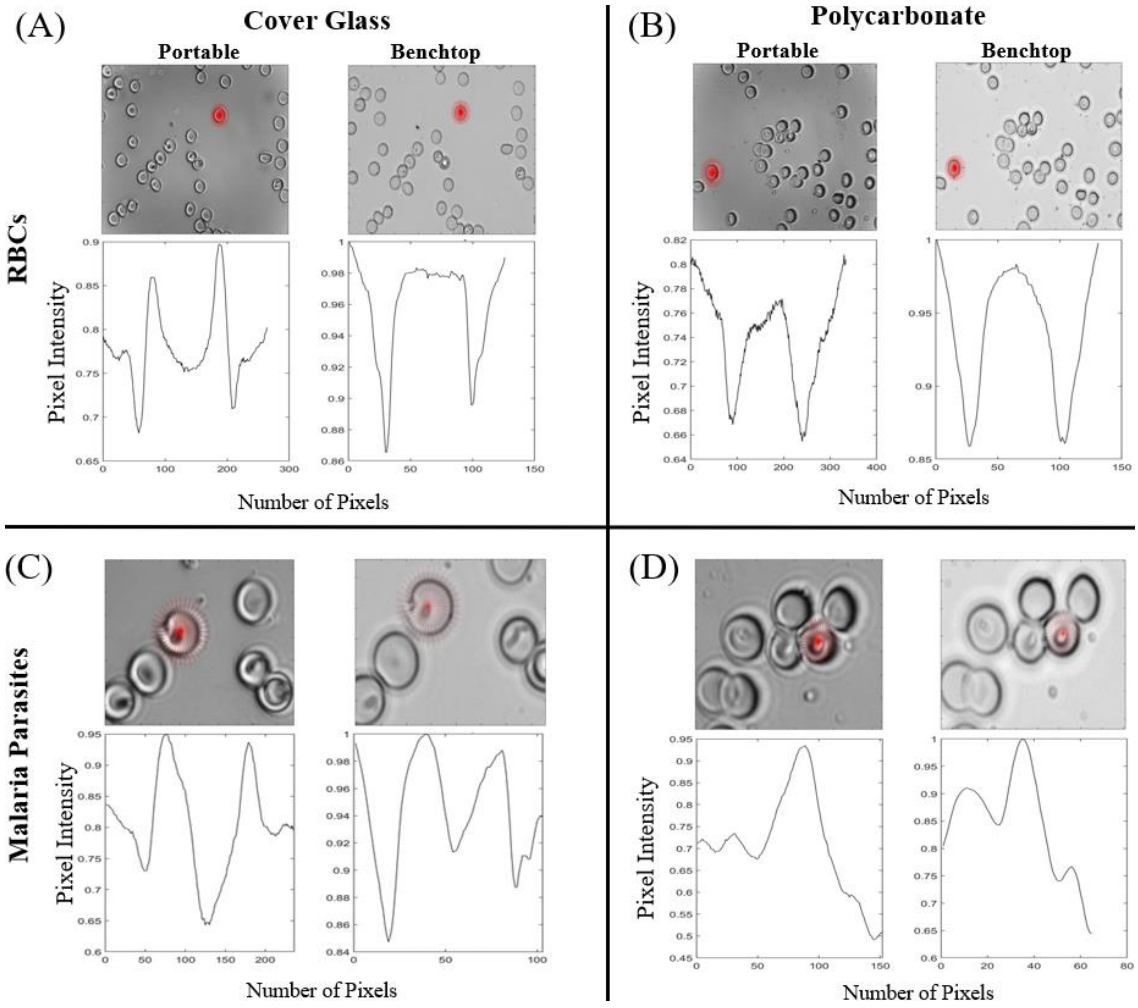

Figure 35: Thin smears on both cover glass and PC containing RBCs and malaria parasites imaged on the benchtop and portable systems with their respective profiles. (A) RBC through cover glass. (B) RBC though PC. (C) Malaria parasite within RBC through cover glass. (D) Malaria parasite within RBC through PC.

When comparing the images acquired through cover glass from the thin smear and the microchannel, the analyzed profiles have the same characteristics showing the cell wall and the malaria parasite, and each of these features can be resolved. This confirms the effects of the PDMS on the image acquisition can be considered negligible. The benchtop system was able to resolve features of the RBC and malaria parasites through

PC and cover glass in the same manner making the materials comparable to one another. Even though the portable system wasn't able to resolve the cell wall of the RBC through PC, it was able to resolve the malaria parasite. The profile taken from the benchtop image through PC shows another set of troughs between those of the cell wall the portable system couldn't resolve due to their intensities being similar to the cell wall. This shows the PC wasn't the issue, but instead the resolution capabilities of the whole system were responsible. Ultimately, when imaging using the portable system, the PC and cover glass substrates are effectively comparable to one another.

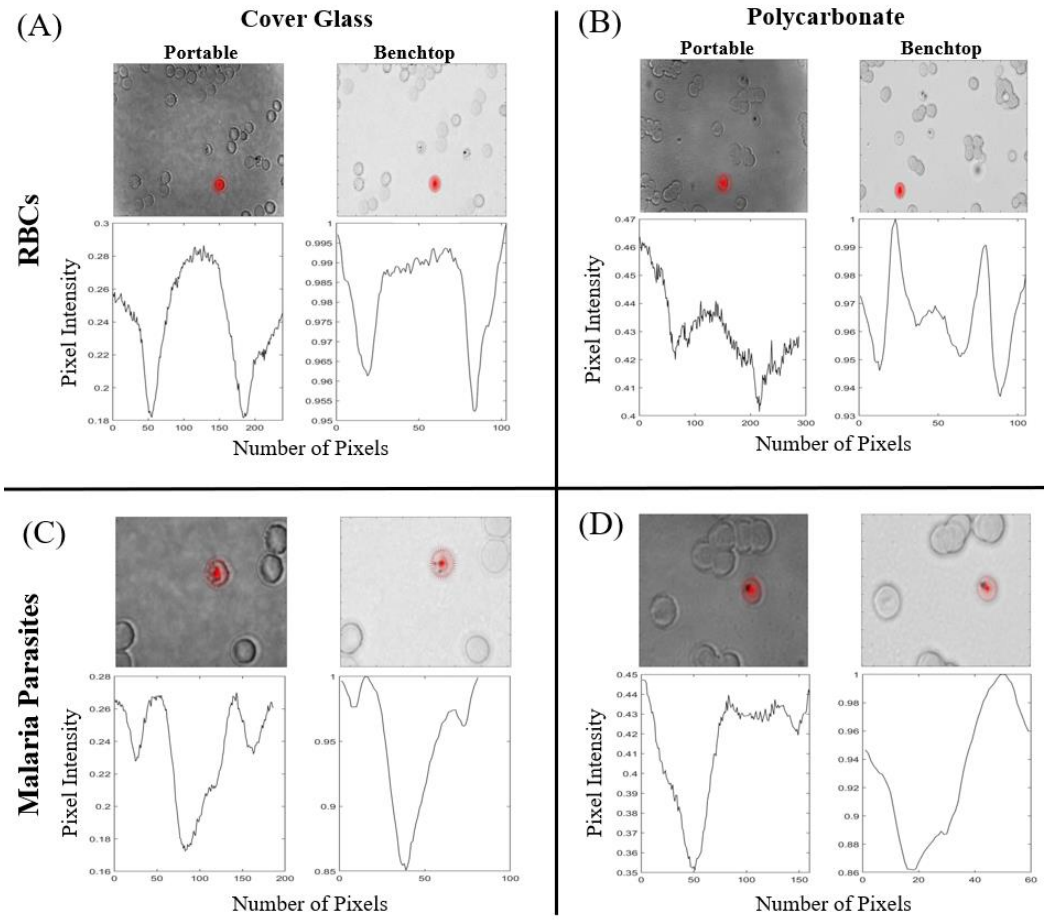

Figure 36: RBCs and malaria parasites within a microchannel with both cover glass and PC as the bonded substrate, using portable and benchtop systems. A) RBC through cover glass. (B) RBC though PC. (C) Malaria parasite within RBC through cover glass. (D) Malaria parasite within RBC through PC.

Conclusions

In conclusion, we have shown that a portable, multimodal microscope can successfully resolve features necessary for detecting *P. falciparum* parasites in brightfield, fluorescence, and cross polarized modalities. This system is constructed in a compact form factor using standard optical components and inexpensive electronics. Preliminary results toward use for malaria diagnosis show that the same morphological features can be seen

on the portable system as on a benchtop microscope with similar magnification, indicating that further, more comprehensive investigation is merited to assess its sensitivity and specificity in a comprehensive diagnostic setting. To the authors' knowledge, this is the first published example of a portable, customizable, tri-modal microscope intended for diagnostic applications at the point-of-care.

An advantage of the system is its flexibility to be easily modified to match the specific needs of a variety of specific tests that may be required. For example, if images of a different magnification or fluorescence emission spectrum are desired, components such as the objective lens, emission filters, LED's, and dichroic mirror are easily accessible and can be interchanged to adapt the microscope to achieve the desired performance. This ability to customize the microscope underscores its potential utility as a platform for performing laboratory-grade microscopic imaging at the point-of-care for a variety of applications. The system as presented here is not without its usability limitations, as numerous changes would likely be made to translate the current prototype into a commercially viable unit that is low-cost and field ready. Use of off the shelf or 3-D printed optomechanical components should be replaced by inexpensive, appropriately toleranced injection-molded parts to improve repeatability and reduce costs. Additionally, the water, shock, and dust resistance and overall durability have not yet been fully tested for the prototype and would need to be considered before field use.

Additionally, it was shown that thin polycarbonate sheeting can be plasma bonded to PDMS channels and is useful as the substrate of a microfluidic cartridge in a comparable, but more durable, manner as cover glass. Both the benchtop and portable

systems were able to resolve the cell walls of individual red blood cells and malaria parasites through polycarbonate. The combination of a portable microscopy system and microfluidic cartridge utilizing plastic as the substrate creates a system that can be used for a variety of applications including the detection of malaria.

CHAPTER V

QUANTITATIVE PARASITEMIA MEASUREMENT USING A LOW-COST, BI-MODAL PORTABLE MICROSCOPY SYSTEM*

Introduction

To more specifically target the need for a quantitative parasitemia measurement tool in remote settings, a second-generation portable microscopy system was researched and developed to be optimized for both quantitative parasitemia measurement and cost efficiency. Such a device can better inform diagnostic and monitoring efforts for malaria patients in remote locations by providing a tool that is able to assess the current infection severity for a patient at any given point in time. The system employs a multimodal approach that uses brightfield imaging to detect RBC margins and count the total number of cells in a field-of-view and fluorescent imaging to detect the presence of parasites with high contrast. The microscope is intended for use as an adjunct to RDT-based primary screening techniques as opposed to an entirely replacement technology. Theoretically, disease confirmation would be obtained using RDT's, then the portable microscopy system would be subsequently used to measure parasitemia for diagnostic and monitoring purposes.

---

* Portions of this chapter are reprinted from: Gordon, P., Ghorayshi, M., Venancio, V. P., Mertens-Talcott, S. U., & Coté, G. (2019, March). Diagnostic utility of a portable multimodal microscope for malaria treatment at the point-of-care. In Optics and Biophotonics in Low-Resource Settings V (Vol. 10869, p. 108690X). International Society for Optics and Gordon, P., Dogbevi, K. S., Kiefer, K., Mertens-Talcott, S. U., & Coté, G. (2020, February). Low cost microscope for malarial parasitemia quantification in microfluidically generated blood smears. In Optics and Biophotonics in Low-Resource Settings VI (Vol. 11230, p. 1123005). International Society for Optics and Photonics. With permission from SPIE.

Statistical Considerations for Parasitemia Measurement

In designing a device for parasitemia measurement, it is important to note that parasitemia can be measured in several slightly different manners, which can generate confusion and inaccuracy if not properly accounted for. The WHO Malaria Microscopy Guide recommends "reasonably and acceptably accurate" parasite counting method in which parasites are counted relative to the number of leukocytes in thick blood films [34]. The accuracy of the measured parasites per microliter using this method is hence limited by the accuracy of the assumption that patients have 8,000 leukocytes per microliter of blood. Values of parasitemia can also be defined by comparing the number of parasites to either red blood cells or directly to blood volume, which are limited by their dependency on the precision of the assumptions of red blood cells per microliter and the exact volume of blood sampled, respectively. To preserve clarity, this work will measure parasitemia by directly comparing the number of parasites to the number of red blood cells in a sample. This value can be expressed in two forms; either as the percent of parasites to RBC's (usually expressed as parasites per 100 RBC's, to match conventional percentage-based metrics), or as the extrapolated number of parasites per microliter of blood (again assuming 5,000,000 RBC's per microliter).

For purposes of this research, the extreme upper limit of expected parasitemia is set to be 500,000 parasites per microliter of blood, or 10% of cells infected. This is the threshold for the definition of hyperparasitemia according to the WHO Malaria diagnostic guidelines, however it represents an extreme example of infection, and symptoms in a patient with such a severe infection will likely leave no doubt as to the severity of the

infection [44]. From a survey of the literature, it can be found that a more common upper range of parasitemia measurements in patients presenting symptoms during *P. falciparum* cases in high-transmission regions could be reasonably expected to be between 100,000-200,000 parasites per microliter, or 2-4% of cells infected (Table 9).

Table 9: Literature survey results of *in-situ* parasitemia measurements in high-transmission region.

Region [reference]	Sampled Population	Demographic	Parasitemia Range (per µL)
Tanzania [165]	Random Sampling	Infants <1	2,600 – 3,507
Tanzania [166]	Random Sampling	Children <6	~500 – 50,000
Tanzania [167]	Random Sampling	Mixed Households	~100-10,000
Burkina Faso [168]	Unknown	Mixed	~50 – 1500
Papa New Guinea [169]	Presenting	Mixed	14,000 – 162,000
Ghana [170]	Random Sampling (asymptomatic)	Mixed	84 – 1,447
Burkina Faso [171]	Presenting	Mixed	1 – 100,000
Kenya [172]	Random Sampling	Mixed Children <14	200 – 10,000
Uganda [173]	Presenting	Mixed	1 – 200,000

In determining an appropriate lower bound of detection, it is impractical to use the true lower range of parasitemia in patients. This is because as a person could have sub-detectable parasitemia using conventional benchtop microscopy. Typical lower limits of microscopic detection from the literature range anywhere from 5 – 100 parasites per microliter, which is accomplished by examining thick blood smears. Yet, these limits of detection are also unfeasible to implement in a system that examines cartridge-based thin

smears as they use many more RBC's than are present in thin smears. It is most practical in this case to consider what lower bound of detection is implied by the diagnostic necessity when the microscope will be used as a supplement to RDT screening. With reference to Table 1, which contains information regarding the types of medications prescribed by the WHO, the primary diagnostic needs are to classify malaria as either complicated or uncomplicated, which species are infecting, whether the infection is resistant to medications, and which risk factors the patient presents. None of these criteria rely explicitly on parasitemia measurements, but it can be inferred that uncomplicated patients with over 1% of cells infected will be in later stages of the disease and more likely to progress rapidly to a complicated state.

After necessary upper and lower diagnostic measurement bounds have been approximated, attention can be turned to the needs implied by microscopy use for disease monitoring purposes. This is primarily driven by the hypothesis that the microscope could be used to screen for drug-resistant infections by measuring clearance rates post-treatment by collecting serial parasitemia data. Therefore, the need is for parasitemia differentiation within those bounds, and possibly below the diagnostically necessary minimum if possible. According to data published by Dondorp et al., it can be determined that drug-resistant strains of *Plasmodium* can be characterized by a decreased clearance rate after the administration of medication [30]. According to that study, nominal clearance rates from the bloodstream are approximately 10^{-2} / 24 hours, while the clearance rates of resistant population are halved, or near 10^{-2} / 48 hours. A graphical expression of these theoretical average clearance rates can be seen in Fig. 37, with sampling points taken at

two-hour intervals post-treatment. When considering the exponential decay of parasites in the bloodstream, it is easy to see that the specificity necessary for parasitemia differentiation is dependent on the current concentration in the blood, causing separability between sequential measurements to be easier when the concentration is high than when it is already low.

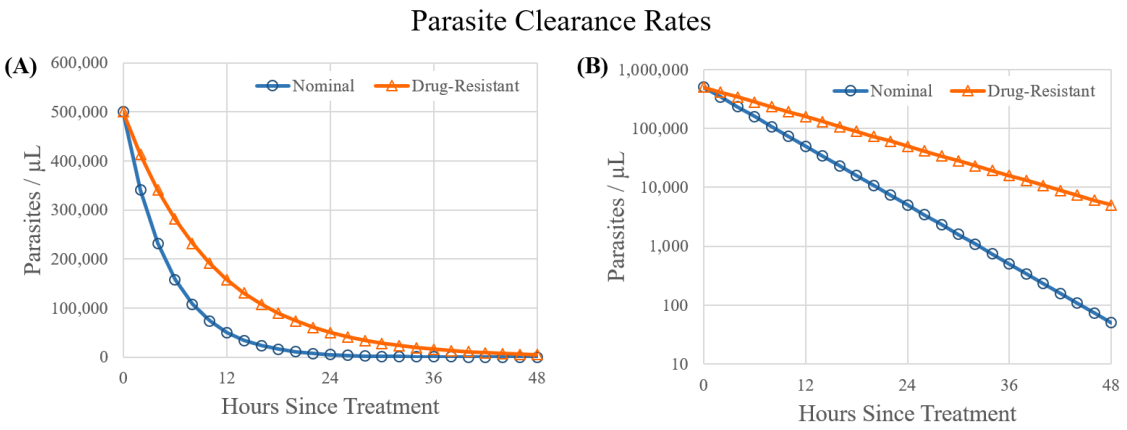

Figure 37: Theoretically modeled parasite clearance rates of nominal and drug-resistant infections post ACT administration in (A) linear space and (B) logarithmic space. Models based on experimental data by Dondorp et al. [30].

Given the differential clearance rates, if a patient presents with a given parasitemia, *p*, their resulting parasitemia after an amount of time, *t*, in hours for nominally resistant infections would be given by,

$$Resulting\ Parasitemia_{nominal} = p * 10^{-(t/12)}, \qquad \text{(Eq. 18)}$$

and the resulting parasitemia for a drug-resistant infection would be given by,

$$Resulting\ Parasitemia_{resistant} = p * 10^{-(t/24)}. \quad \text{(Eq. 19)}$$

Therefore, the necessary lower bound of detection imposed by use for hypothesized drug monitoring applications is any that allows the difference between nominal and resistant infections to be measured without significant overlap in uncertainty at the time of measurement. Because these considerations are dependent on the presenting parasitemia, which is unknown and varies widely depending on region and uncertainty in a resulting measurement, it is difficult to impose a strict necessary lower bound of desired parasitemia detection without further information. What can be said definitively, however, is that optimal sampling intervals would need to be assessed depending on the most commonly presenting parasitemia in patients in a given setting. It can also be determined that the larger the sample size of cells that are surveyed, the lower the uncertainty in measurements, and the greater the probability that low parasitemia measurements will be accurate. Attention must therefore be given to the number of cells that must be surveyed.

Determination of Necessary Sample Size

It is difficult to translate current WHO and CDC recommendations for lab-based microscopy sample sizes directly to the portable microscopy system [22, 34]. This is because these recommendations have been developed to improve the reliability of human performance, rather than being based strictly on rigorous statistical data. A summary of

sample sizes derived from WHO-recommended procedures for lab-based microscopy is provided in Table 10 (data adapted from WHO documentation [22]). A more rigorous treatment of generally applicable statistical considerations for various malaria diagnostic and eradication purposes can be found in the 1966 WHO publication by Swaroop et al. [174].

Table 10: Calculated sample size requirements for WHO lab-based microscopy. Adapted from [22].

Smear Type	Purpose	Parasitemia Range	Detection Limit (normal/expert)	Necessary RBC's	Necessary WBC's
Thick	Detection	All	100 / 5	1,000,000	1,750
Thick	Parasitemia Count	<4,000	-	312,500	500
Thick	Parasitemia Count	>4,000	-	125,000	200
Thin	Detection, Species, & Count	>4,000	500 / 200	320,000	512

If the determination of whether a specific red blood cell is infected is represented as a binomial event, the probability of whether red blood cells in a sample are infected with parasites can be assumed to follow a Bernoulli distribution. From this assumption, it is possible to construct a model to simulate the distribution of probable numbers of parasites found in various sample sizes at discreet time intervals during treatment. The results of one such model constructed in MATLAB utilizing the Clopper-Pearson interval

are displayed in Fig. 38. The shown example outputs from the model use 10,000 and 1,000 cell samples and nominal clearance rates to deomonstrate the distribution of probabalistic outcomes when a measurement from a sample containing the true parasitemia represented by the peak of the distribution is collected. The legend in the plot gives the total number of parasites expected to be found in a population of cells given by the sample size when the true parasitemia is at the concentration indicated by the peak of the corresponding bell curve. As can be seen toward the right side of each graph, when the true parasitemia is high, the possible distribution of sampling results remains narrow, and measurements taken at four hour intervals remain highly separable. Toward the left side of each plot, however, it can be shown that as the concentration of parasites decreases, the distribution of probable outcomes begin to significantly overlap for measurements taken at four hour increments. By comparing Fig. 38a to Fig. 38b, it is also apparent that increasing the number of sampled cells leads to increased differentiability between populations of probable parasitemia measurements. Although this model assumes perfect detection of parasites in blood smears, it gives a useful generalized framework from which to understand the interconnected impact of changes in parasitemia, sample size, and sampling intervals in gathering micrographic measurements for the monitoring of parasitic clearance rates.

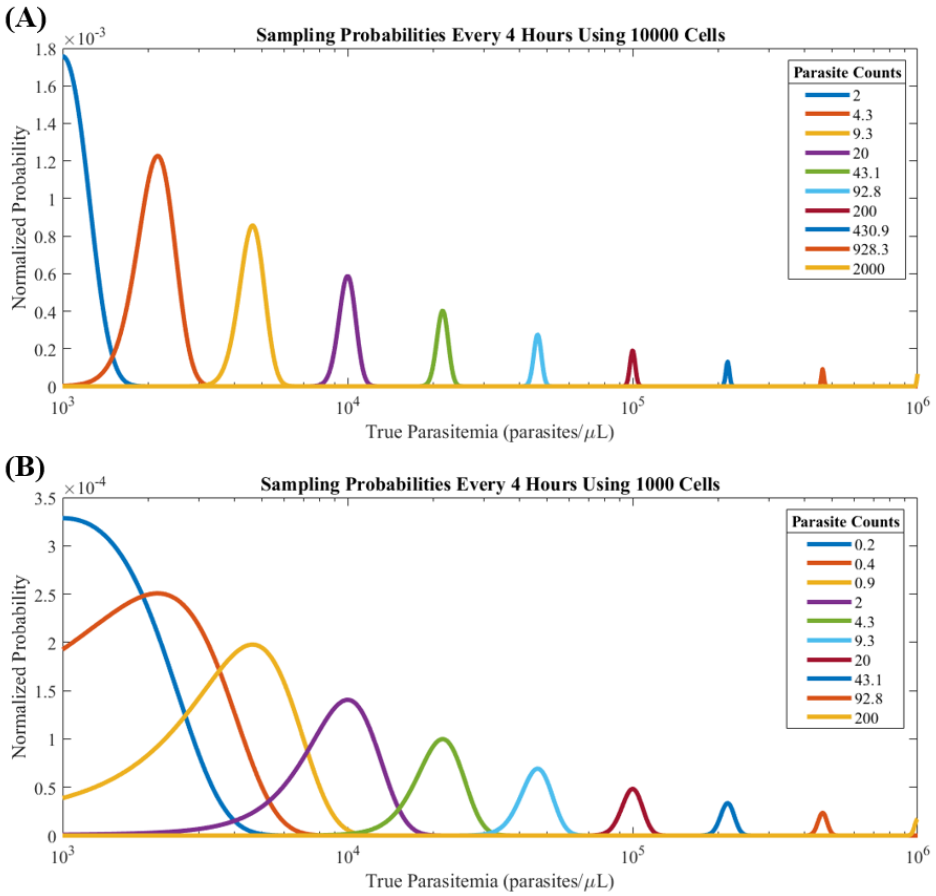

Figure 38: Modeled outcome of parasitemia sampling every four hours (successively from right to left) during post-treatment parasite clearance. Curves represent the distribution of probable sampling outcomes at their peak (mean) true parasitemia when (A) 10,000 cells and (B) 1,000 cells are sampled.

An alternative way to consider the impact that parasitemia and sample size have on the statistical accuracy of measurements is to consider the percent error of a given parasitemia measurement at the edge of its 95% confidence interval for any given sample size. This relationship, being a function of two independent variables, can be represented as a surface over parasitemia and sample size, with the percent error of the confidence interval increasing with both lower parasitemia and lower sample size. A contour plot of

this surface is shown in Fig. 39, representing sample size as the equivalent number of microscopic FOV assuming the average cellular smear density (670 RBC per FOV) that was found using the bimodal microscopy system. Being based on the deviation from the mean at the outer edges of the 95% confidence interval, these relative error calculations represent an approximated worst-case probable outcome, and it is generally expected that the relative error of measurements will be below those represented here.

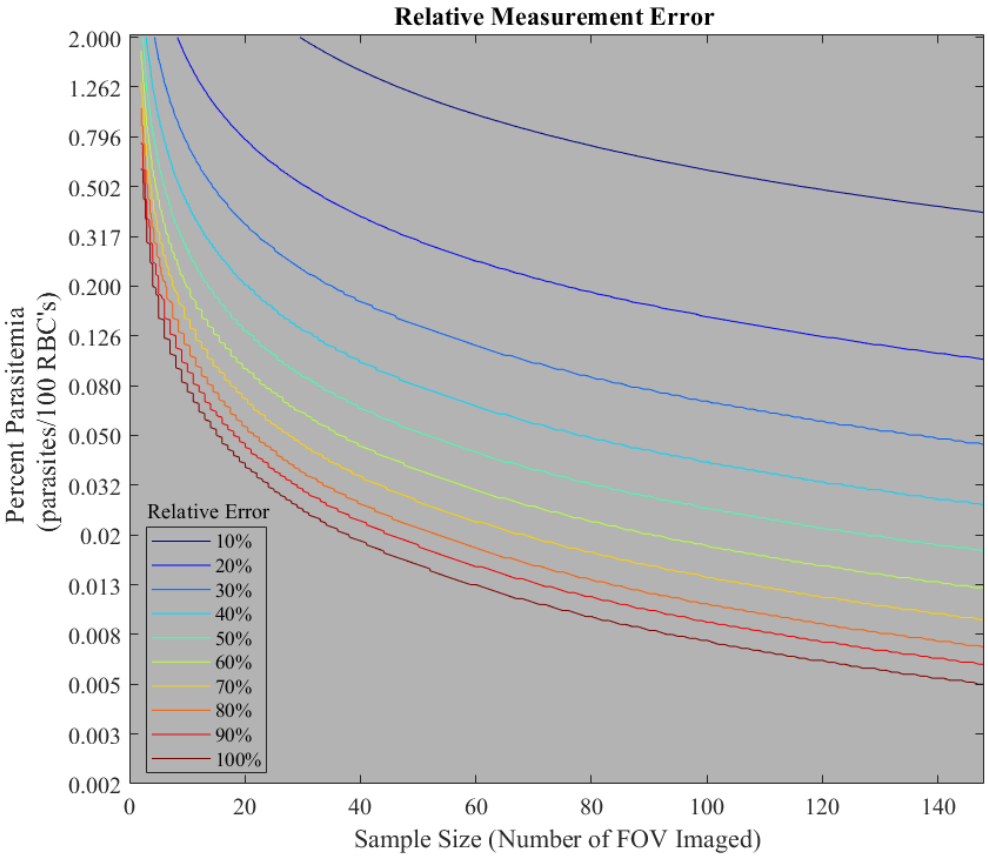

Figure 39: Contour plot of relative measurement error for varying parasitemia and sample sizes. Parasitemia is defined as the number of parasites per 100 RBC's, and the sample size is listed in number of fields of view examined assuming the average of 670 cells per field of view.

Microscope Configuration

A bi-modal brightfield and fluorescence design was chosen for the microscope, with brightfield imaging used to assess cellular size and boundaries, and fluorescence imaging used to detect intracellular parasites [62]. Bimodality is achieved by capturing two subsequent images for each field-of-view, with transmission-mode images providing cell counts and fluorescence-mode images providing biomarker localization data. A 523-nm monochromatic LED for transmission illumination (Osram, Germany; # LZ1-00G102-0000) is employed with center wavelength aligned to the fluorophore label (acridine orange) emission peak near 520nm, which minimizes the effect of chromatic aberrations, allowing for singlet lenses to be used in place of more expensive doublets and triplets designed to correct for chromatic aberrations. Fluorescence excitation was provided by a 485 nm LED (Cree, U.S; #XPEBBL-L1-0000-00301) chosen to align primary emission wavelength with the excitation peak of both Acridine Orange and SYBR Green-1 dyes used to label parasites in smears. The fluorescence filter set (Semrock, U.S; FITC-LP01-Clinical-000) contained a dichroic mirror with 500 nm cut on/off, 475/28 nm excitation bandpass filter, and emission long-pass filter with cutoff at 515 nm. A Jetson Nano ARM-based single-board computer (Nvidia, Santa Clara, CA) was chosen as the onboard data collection and processing system due to its low cost and ability to facilitate future implementations of automated image processing based on machine-learning algorithms. A 1.6 MP monochromatic Blackfly S camera with a Sony IMX273 sensor (FLIR Systems Inc, Wilsonville, OR) was chosen for its combination of price, sensor and pixel sizes, frame rate, SNR, compatibility, and well-defined programmatic interface.

Zemax ray trace models were used to design the system, choose off-the-shelf lenses, and verify performance prior to prototype construction. The system was designed to resolve the features necessary to detect *Plasmodium* inside red blood cells and magnify the image by approximately 16x to allow the full width of prototype microfluidic channels (250 μm) to be surveyed in a single image capture. Using the Rayleigh criterion, the diffraction limited resolution for an NA 0.40 objective lens at 520nm is 793nm, which is theoretically sufficient to resolve intracellular parasites on the order of one micron in diameter. The objective lens chosen based on Zemax modeling was a Geltech 0.40 numerical aperture (NA) glass aspheric singlet with 6.24mm focal length (LightPath Technologies, Orlando, FL; ##355110), and the chosen tube lens was a bi-convex spherical singlet with 100 mm focal length (Newport Corp., Irvine, CA; #KBX064). Glass aspheric lenses with NA 0.79 were used to collect and condense the light from the transmission LED source onto the object plane (Thorlabs, Newton, NJ; ##ACL25416U), and a singlet biconvex lens (Newport Corp, Irvine, CA; #KBX043) was used to collect epi-illumination light for fluorescence excitation.

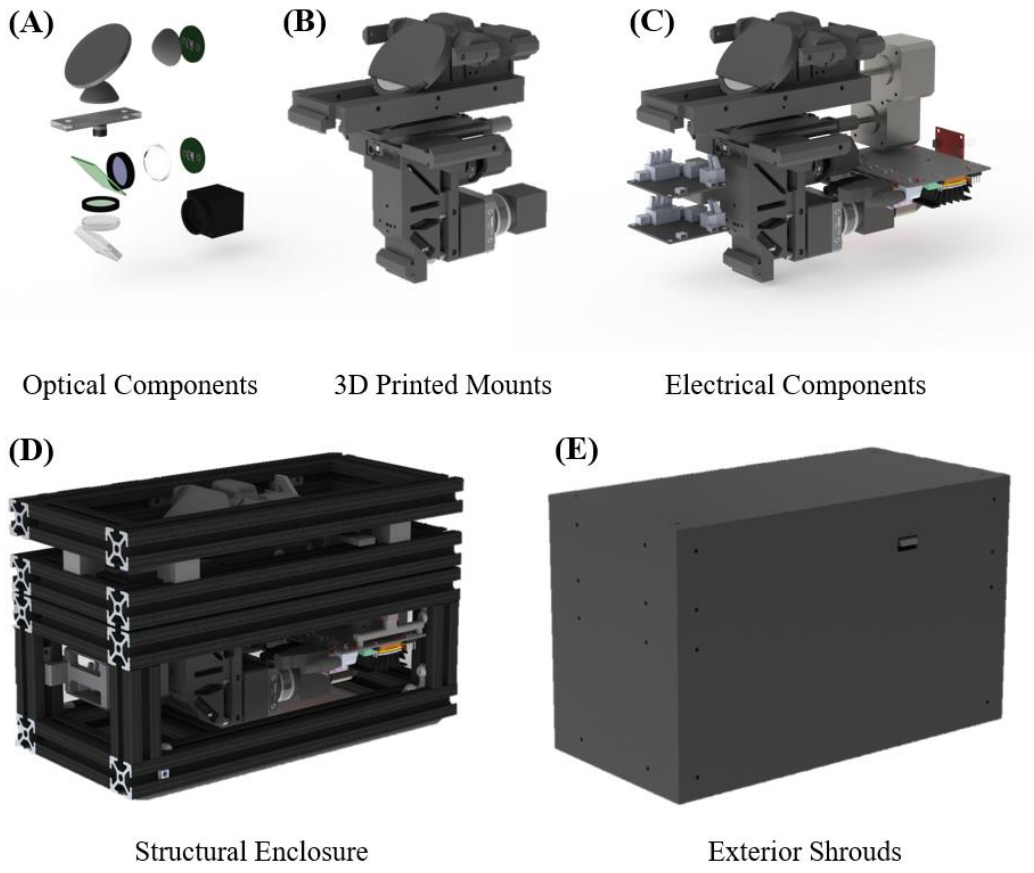

Figure 40: Model renderings of prototype microscope showing: (A) primary optical components, (B) 3-D printed optomechanical mounts, (C) electronic and control components, (D) structural enclosure, and (E) exterior shrouds.

The prototype microscope was assembled using 3-D printed (fused deposition modeling, PLA filament) custom optomechanical components and was housed inside a case constructed from 1” square aluminum rails and an ABS plastic enclosure, with exterior dimensions measuring approximately 12” x 8” x 5” (Fig. 40). The optical configuration was similar to that of a conventional fluorescent microscope with a 2” planar aluminum mirror (Thorlabs, Newton, NJ; #ME2-G01) used to fold the illumination

pathway and a 1” planar aluminum mirror (Thorlabs, Newton, NJ; #PFSQ10-03-G01) used to fold the imaging pathway (Fig.41). To check performance with potential cartridge-based smear preparation devices, images of a wet smear generated in a prototype fluidic cartridge were gathered. Following the check for cartridge compatibility, a fluorescently stained glass mounted thin-smear was imaged on both the prototype microscope and a benchtop system (Nikon Eclipse Ti2-U) using a similar commercial microscope objective (20x, 0.45 NA, Nikon #MRH48230) to verify fluorescence imaging functionality and establish the benchtop system as viable a gold-standard control.

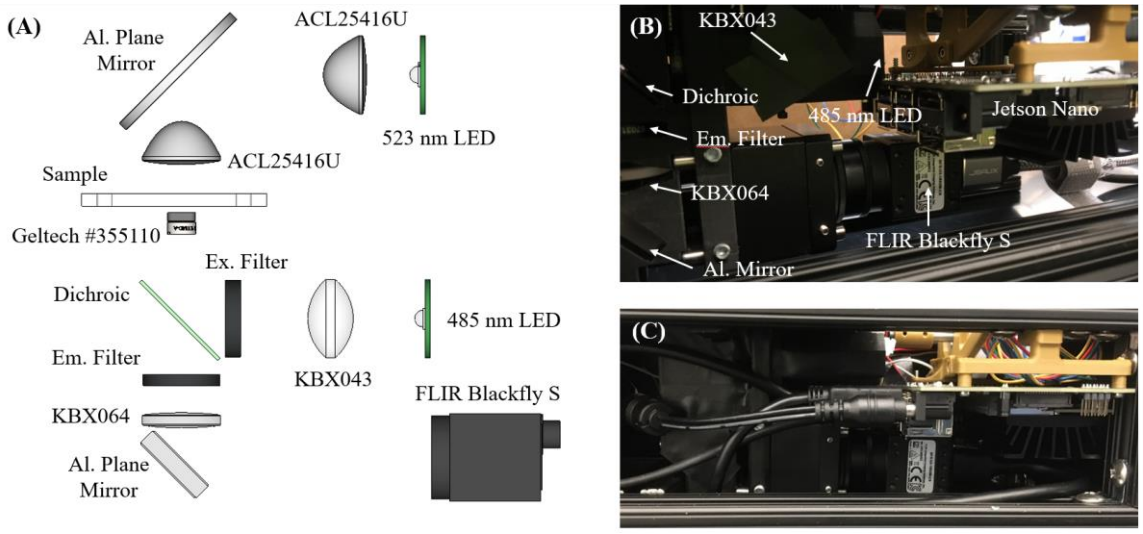

Figure 41: (A) Layout of optical components in the portable microscope. (B) Microscope base showing imaging system optics in partially constructed microscope. (C) Microscope base after electronic components have been connected.

To hold samples in a horizontal, level position (necessary for microfluidic cartridges), the microscope was assembled with illumination system housed in the lid of the system and the imaging and control components in the base. To operate, the lid was opened, sample placed onto the stage, then the lid was closed before imaging. The system was designed so that either dry thin blood smears mounted to conventional 75 mm x 25mm glass slides or smears created inside microfluidic cartridges could be placed into interchangeable clips for imaging, giving the microscope adaptability to either sample preparation format (Fig. 42a & 42b). When the lid closes, it applies a sandwiching pressure to the interchangeable clips, holding samples to the stage and ensuring that samples are roughly aligned with the focal plane of the microscope. Either of two stepper motors (Sparkfun, Boulder, CO; # ROB-09238) could be activated to laterally translate the sample or fine-tune focus as needed. Given that the microscope FOV was tuned to match the width of the microfluidic channel, translation in a single axis was sufficient to image the entire cartridge-based smear, provided that it is properly aligned with the direction of translation. When imaging conventional thin smears, the 60 mm translational throw distance allowed for collection of approximately 180 FOV with a well-made smear.

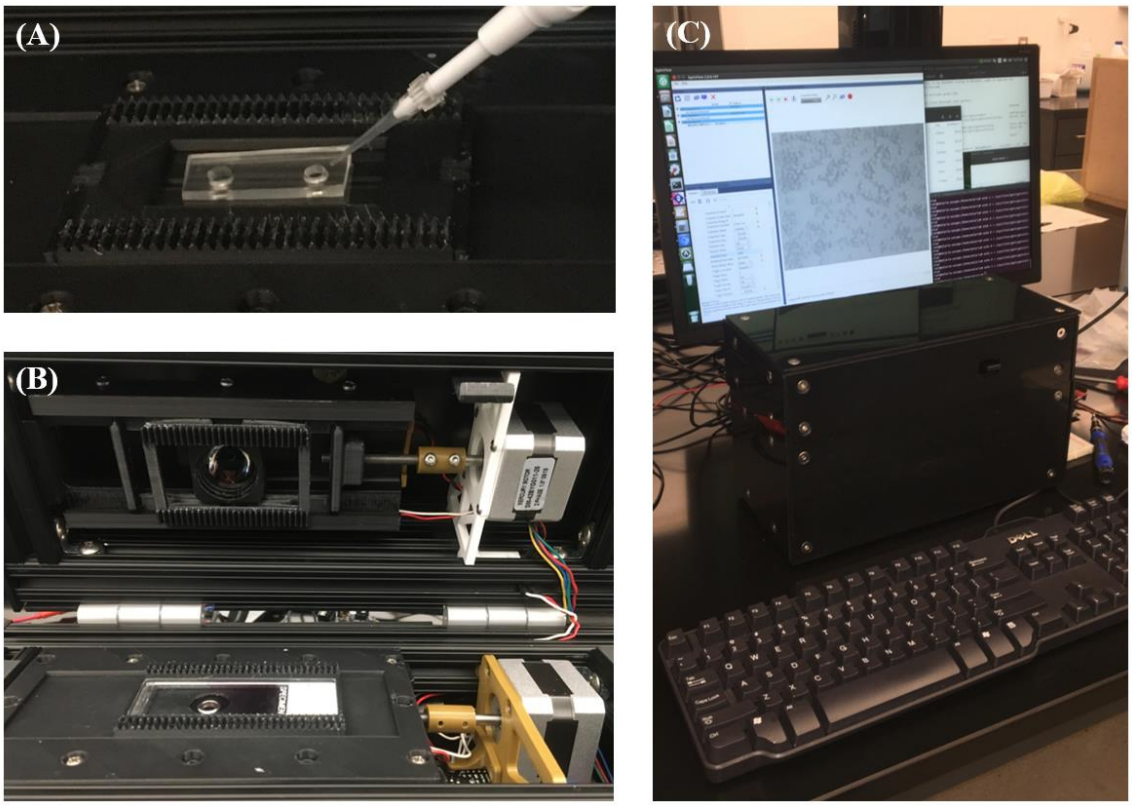

Figure 42: (A) Sample being pipetted into microfluidic channel in clip. (B) A glass slide-mounted thin smear positioned in the open microscope, ready for imaging. Top motor assembly translates sample, while bottom controls objective focus. (C) The completed portable microscope in use collecting data.

Optical Characterization

Two methods were employed to assess the resolution capabilities of the system, with the first being to collect images of the 1951 US Air Force Resolution Target (USAFT) using brightfield illumination (Fig. 43). Results show that the system in its current form is fully capable of resolving sub-micron features, as shown by the clear resolution of all group nine elements, with contrast of over 0.5 being resolved for element 9-1, which has a line width of 0.91 μm. This implies that the system cutoff frequency approaches the

theoretical diffraction limit of 0.793 µm by the Rayleigh criterion. Further analysis of the US Air Force Target images shows that the net system magnification is experimentally measured to be 16.03x, exactly the theoretical magnification predicted by the ratio of the tube lens focal distance (f = 100 mm) to that of the objective lens (f = 6.24 mm). At this magnification, each camera pixel represents 0.215 µm x 0.215 µm of object space, allowing the system to satisfy the digital sampling requirements according to the Nyquist Sampling Theorem for features above 430 nm in size.

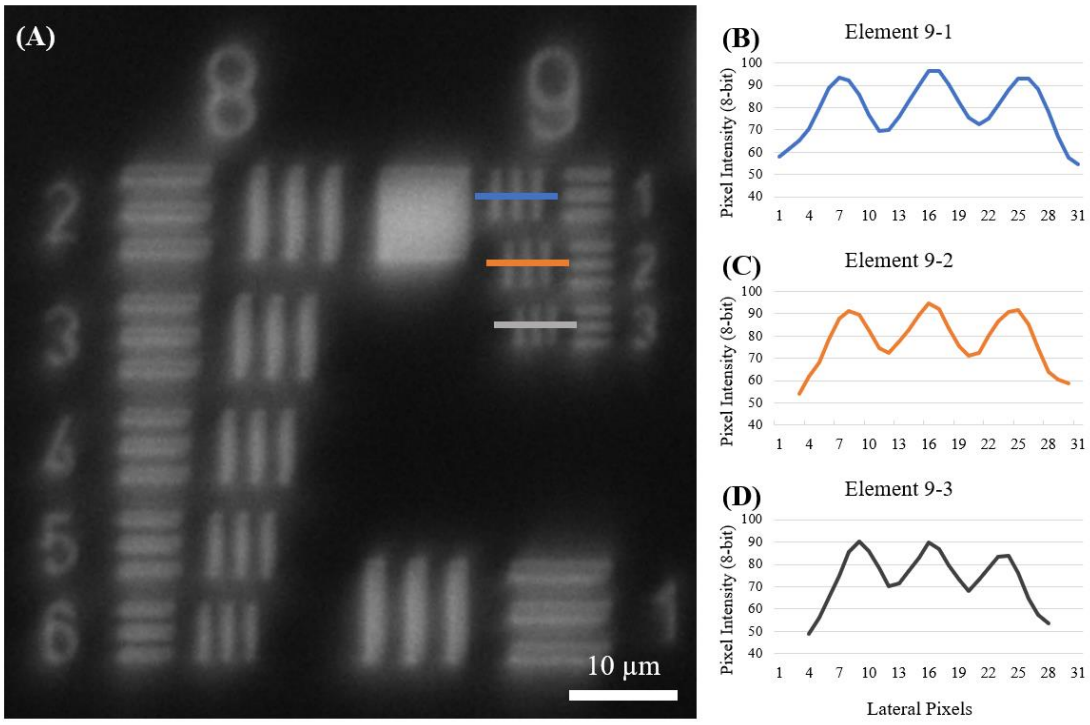

Figure 43: (A) Image of 1951 US Air Force Target captured using the portable microscope. Profiles from rectangular sections taken across elements (B) 9-1: 0.98 µm; (C) 9-2: 0.87 µm; and (D) 9-3: 0.78 µm are shown at right.

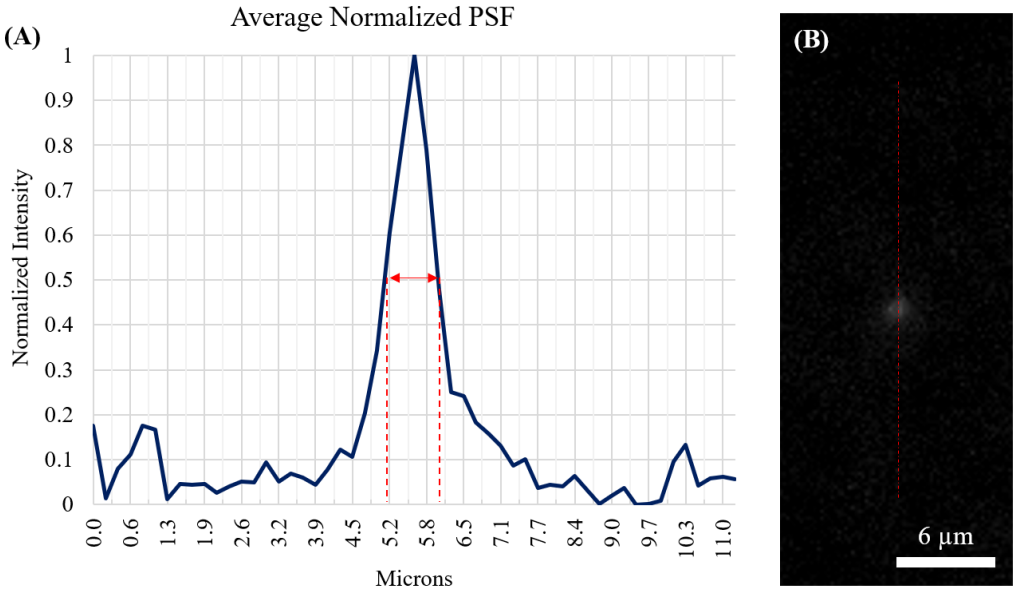

Figure 44: (A) Measured point spread function for the microscope. Eight separate sections through sub-resolution fluorescent features such as that in (B) were normalized, then averaged to create the net PSF.

The second method used to assess system imaging performance was to approximate the microscope's point spread function (PSF) using linear cross sectional profiles through eight sub-resolution fluorescent particles found in sample images. Horizontal cross sections through eight different small fluorescent features were collected, then linearly normalized and averaged together to create a smoothed, normalized PSF (Figure 44). Due to the normalization procedure employed, it is expected that the resulting function is not a true PSF representative of the dispersion of a theoretical delta function being passed through the system. Rather, it is simply a tool to measure the transverse spreading of light from sub-resolution features. After all normalized PSF's were averaged

together, the full-width-half-max distance was calculated using linear interpolation to be 4.47 pixels, or 0.963 μm.

Quantitative Parasitemia Measurement

Materials and Methods

Wild-type *P. falciparum* parasites were cultured in cell media until growth cycles were desynchronized and multiple morphologies across the erythrocytic cycle could be found simultaneously in test smears. From this culture, several mL of parasitized red blood cells were centrifuged in two-minute increments at 0.2 x 1,000 rcf to form a loose pellet of concentrated RBC's. These pellets were then extracted from all spun-down cultures, collected into a single tube, and the process repeated twice more until nearly all cell media was separated from the parasitized RBC's. This concentrated culture pellet was resuspended in equal volume fresh human blood plasma to create an approximate parasitized human blood analog, but which contained no white blood cells. White blood cells were removed so that that state of parasitic infection could be preserved for as long as possible in the reconstituted culture. From Giemsa-stained control slides, the parasitemia of the raw culture was measured to be between 1.07-1.3 parasites per 100 RBC's, and dilutions were further mixed based on the assumption of culture parasitemia equal to 1.2 parasites/100 RBC's (1.2%). When various parasitemia dilutions were created, they were created by mixing volumes of this reconstituted parasitized culture with whole human blood. Dilutions were created to target parasitemia levels of 1%

(50,000/µL), 0.75% (37,500/µL), 0.5% (25,000/µL), 0.25% (12,500/µL), 0.1% (5,000/µL), 0.05% (2,500/µL), and 0.01% (500/µL). At least eight smears were made using each dilution as well as the raw culture and whole, unparasitized blood (0.0% parasitemia). Control smears were stained using CDC recommended Giemsa staining techniques for each dilution.

Fluorescent staining solution for dry thin smears was created by dissolving SYBR Green 1 stock at 1:8,000 dilution in 1x Tris-HCL buffer pH 8. To create fluorescently stained thin smears, previously fixed thin smears on 25mm x 75mm x 1mm slide glass were flooded with approximately 500 µL of this SYBR stock solution and allowed to incubate for five minutes in the dark. Afterwards, all smears were rinsed for approximately 10 seconds with a stream of DI water and allowed to air dry in the dark. Acridine Orange stock solution was prepared by diluting AO powder to 100 µg/mL in 1x PBS pH 7.4. To stain blood dilutions in channels, the in-tube staining procedure as described in Chapter 2 was implemented. In short, one-part stain was mixed with two-parts blood in a centrifuge tube for five minutes, then 0.3 microliters of the stained blood were pipetted into the microchannel inlet, allowing cells to flow via capillary force and create a thin smear.

To collect quantitative parasitemia measurements, the portable microscope was connected to an auxiliary display monitor, keyboard, and mouse to control the user interface used to capture images, activate LED's, change exposure settings, and translate the sample. Two smears from each dilution were imaged first on the portable system, then on the benchtop system. Fluorescent images were captured first for each FOV to minimize the effects of photobleaching due to brightfield illumination incident on the sample.

Brightfield images were captured immediately afterwards, then the sample was translated to the next FOV, and the process repeated until an adequate number of images were captured using the portable system. If the preview image displayed on the screen did not contain a homogenous monolayer of cells, the sample was translated until the next viable FOV appeared. Focusing the objective was necessary before the first image was captured for each slide, but re-focusing was typically unnecessary throughout the imaging of each individual slide. Once imaging of a smear was completed on the portable system, it was immediately imaged on the benchtop Nikon Ti-82 inverted fluorescence microscope using a 20x objective and FITC fluorescence filter set. Fluorescence images were again captured first, then brightfield images. This process was also repeated for one slide each of the un-diluted culture and the non-parasitic whole blood control slide.

Results

Images of red blood cells gathered from samples show clear resolution of cells in brightfield mode, both inside microfluidic channels and on conventionally fixed and stained dry samples on the front surface of glass slides. Because of inconsistencies associated with microfluidically generated smears during data collection, primary microscope functionality assessment was conducted using conventional dry thin smears made using glass microscope slides. The average cell distribution typically found on such a conventional smear was 670 red blood cells per field of view.

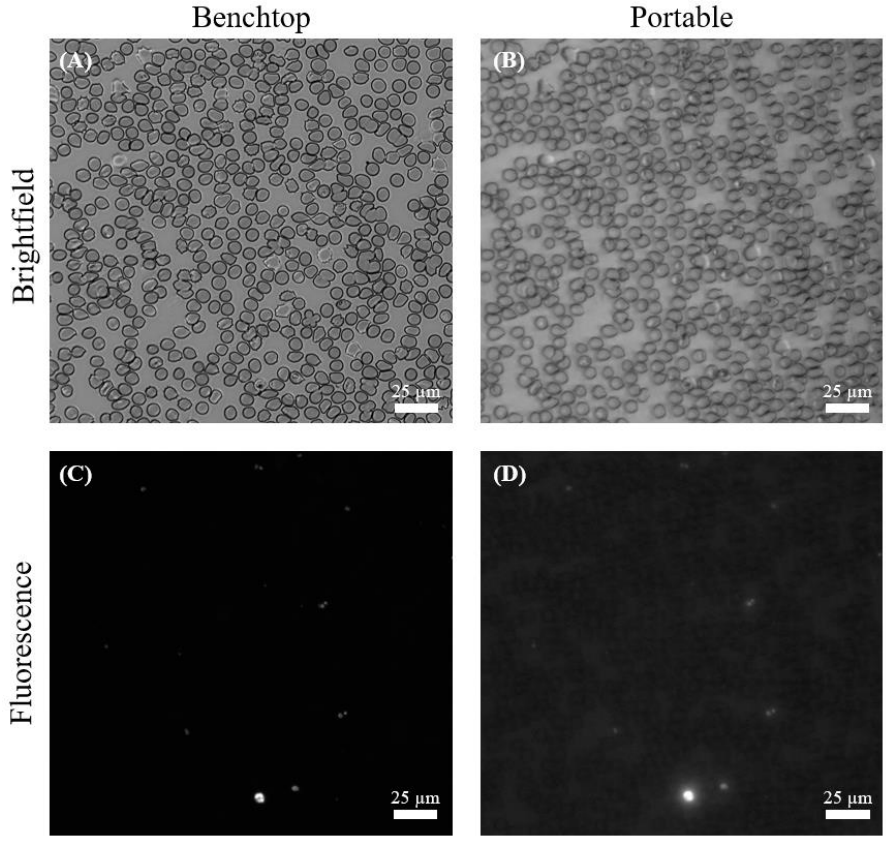

Figure 45: Brightfield and fluorescence images from the same FOV for the (left) benchtop control, and (right) portable microscope. Images have been linearly contrast enhanced.

When comparing brightfield images of the same sample gathered on both the prototype microscope and the benchtop control, the benchtop system clearly shows more definition of cell boundaries and allows for variances in erythrocyte shading to be seen, whereas this is difficult to identify in prototype images (Fig. 45). Fluorescent images from the prototype system showed higher background fluorescence than their benchtop counterparts. The exposure times necessary to capture images using the portable system were 100 ms for fluorescence images and 15 ms for brightfield images. Subsequent

brightfield and fluorescent images for several FOV were collected on both systems with minimal pixel shifting between modes, allowing cross-comparison and simple image addition to create the composite images shown in Fig. 46.

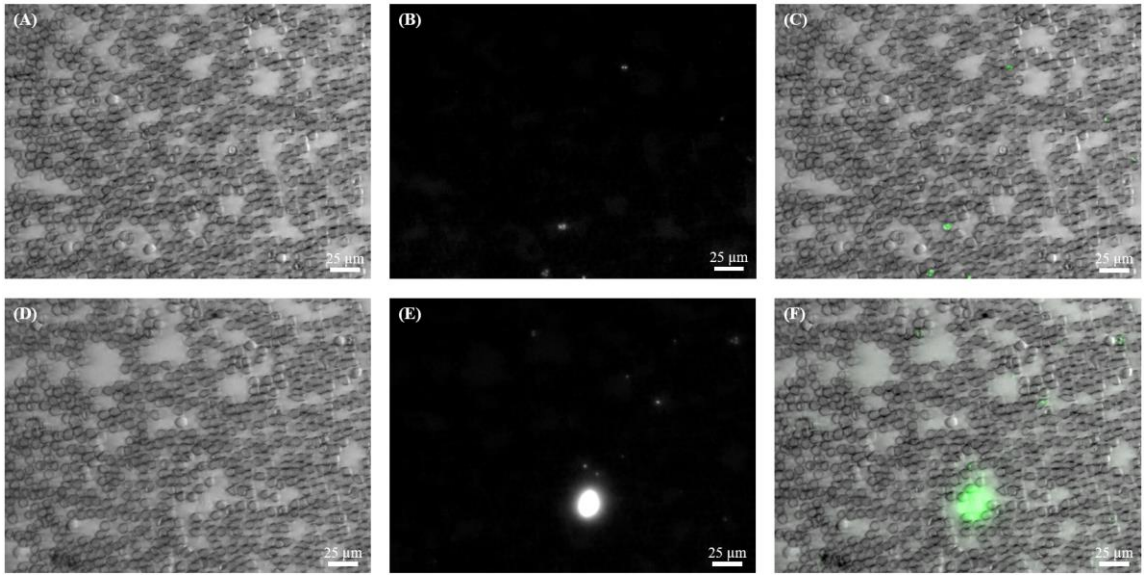

Figure 46: Two different FOV from the portable microscope (top row, bottom row respectively). (A, D) show brightfield images, (B, E) show fluorescence images, and (C, E) show stacked composites with fluorescence image being false colored. Note the large white blood cell in image (E). Images shown have been linearly contrast enhanced.

In order to translate image data into quantifiable parasitemia measurements, the number of both parasites and red blood cells must be collected from each image. Macros were written in ImageJ/FIJI to perform all processing tasks consistently across all images and minimize bias during the process. Red blood cells per brightfield images were counted by finding the local maxima of the Laplacian transform of each image. Parasite segmentation from fluorescent images was done in a two-step process in order to gather

wholistic image object information. The first operation was to segment all fluorescent objects from images, and the second operation was to set object thresholds to classify each object as either an actual parasite or an artifact / false positive. Initial, conservative segmentation of objects in fluorescent images was performed by automated intensity thresholding from a background-subtracted image. Masks created from all thus segmented objects were applied to original fluorescent images, and all resulting objects measured for pixel maximum and mean intensities, size, and circularity. From the distributions of these four parameters, further thresholds were set to classify objects. To ensure consistent treatment and again minimize the effect of subjective bias on final classification, ranges of all possible thresholds were set based on observation of manually classified parasites, then fine-tuning of exact thresholds within those ranges was computationally optimized.

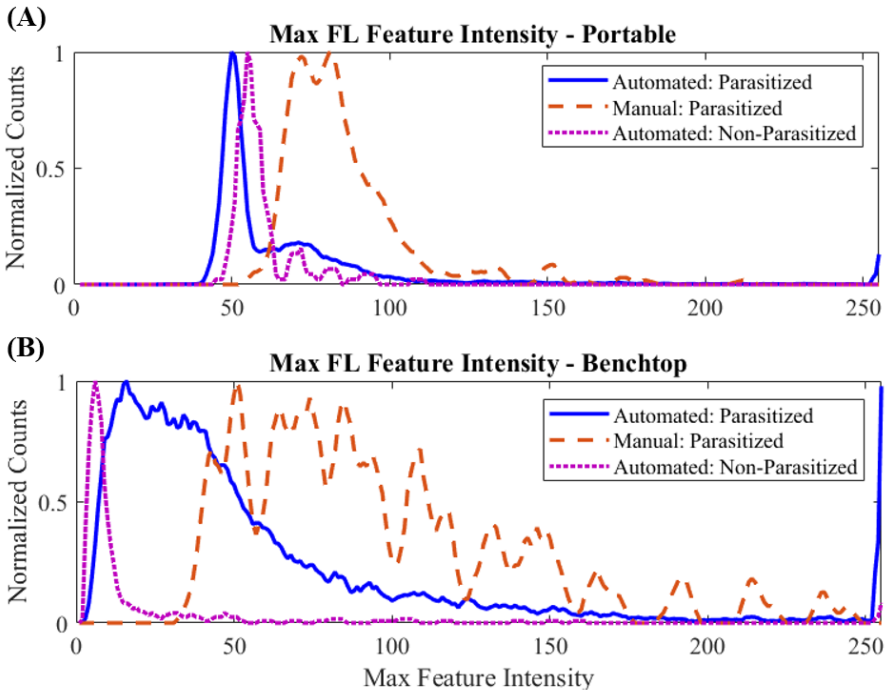

Figure 47: Comparative histograms showing the distributions of maximum intensities in fluorescent features segmented by initial automated threshold (blue-solid), manual segmentation (orange-dashed), and automatically segmented in a non-parasitized control smear (magenta-dotted) for both the (A) portable microscope and (B) benchtop microscope.

The most discriminating feature that showed clear separability between parasites and non-parasites was feature maximum intensity, as the majority of artifacts displayed a peak fluorescence intensity well below that of parasites and image exposure was tuned to prevent parasites from saturating the maximum dynamic range of the camera. Histograms for feature maximum intensity were plotted for objects from both parasite-containing samples and for control "non-parasitized" samples using the automated segmentation macro written in FIJI/ImageJ. Then, fluorescent features subjectively judged to be parasites were manually segmented, and the distributions of their maximum intensities

were overlaid with the original histograms to show the contrast between the raw and defined feature distributions (Fig 47). The valley between the distribution of manually classified parasites and fluorescent objects from control images in these comparative histograms were then used to set the specific thresholding ranges to further specify which fluorescent markers were to be classified as parasites and which would be classified as artifacts. Feature area and circularity were also used to set minimum and maximum bounds for objects allowed to be classified as parasites, however this could not be implemented in the same way as using maximum intensity because the specific sizes and shapes of manual and automatically segmented objects are not guaranteed to align. Rather, conservative bounding ranges set based on observation of the sizes and shapes of subjectively classified non-parasitic objects in images were used. This process allowed for the disqualification of clearly non-parasitic features such as dead pixels or white blood cells. While separate classification thresholds were defined for each of the portable and benchtop systems, once set, they were applied equally to all images for each respective system. Figs. 48 and 49 show the distribution of fluorescent object parameters both before and after classification processing.

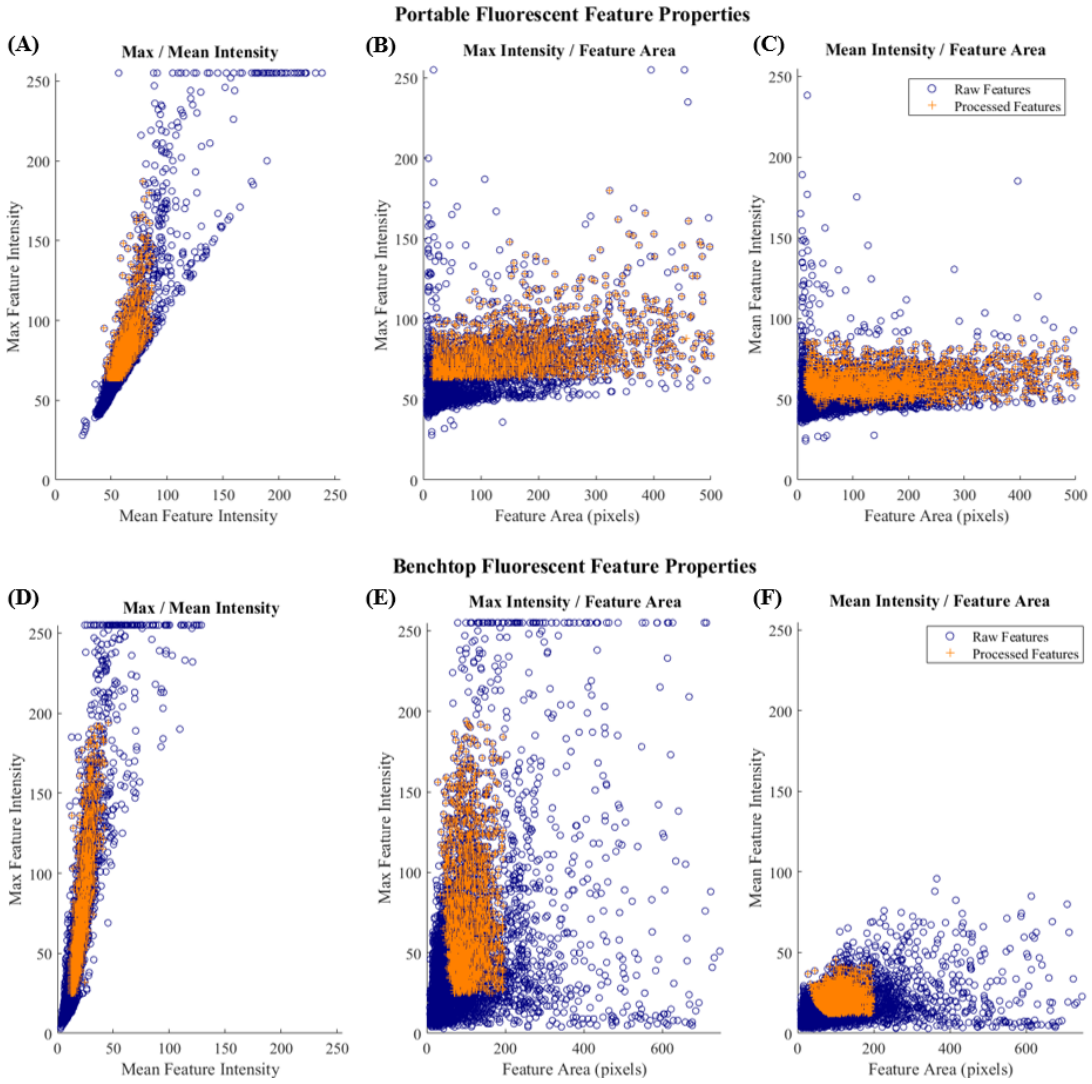

Figure 48: Scatterplot distributions for all fluorescent objects from parasitized smears for both (A-C) portable microscope and (D-F) benchtop microscope. Raw, unprocessed features are indicated by blue circles, while features classified as parasites are again plotted as orange crosses.

Table 11: Sample sizes of all smears, cells, and fluorescent objects

		Portable				Benchtop			
Smear	Intended Parasitemia	# FOV	# Cells	Raw Objects	Processed Objects	# FOV	# Cells	Raw Objects	Processed Objects
1	1.200%	21	12477	455	207	6	15441	754	244
2	1.000%	26	13998	203	203	3	8247	107	107
3	1.000%	19	12903	197	182	7	25817	406	294
4	0.750%	50	30923	290	287	8	39139	215	215
5	0.500%	10	7231	53	53	4	18703	98	98
6	0.500%	25	17524	90	90	5	24216	111	111
7	0.250%	9	6635	23	23	2	7045	43	16
8	0.250%	24	14401	69	52	6	22843	103	88
9	0.100%	20	15355	64	64	5	23089	43	43
10	0.100%	17	11528	44	35	5	26413	45	42
11	0.050%	25	22557	51	51	5	28322	32	15
12	0.050%	13	9657	37	24	4	18215	33	33
13	0.010%	35	18593	115	115	10	42366	85	85
14	0.010%	32	24145	104	92	5	22662	64	64
15	0.004%	18	13456	17	17	6	29521	4	4
16	0.000%	10	6763	15	15	2	5248	9	2

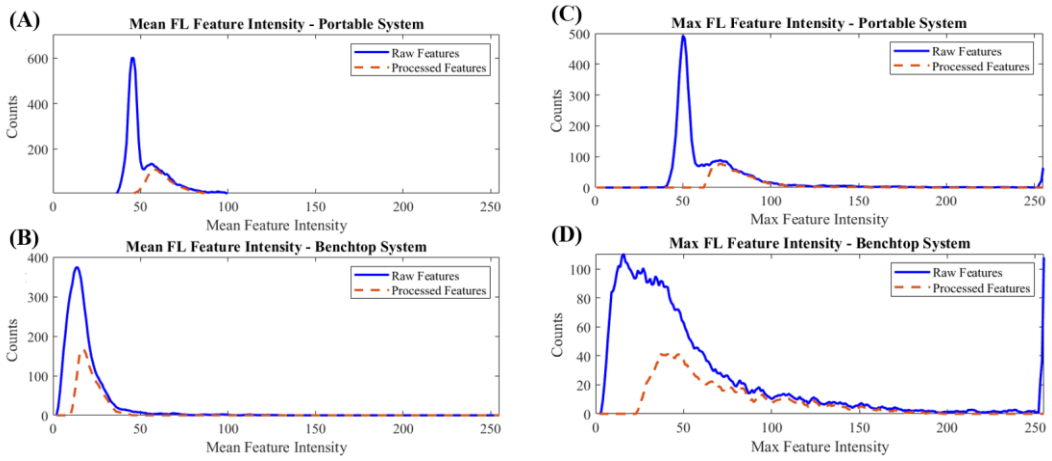

Figure 49: Distributions for (A, B) mean feature intensities and (C, D) max feature intensities both before (blue, solid) and after (orange, dashed) classification.

After tuning the segmentation thresholds, the number of parasites and red blood cells from each field of view were tabulated, then the ratio of parasites to total red blood cells was plotted for the portable system and the benchtop system to assess the agreement in parasitemia measurements between the two systems (Fig. 50). A linear regression was fit to the dataset to quantify the degree of agreement between the two sets of measurements, with $R^2 = 0.939$ and slope = 0.996.

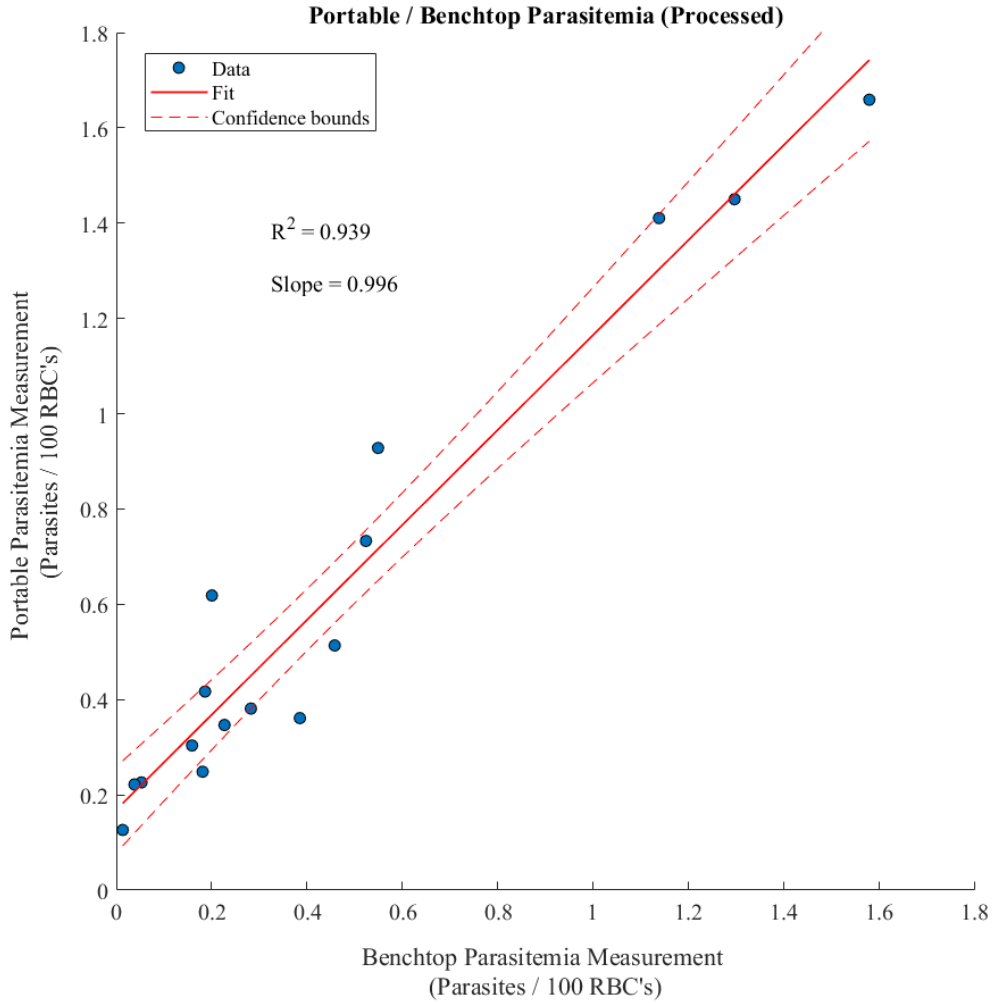

Figure 50: Correlation between parasitemia measurements collected using the portable and benchtop microscopes.

Imaging Performance with Alternative Smear Types

The ability of the microscope to image smears created in microfluidic channels was tested. While an insufficient number of successful in-channel smears were collected to permit quantitative parasitemia measurements in this format, well-made smears were able to be successfully imaged using the portable microscope. Images of a thin microfluidic smear stained with Acridine Orange can be seen in Fig. 51.

Figure 51: Images of Acridine-Orange stained samples in-channel with (A) brightfield, (B) fluorescence, and (C) composite image with false coloration on the fluorescence channel for contrast. Images have been linearly contrast enhanced for clarity.

Thick smears were also imaged using the portable system. Samples were mounted on standard glass microscope slides using cells stained using the same in-tube procedures as were implemented for microfluidic smears, and images were collected in the same manner as all thin smears. Although the nature of the thick smear prevents quantitative analysis of the number of red blood cells, both immature and mature parasites are still clearly visible in the fluorescence images and can easily be tabulated, indicating that microscopic detection and approximate parasitemia quantification may be possible using only fluorescence imaging to approximate WHO and CDC recommended thick smear

examination protocols. However, further investigation is merited to develop a robust understanding of quantitative parasitemia relationships, the limit of detection, and the effects of potential fluorescent artifacts creating by the lysing of red and white blood cells. It is expected that stained leukocytic granules and material may be especially difficult to discriminate from parasites in these images. Examples of thick smear images can be seen in Figure 52, with little apparent information available in brightfield images.

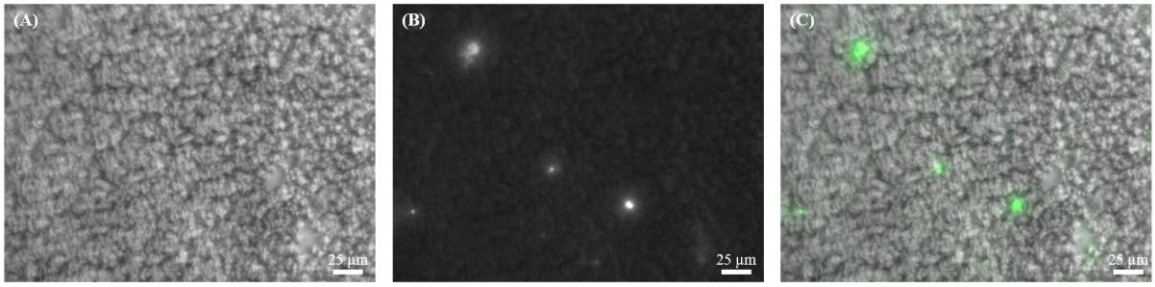

Figure 52: Images of a thick smear imaged on the portable microscope. (A) Brightfield image with indistinguishable erythrocytes. (B) Fluorescence image showing the presence of both immature and mature parasites. (C) Composite image. Images have been linearly contrast enhanced for clarity.

Cost Analysis

A bill of materials for all major optical and electronic components is presented in Table 12 along with associated costs. The total cost of the prototype microscope system is approximately $1,300, excluding the cost of non-critical components likely to be significantly changed for future field deployment. Examples of such minor components include fastening hardware, case rails, 3-D printed mounts, and wiring cables/adapters. The estimated total cost of such minor components is estimated to be around $300, but

this cost is likely to be significantly reduced by potential manufacturing optimizations. Brief examination of the cost breakdown reveals that approximately 50% of the current cost is allocated to the interference filter set used to generate fluorescence contrast. While this cost may not be possible to eliminate entirely, it is expected that it can also be significantly reduced by economies of scale and the reduction in size possible if only the necessary surface area is used for each filter component. Even in its current form, the cost associated with the system is significantly less than base model benchtop fluorescence microscopes, which retail for >$3,000 USD. While it is more expensive than simple compound benchtop microscopes that range in cost from $300-1,000 USD, these systems are not portable and do not have the onboard computational power required to provide the automation necessary to allow parasitemia quantification to be possible in remote settings by those without extensive skill and infrastructure. The prototype microscope presented here is comparable in price to predicate portable medical tools and systems such as Lab-In-A-Backpack prototypes, (~$1,500) [175].

Table 12: Costs of major components in portable microscope prototype.

Description	#	Price/ea.	Total Price
Nvidia Jetson Nano	1	$89	$89
Sparkfun Stepper Motor #ROB-09238	2	$17	$34
FLIR Blackfly S 1.6MP Mono	1	$315	$315
Geltech Asphere Lens #355110	1	$98	$98
Newport Bi-Convex Lens #KBX064	1	$41	$41
Newport Bio-Convex Lens #KBX043	1	$41	$41
Thorlabs Asphere Lens #ACL25416U	2	$19	$38
Semrock Filter Set #FITC-LP01-Clinical-000	1	$625	$625
Osram 523nm Green LED # LZ1-00G102-0000	1	$5	$5
CREE 485nm Blue LED #XPEBBL-L1-0000-00301	1	$2	$2
		Total Cost:	$1318

To the author's knowledge, this would represent the lowest cost of a portable multimodal microscopy platform capable of both collecting and automatically processing data necessary to provide quantitative parasitemia information for malaria patients at the point-of-care. The net cost per test would then primarily be the cost of renewables (slides, cartridges, stains, etc.), with the microscope cost being divided across the number of tests performed in its useful lifetime. Without durability studies or field testing, it is impossible to assess the device's theoretical useful lifespan and thus cost per test, however, it is entirely possible that the cost per test could be at or below the $10 ICER for benchtop microscopy as described in Chapter 1.

Discussion

By optimizing a microscopy system to address a highly specific diagnostic gap, its complexity and cost have been reduced toward practical utility in the developing world. This prototype microscope represents a developmental step towards an automated, low-cost method for quantitative parasitemia measurement by healthcare workers while away from a centralized microscopy laboratory. Preliminary results indicate that the current prototype can quantify parasitemia with high correlation to that provided by benchtop microscopy, albeit with an apparent baseline false-positive rate of approximately 0.2 parasites per 100 RBC's, or 10,000 parasites per microliter, which is equivalent to approximately 1.3 objects per FOV. While this lower limit of quantification is sufficient to inform most diagnostic decisions, it constrains the monitoring of parasite clearance to relatively high parasitemia cases. If a patient with 2% of cells infected was treated, they would progress to be below the current detection limit in a minimum of approximately 12 hours with a nominally resistant infection up to approximately 24 hours with a resistant infection. It is likely that this lower limit of detection could be significantly lowered with improved fluorescence/artifact classification, possibly using the machine learning/neural network processing capabilities of the onboard Jetson Nano platform.

A useful next step would be to use the prototype system to collect images from actual malaria patients. This would be informative for multiple reasons, including the ability to gather control parasitemia data from full-time malaria microscopists and the ability to image patient blood that is likely to be different from that in reconstituted cultures. Gathering more representative data that would more fully encapsulate the

diversity of possible hematological conditions would be essential for training an effective classification algorithm. Additionally, the presence of physiologically relevant numbers of leukocytes in the blood would facilitate a study of the accuracy and utility of thick smears for detection and parasitemia quantification using this system. It would also be very useful to assess how actual parasite clearance rates vary when compared to those portrayed in the theoretical average decay model in Fig. 37, as the plots do not necessarily reflect the inherent fluctuations in peripheral parasite circulation due to the their erythrocytic infection and schizogony cycles.

CHAPTER VI

SUMMARY AND CONCLUSIONS

In summary, this dissertation presents a record of research activities to investigate and develop a portable microscopy system for malaria diagnosis and monitoring at the point of care. Clinical and pathological contexts were examined to better inform the direction of technological development for the portable microscope. Previous microscope iterations had demonstrated that it was possible to detect malaria using a cross-polarized, cell phone based system, and a new portable microscope was proposed that would use a tri-modal brightfield, fluorescence, and cross-polarized approach to maximize the amount of information provided for malaria diagnosis. A prototype tri-modal system was built, and testing revealed that it was successful in detecting parasites in thin blood smears that were stained using either Acridine Orange or SYBR Green-1 fluorescence stains. Drawbacks to the system included its low sampling rate, complexity of operation, and reliance on high-cost optical components.

Several separate novel investigations were simultaneously initiated to increase the utility of the entire portable microscopic system. Firstly, sample preparation methods were investigated to optimize the creation of fluorescently stained thin smears. While the use of microfluidic channels to create thin smears had been previously demonstrated, the system was inadequate for use in the portable microscope because the staining procedures were only adapted for Giemsa staining, and the glass cartridge substrate was prohibitively thick for imaging using low cost optical components. The microfluidic cartridges were

modified to utilize thin polycarbonate plastic as an alternative substrate that improved the durability of the cartridges and minimized optical aberrations in imaged collected using the portable trimodal microscope. A single-step process to fluorescently stain blood samples with Acridine Orange stain was developed and shown to provide adequate contrast to allow for detection of parasites inside of the microfluidic channels.

While the preparation of thin smears using microfluidic channels offers promise in improving the simplicity and reliability of smear creation, the technology still lacks many improvements necessary to be considered a viable option for use at the point of care. Specifically, current cartridge-based smears are not stable and shift frequently, oftentimes causing the smear to be entirely altered during imaging. Smears used for multimodal imaging must necessarily be stable so that consecutively gathered images align and allow for the quantification of parasites and blood cells in each field of view. Additionally, the skill required to use the cartridges is still higher than is practical to expect for use by non-expert personnel at the point of care. Ultimately, cartridge operation may become consistent enough to merit full integration into a portable microscopy system, but it is recommended that any field studies be conducted with dry, traditional thin smears affixed to glass microscope slides, pending significant improvement to the cartridge technology.

The second independent research venture initiated was the discovery and testing of a novel rapid fabrication technique for parabolic aspheric lenses. The lenses were created by curing polymer in a steady-state spinning crucible. This process allowed for exceptionally smooth parabolic surfaces to be formed in the polymer, with surface roughnesses that are comparable in quality to mid-to-high-end polished glass lenses from

major optical manufacturers. The combination of these surfaces allowed for three distinct lens geometries to be fabricated. Plano-convex lenses made in this manner were hypothesized to be usable as collector and condenser lenses in the illumination system of the prototype microscope, but time constraints in their development prevented them from being incorporated as preferable options to commercially available glass lenses in the final microscope prototype. There is some reason to believe that polymeric lenses used in a field-deployable microscope system may prove to be more durable than glass counterparts. Ultimately, the novel lens manufacturing technique has its primary utility in fundamental research and as a potential rapid lens prototyping system. Future works to follow this line of inquiry could possibly include investigations into photo-curable polymers, fidelity for large-diameter geometries, surface coating techniques to create mirrors, use of immiscible fluids during curing, and off-axis centrifugation to create varying parabolic profiles.

A secondary prototype portable microscopy system that is also more specifically targeted to the unmet need of parasitemia quantification was created to research its potential as a low-cost, bi-modal alternative to the initial device. The cross-polarized imaging modality from the previous system was dropped, as detecting the presence of hemozoin was determined to add cost to the system and contribute little diagnostic or monitoring value. Brightfield imaging was still utilized to define red blood cell boundaries in images, and fluorescence images were used to identify and locate parasites in thin blood smears. The system successfully incorporated singlet objective and tube lenses while preserving sub-micron resolution and incorporated a more robust camera to improve sensitivity and imaging FOV size. Being built around a portable computer capable of

running sophisticated neural networks allows the portable microscope to potentially perform automated onboard image processing with additional future development.

Results of imaging varying concentrations of parasitized cultures in whole human blood using the portable microscope showed that parasitemia measurements have a strong correlation with those measured using a comparable benchtop system. However, current image processing procedures include a baseline of false-positive fluorescent objects in images that were present across all samples, limiting the current lower bounds of parasitemia detection to be above 0.2%. While this lower bound is theoretically sufficient to inform diagnostic decisions, it is only useful for quantifying post-treatment parasite clearance rates if the patient presents a relatively high parasitemia to begin with. This is a drawback to the current system, but there is strong reason to believe that a more sophisticated fluorescent object classification system could push the limit of quantifiable detection to a lower, more consistently applicable level. At the conclusion of this research effort, the cost of the critical components in the portable microscopy system were approximately $1,300 USD. It is believed that this cost could be further reduced during manufacturing optimization, but even this price is below that of most commercially available fluorescence benchtop microscopes. If this technology can continue to be developed and successfully commercialized, it has the potential to be a valuable tool for the augmentation of malaria diagnosis and monitoring technologies in a variety of settings and applications.

REFERENCES

1. Carter, R. and K.N. Mendis, *Evolutionary and historical aspects of the burden of malaria.* Clinical Microbiology Reviews, 2002. **15**(4): p. 564-594.

2. Adams, F., *The genuine works of Hippocrates*. 1886.

3. Poinar, G., *Plasmodium dominicana n. sp.(Plasmodiidae: Haemospororida) from Tertiary Dominican amber.* Systematic Parasitology, 2005. **61**(1): p. 47-52.

4. Hempelmann, E. and K. Krafts, *Bad air, amulets and mosquitoes: 2,000 years of changing perspectives on malaria.* Malaria Journal, 2013. **12**(1): p. 232.

5. Laveran, A., *A new parasite found in the blood of malarial patients. Parasitic origin of malarial attacks.* Bulletins et Memoires de la Societe Medicale des Hopitaux de Paris, 1880. **17**: p. 158-164.

6. *World Malaria Report 2019*. 2019, Global Malaria Programme, WHO (World Health Organitation) Global: Geneva. http://apps.who.int/iris/bitstream/10665/200018/1/9789241565158_eng.pdf?ua=1.

7. *World malaria report 2015*. 2015, Global Malaria Programme, WHO (World Health Organitation) Global: Geneva. https://apps.who.int/iris/rest/bitstreams/1262394/retrieve.

8. Brasil, P., et al., *Outbreak of human malaria caused by Plasmodium simium in the Atlantic Forest in Rio de Janeiro: a molecular epidemiological investigation.* The Lancet Global Health, 2017. **5**(10): p. e1038-e1046.

9. Prevention, C.f.D.C.a., *Malaria Biology.* 2016. Accessed at: https://www.cdc.gov/malaria/about/biology/index.html.

10. D'Acremont, V., et al., *Time to move from presumptive malaria treatment to laboratory-confirmed diagnosis and treatment in African children with fever.* PLoS Medicine, 2009. **6**(1): p. e252.

11. *Malaria rapid diagnostic test performance: results of WHO product testing of malaria RDTs: round 6 (2014-2015).* 2015. World Health Organization: Geneva.

12. Coleman, R.E., et al., *Comparison of field and expert laboratory microscopy for active surveillance for asymptomatic Plasmodium falciparum and Plasmodium vivax in western Thailand.* American Journal of Tropical Medicine and Hygiene, 2002. **67**(2): p. 141-144.

13. Drakeley, C. and H. Reyburn, *Out with the old, in with the new: the utility of rapid diagnostic tests for malaria diagnosis in Africa ☆.* Transactions of the Royal Society of Tropical Medicine and Hygiene, 2009. **103**(4): p. 333-337.

14. Hanboonkunupakarn, B. and N.J. White, *The threat of antimalarial drug resistance.* Tropical Diseases, Travel Medicine and Vaccines, 2016. **2**(1): p. 10.

15. Oladosu, O.O. and W.A. Oyibo, *Overdiagnosis and overtreatment of malaria in children that presented with fever in Lagos, Nigeria.* ISRN Infectious Diseases, 2012. **2013**. Accessed at: https://www.hindawi.com/journals/isrn/2013/914675/#copyright.

16. O'Meara, W.P., D.L. Smith, and F.E. McKenzie, *Potential impact of intermittent preventive treatment (IPT) on spread of drug-resistant malaria.* PLoS Medicine, 2006. **3**(5): p. e141.

17. Manguin, S., et al., *Malaria overdiagnosis and subsequent overconsumption of antimalarial drugs in Angola: Consequences and effects on human health.* Acta Tropica, 2017. **171**: p. 58-63.

18. Batwala, V., et al., *Cost-effectiveness of malaria microscopy and rapid diagnostic tests versus presumptive diagnosis: implications for malaria control in Uganda.* Malaria Journal, 2011. **10**(1): p. 372.

19. *Guidelines for the treatment of malaria*. 2006: World Health Organization: Geneva.

20. Chiodini, P.L., *Malaria diagnostics: now and the future.* Parasitology, 2014. **141**(14): p. 1873-1879.

21. Hume, J.C., et al., *Household cost of malaria overdiagnosis in rural Mozambique.* Malaria Journal, 2008. **7**(1): p. 33.

22. *Basic Malaria Microscopy: Part I. Learner's Guide*. 2010, World Health Organization: Geneva.

23. Pasvol, G., *The treatment of complicated and severe malaria.* British Medical Bulletin, 2005. **75**(1): p. 29-47.

24. *Global technical strategy for malaria 2016-2030*. 2015, World Health Organization: Geneva.

25. *Malaria eradication: benefits, future scenarios and feasibility.* 2020, World Health Organization: Geneva.

26. Payne, D., *Spread of chloroquine resistance in Plasmodium falciparum.* Parasitology Today, 1987. **3**(8): p. 241-246.

27. Wootton, J.C., et al., *Genetic diversity and chloroquine selective sweeps in Plasmodium falciparum.* Nature, 2002. **418**(6895): p. 320-323.

28. White, N.J., *Antimalarial drug resistance.* The Journal of Clinical Investigation, 2004. **113**(8): p. 1084-1092.

29. Menard, D. and A. Dondorp, *Antimalarial drug resistance: a threat to malaria elimination.* Cold Spring Harbor Perspectives in Medicine, 2017. **7**(7): p. a025619.

30. Dondorp, A.M., et al., *Artemisinin resistance in Plasmodium falciparum malaria.* New England Journal of Medicine, 2009. **361**(5): p. 455-67.

31. Dondorp, A.M., et al., *Artemisinin resistance in Plasmodium falciparum malaria.* New England Journal of Medicine, 2009. **361**(5): p. 455-467.

32. Bell, D., C. Wongsrichanalai, and J.W. Barnwell, *Ensuring quality and access for malaria diagnosis: how can it be achieved?* Nature Reviews Microbiology, 2006. **4**(9): p. 682-695.

33. Kilian, A., et al., *Reliability of malaria microscopy in epidemiological studies: results of quality control.* Tropical Medicine & International Health, 2000. **5**(1): p. 3-8.

34. *Basic malaria microscopy*. 2010. World Health Organization: Geneva.

35. Tangpukdee, N., et al., *Malaria diagnosis: a brief review.* The Korean Journal of Parasitology, 2009. **47**(2): p. 93-102.

36. McArthur, J., *II.— Advances in the design of the inverted prismatic microscope*. Journal of the Royal Microscopical Society, 1945. **65**(1-4): p. 8-16.

37. McArthur, J., *A new concept in microscope design for tropical medicine.* The American Journal of Tropical Medicine and Hygiene, 1958. **7**(4): p. 382-385.

38. McArthur, J.N., *XIII.-A new type of portable microscope.* Journal of the Royal Microscopical Society, 1934. **54**(3): p. 182-185.

39. Richards, J.R., K.A. Gaylor, and A.J. Pilgrim, *Comparison of traditional otoscope to iPhone otoscope in the pediatric ED.* The American Journal of Emergency Medicine, 2015. **33**(8): p. 1089-1092.

40. Dunning, K. and J.R. Stothard, *From the McArthur to the Millennium Health Microscope (MHM): Future Developments in Microscope Miniaturization for International Health.* Microscopy Today, 2007. **15**(2): p. 18-21.

41. Jones, D., et al., *McArthur revisited: fluorescence microscopes for field diagnostics.* Trends in Parasitology, 2007. **23**(10): p. 468-469.

42. Kwon, L., et al., *Medical diagnostics with mobile devices: Comparison of intrinsic and extrinsic sensing.* Biotechnology Advances, 2016. **34**(3): p. 291-304.

43. Switz, N.A., M.V. D'Ambrosio, and D.A. Fletcher, *Low-cost mobile phone microscopy with a reversed mobile phone camera lens.* PloS One, 2014. **9**(5): p. e95330.

44. *Guidelines for the Treatment of Malaria*. 3rd Edition ed. WHO Library Cataloguing-in-Publication Data. 2015, World Health Organization: Geneva.

45. Li, B., et al., *Performance of pfHRP2 versus pLDH antigen rapid diagnostic tests for the detection of Plasmodium falciparum: a systematic review and meta-analysis.* Archives of Medical Science: AMS, 2017. **13**(3): p. 541.

46. *Malaria rapid diagnostic test performance: results of WHO product testing of malaria RDTs: round 8 (2016–2018)*. 2018, World Health Organization: Geneva.

47. Mahende, C., et al., *Performance of rapid diagnostic test, blood-film microscopy and PCR for the diagnosis of malaria infection among febrile children from Korogwe District, Tanzania.* Malaria Journal, 2016. **15**(1): p. 1-7.

48. Batwala, V., P. Magnussen, and F. Nuwaha, *Are rapid diagnostic tests more accurate in diagnosis of plasmodium falciparum malaria compared to microscopy at rural health centres?* Malaria Journal, 2010. **9**(1): p. 349.

49. Hänscheid, T., E. Valadas, and M. Grobusch, *Automated malaria diagnosis using pigment detection.* Parasitology Today, 2000. **16**(12): p. 549-551.

50. Frosch, T., et al., *In situ localization and structural analysis of the malaria pigment hemozoin.* The Journal of Physical Chemistry B, 2007. **111**(37): p. 11047-11056.

51. Coronado, L.M., C.T. Nadovich, and C. Spadafora, *Malarial hemozoin: from target to tool.* Biochimica et Biophysica Acta, 2014. **1840**(6): p. 2032-41.

52. Hanson, K. and C. Goodman, *Testing times: trends in availability, price, and market share of malaria diagnostics in the public and private healthcare sector across eight sub-Saharan African countries from 2009 to 2015.* Malaria Journal, 2017. **16**(1): p. 205.

53. Hänscheid, T., *Diagnosis of malaria: a review of alternatives to conventional microscopy.* Clinical & Laboratory Haematology, 1999. **21**(4): p. 235-245.

54. *Malaria microscopy quality assurance manual-version 2*. 2016: World Health Organization: Geneva.

55. Kawamoto, F., *Rapid diagnosis of malaria by fluorescence microscopy with light microscope and interference filter.* The Lancet, 1991. **337**(8735): p. 200-202.

56. Lowe, B., et al., *Acridine orange fluorescence techniques as alternatives to traditional Giemsa staining for the diagnosis of malaria in developing countries.* Transactions of the Royal Society of Tropical Medicine and Hygiene, 1996. **90**(1): p. 34-36.

57. Guy, R., et al., *The use of fluorescence enhancement to improve the microscopic diagnosis of falciparum malaria.* Malaria Journal, 2007. **6**(1): p. 89.

58. Hassan, S.E.-D.H., et al., *Fluorescence microscope (Cyscope®) for malaria diagnosis in pregnant women in Medani Hospital, Sudan.* Diagnostic Pathology, 2011. **6**(1): p. 1.

59. Lenz, D., et al., *Assessment of LED fluorescence microscopy for the diagnosis of Plasmodium falciparum infections in Gabon.* Malaria Journal, 2011. **10**(1): p. 194.

60. Bray, P.G., et al., *Distribution of acridine orange fluorescence in Plasmodium falciparum-infected erythrocytes and its implications for the evaluation of digestive vacuole pH.* Molecular and Biochemistry Parasitology, 2002. **119**.

61. Keiser, J., et al., *Acridine Orange for malaria diagnosis: its diagnostic performance, its promotion and implementation in Tanzania, and the implications for malaria control.* Annals of Tropical Medicine and Parasitology, 2002. **96**.

62. Wongsrichanalai, C., et al., *Acridine orange fluorescent microscopy and the detection of malaria in populations with low-density parasitemia.* American Journal of Tropical Medicine and Hygiene, 1991. **44**(1): p. 17-20.

63. Xu, L. and A. Chaudhuri, *Plasmodium yoelii: a differential fluorescent technique using Acridine Orange to identify infected erythrocytes and reticulocytes in Duffy knockout mouse.* Experimental Parasitology, 2005. **110**.

64. Caramello, P., et al., *Rapid diagnosis of malaria by use of fluorescent probes.* Diagnostic Microbiology and Infectious Diseases, 1993. **17**.

65. Gwanzura, L., et al., *Evaluation of "Cyscope", a novel fluorescence-based microscopy technique for the detection of malaria.* The Journal of Infection in Developing Countries, 2011. **6**(02): p. 212-215.

66. Ogouyemi-Hounto, A., et al., *[Assessment of a rapid diagnostic test and portable fluorescent microscopy for malaria diagnosis in Cotonou (Benin)].* Bulletin de la Societe de Pathologie Exotique (1990), 2013. **106**(1): p. 27-31.

67. Parsel, S.M., et al., *Malaria over-diagnosis in Cameroon: Diagnostic accuracy of Fluorescence and Staining Technologies (FAST) Malaria Stain and LED microscopy versus Giemsa and bright field microscopy validated by polymerase chain reaction.* Infectious Diseases of Poverty, 2017. **6**(1): p. 1.

68. Srinivasan, S., A.H. Moody, and P.L. Chiodini, *Comparison of blood-film microscopy, the OptiMAL dipstick, Rhodamine-123 fluorescence staining and PCR, for monitoring antimalarial treatment.* Annals of Tropical Medicine and Parasitology, 2000. **94**.

69. Pandey, A.V., et al., *Hemozoin formation in malaria: a two-step process involving histidine-rich proteins and lipids.* Biochemical and Biophysical Research Communications, 2003. **308**(4): p. 736-743.

70. Coronado, L.M., C.T. Nadovich, and C. Spadafora, *Malarial hemozoin: from target to tool.* Biochimica et Biophysica Acta (BBA)-General Subjects, 2014. **1840**(6): p. 2032-2041.

71. Grobusch, M.P., et al., *Sensitivity of hemozoin detection by automated flow cytometry in non-and semi-immune malaria patients.* Cytometry Part B: Clinical Cytometry, 2003. **55**(1): p. 46-51.

72. Kim, K., et al., *High-resolution three-dimensional imaging of red blood cells parasitized by Plasmodium falciparum and in situ hemozoin crystals using optical diffraction tomography.* Journal of Biomedical Optics, 2013. **19**(1): p. 011005.

73. Lawrence, C. and J.A. Olson, *Birefringent hemozoin identifies malaria.* American Journal of Clinical Pathology, 1986. **86**(3): p. 360-363.

74. Lukianova-Hleb, E.Y., et al., *Hemozoin-generated vapor nanobubbles for transdermal reagent-and needle-free detection of malaria.* Proceedings of the National Academy of Sciences, 2014. **111**(3): p. 900-905.

75. Silva, I., et al. *Hemozoin and hemoglobin characterization by optical absorption towards a miniaturized spectrophotometric malaria diagnostic system*. in *Bioengineering (ENBENG), 2017 IEEE 5th Portuguese Meeting on*. 2017. IEEE.

76. Tripathy, U., et al., *Optimization of malaria detection based on third harmonic generation imaging of hemozoin.* Analytical and Bioanalytical Chemistry, 2013. **405**(16): p. 5431-5440.

77. Wilson, B.K., et al., *Detection of malarial byproduct hemozoin utilizing its unique scattering properties.* Optics Express, 2011. **19**(13): p. 12190-12196.

78. Wiseman, P.W., et al., *Haemozoin detection*. 2013, United States Patent and Trademark Office; Patent No. US8423104B2.

79. Shapiro, H.M., et al., *Cytometry in malaria—a practical replacement for microscopy?* Current Protocols in Cytometry, 2013. **65**(1): p. 11.20. 1-11.20. 23.

80. Dharmadhikari, A. K., Basu, H., Dharmadhikari, J. A., Sharma, S., & Mathur, D. (2013). On the birefringence of healthy and malaria-infected red blood cells. Journal of biomedical optics, 18(12), 125001.

81. Li, C., et al., *Integrated quantitative phase and birefringence microscopy for imaging malaria-infected red blood cells.* Journal of Biomedical Optics, 2016. **21**(9): p. 090501.

82. Delahunt, C., et al., *Limitations of haemozoin-based diagnosis of Plasmodium falciparum using dark-field microscopy.* Malaria Journal, 2014. **13**(1): p. 147.

83. Frita, R., et al., *In vivo hemozoin kinetics after clearance of Plasmodium berghei infection in mice.* Malaria Research and Treatment, 2012. **2012**.

84. Hänscheid, T., et al., *Full blood count and haemozoin-containing leukocytes in children with malaria: diagnostic value and association with disease severity.* Malaria Journal, 2008. **7**(1): p. 109.

85. Carneiro, I.A., et al., *Haemoglobin and haematocrit: is the threefold conversion valid for assessing anaemia in malaria-endemic settings?* Malaria Journal, 2007. **6**(1): p. 67.

86. Rebelo, M., et al., *Haemozoin detection in infected erythrocytes for Plasmodium falciparum malaria diagnosis—Prospects and limitations.* Acta Tropica, 2012. **123**(1): p. 58-61.

87. Noland, G.S., N. Briones, and D.J. Sullivan, *The shape and size of hemozoin crystals distinguishes diverse Plasmodium species.* Molecular and Biochemical Parasitology, 2003. **130**(2): p. 91-99.

88. Adewoyin, A., *Peripheral blood film-a review.* Annals of Ibadan Postgraduate Medicine, 2014. **12**(2): p. 71-79.

89. Comar, S.R., M. Malvezzi, and R. Pasquini, *Evaluation of criteria of manual blood smear review following automated complete blood counts in a large university hospital.* Revista Brasileira de Hematologia e Hemoterapia, 2017. **39**(4): p. 306-317.

90. Bain, B.J., *Diagnosis from the blood smear.* New England Journal of Medicine, 2005. **353**(5): p. 498-507.

91. Gulati, G., et al., *Purpose and criteria for blood smear scan, blood smear examination, and blood smear review.* Annals of Laboratory Medicine, 2013. **33**(1): p. 1-7.

92. Kull, J., P. Krawczel, and G. Pighetti, *Evaluation of an automated method for assessing white blood cell concentrations in Holstein dairy cows.* Veterinary Immunology and Immunopathology, 2018. **197**: p. 21-23.

93. Eltoum, I., et al., *Introduction to the theory and practice of fixation of tissues.* Journal of Histotechnology, 2001. **24**(3): p. 173-190.

94. Benattar, L. and G. Flandrin, *Morphometry and quality control for a May-Grunwald Giemsa stained preparation. A 40 centers cooperative study.* Leukemia & Lymphoma, 1999. **33**(5-6): p. 587-591.

95. Rolls, G. *Process of Fixation and the Nature of Fixatives*. Fixation and Fixatives 2012 [cited 2019; Available from: https://www.leicabiosystems.com/knowledge-pathway/fixation-and-fixatives-1-the-process-of-fixation-and-the-nature-of-fixatives/.]

96. Horobin, R., *How Romanowsky stains work and why they remain valuable—including a proposed universal Romanowsky staining mechanism and a rational troubleshooting scheme.* Biotechnic & Histochemistry, 2011. **86**(1): p. 36-51.

97. Houwen, B., *Blood film preparation and staining procedures.* Clinics in Laboratory Medicine, 2002. **22**(1): p. 1-14.

98. Sathpathi, S., et al., *Comparing Leishman and Giemsa staining for the assessment of peripheral blood smear preparations in a malaria-endemic region in India.* Malaria Journal, 2014. **13**(1): p. 512.

99. Singh, H., et al., *Fixation and fixatives: Roles and functions—A short review.* Dental Journal of Advance Studies, 2019. **7**(02): p. 051-055.

100. Horning, M.P., et al., *A paper microfluidic cartridge for automated staining of malaria parasites with an optically transparent microscopy window.* Lab on a Chip, 2014. **14**(12): p. 2040-2046.

101. Amexo, M., et al., *Malaria misdiagnosis: effects on the poor and vulnerable.* The Lancet, 2004. **364**(9448): p. 1896-1898.

102. Wongsrichanalai, C., et al., *A review of malaria diagnostic tools: microscopy and rapid diagnostic test (RDT).* The American Journal of Tropical Medicine and Hygiene, 2007. **77**(6_Suppl): p. 119-127.

103. Hyde, J.E., *Drug-resistant malaria− an insight.* The FEBS Journal, 2007. **274**(18): p. 4688-4698.

104. Antony, H.A. and S.C. Parija, *Antimalarial drug resistance: an overview.* Tropical Parasitology, 2016. **6**(1): p. 30.

105. Simson, E., M. GASCON-LEMA, and D. Brown, *Performance of automated slidemakers and stainers in a working laboratory environment–routine operation and quality control.* International Journal of Laboratory Hematology, 2010. **32**(1p1).

106. *Staining for malaria parasites*, D.o.H.a.H. Services, Editor., Centers for Disease Control and Prevention, Division of Parasitic Diseases: Laboratory Identification of Parasites of Public Health Concern. Accessed at: https://www.cdc.gov/dpdx/diagnosticprocedures/blood/index.html.

107. *Preparation of blood smears*, D.o.H.a.H. Services, Editor., Centers for Disease Control and Prevention, Division of Parasitic Diseases: Laboratory Identification of Parasites of Public Health Concern. Accessed at: https://www.cdc.gov/dpdx/diagnosticprocedures/blood/index.html.

108. Maguire, J.D., et al., *Production and validation of durable, high quality standardized malaria microscopy slides for teaching, testing and quality assurance during an era of declining diagnostic proficiency.* Malaria Journal, 2006. **5**.

109. Becker, H. and L.E. Locascio, *Polymer microfluidic devices.* Talanta, 2002. **56**(2): p. 267-287.

110. Paiè, P., et al., *Microfluidic Based Optical Microscopes on Chip.* Cytometry Part A, 2018. **93**(10): p. 987-996.

111. Whitesides, G.M., *The origins and the future of microfluidics.* Nature, 2006. **442**(7101): p. 368.

112. Wu, J., G. Zheng, and L.M. Lee, *Optical imaging techniques in microfluidics and their applications.* Lab on a Chip, 2012. **12**(19): p. 3566-3575.

113. Duffy, D.C., et al., *Rapid prototyping of microfluidic systems in poly (dimethylsiloxane).* Analytical Chemistry, 1998. **70**(23): p. 4974-4984.

114. Malacara, D., *Optical shop testing*. Vol. 59. 2007: John Wiley & Sons.

115. Hung, K.-Y., et al., *Design and fabrication of a copolymer aspheric bi-convex lens utilizing thermal energy and electrostatic force in a dynamic fluidic.* Optics Express, 2010. **18**(6): p. 6014-6023.

116. Lee, W., et al., *Fabricating low cost and high performance elastomer lenses using hanging droplets.* Biomedical Optics Express, 2014. **5**(5): p. 1626-1635.

117. Sung, Y.-L., et al., *Fabricating optical lenses by inkjet printing and heat-assisted in situ curing of polydimethylsiloxane for smartphone microscopy.* Journal of Biomedical Optics, 2015. **20**(4): p. 047005.

118. Karunakaran, B., et al., *Fabrication of miniature elastomer lenses with programmable liquid mold for smartphone microscopy: curing polydimethylsiloxane with in situ curvature control.* Journal of Biomedical Optics, 2018. **23**(2): p. 025002.

119. Yabu, H. and M. Shimomura, *Simple fabrication of micro lens arrays.* Langmuir, 2005. **21**(5): p. 1709-1711.

120. Pan, L.-W., X. Shen, and L. Lin, *Microplastic lens array fabricated by a hot intrusion process.* Journal of Microelectromechanical Systems, 2004. **13**(6): p. 1063-1071.

121. Wood, R., *The mercury paraboloid as a reflecting telescope.* The Astrophysical Journal, 1909. **29**: p. 164.

122. Hecht, E., *Optics, 4th.* International edition, Addison-Wesley, San Francisco, 2002. **3**.

123. Vaidya, N. and O. Solgaard, *3D printed optics with nanometer scale surface roughness.* Microsystems & Nanoengineering, 2018. **4**(1): p. 1-8.

124. Gibson, B.K., *Liquid Mirror Telescopes-History.* Journal of the Royal Astronomical Society of Canada, 1991. **85**: p. 158.

125. Ninane, N.M. and C.A. Jamar, *Parabolic liquid mirrors in optical shop testing.* Applied Optics, 1996. **35**(31): p. 6131-6139.

126. Borra, E.F., et al. *Liquid mirrors: a progress report*. in *Advanced Technology Optical Telescopes IV*. 1990. International Society for Optics and Photonics.

127. Hickson, P. and R. Racine, *Image Quality of Liquid-Mirror Telescopes.* Publications of the Astronomical Society of the Pacific, 2007. **119**(854): p. 456.

128. Coombs, W. and H. Knoll, *Spincasting contact lenses.* Optical Engineering, 1976. **15**(4): p. 154332.

129. Born, M. and E. Wolf, *Principles of optics: electromagnetic theory of propagation, interference and diffraction of light*. 2013: Elsevier.

130. Fox, R.W., A.T. McDonald, and J.W. Mitchell, *Fox and McDonald's introduction to fluid mechanics*. 2020: John Wiley & Sons.

131. Lakshminarayanan, V. and A. Fleck, *Zernike polynomials: a guide.* Journal of Modern Optics, 2011. **58**(7): p. 545-561.

132. Lubarda, V.A., *The shape of a liquid surface in a uniformly rotating cylinder in the presence of surface tension.* Acta Mechanica, 2013. **224**(7): p. 1365-1382.

133. Turkington, R. and D. Osborne, *On the influence of surface tension on the surface profile of a rotating liquid.* Proceedings of the Physical Society, 1963. **82**(4): p. 614.

134. Burge, J.H., *Introductory Optomechanical Engineering*. University of Arizona. Accessed at: https://wp.optics.arizona.edu/optomech/courses/opti-421521-introductory-optomechanical-engineering/.

135. *Numerical Aperture*. Techniques in Light Microscopy 1/31/2019]; Available from: http://microscopy.berkeley.edu/courses/tlm/optics/na.html.

136. Franklin, G.F., et al., *Feedback control of dynamic systems*. Vol. 4. 2002: Prentice Hall Upper Saddle River.

137. *All About Aspheric Lenses - Custom Aspheric Manufacturing Capabilities*. Available from: https://www.edmundoptics.com/resources/application-notes/optics/all-about-aspheric-lenses/.

138. Meunier, P., et al., *Rotating fluid cylinder subject to weak precession.* Tourbillons et Sillages dans les Fluides Géophysiques, 2008: p. 404.

139. Verzicco, R., et al., *Dynamics of a vortex ring in a rotating fluid.* Journal of Fluid Mechanics, 1996. **317**: p. 215-239.

140. Ghosh, K.K., et al., *Miniaturized integration of a fluorescence microscope.* Nature Methods, 2011. **8**(10): p. 871-878.

141. Miller, A.R., et al., *Portable, battery-operated, low-cost, bright field and fluorescence microscope.* PLoS One, 2010. **5**(8): p. e11890.

142. Schaefer, S., S.A. Boehm, and K.J. Chau, *Automated, portable, low-cost bright-field and fluorescence microscope with autofocus and autoscanning capabilities.* Applied Optics, 2012. **51**(14): p. 2581-2588.

143. Zhang, Y.S., et al., *A cost-effective fluorescence mini-microscope for biomedical applications.* Lab on a Chip, 2015. **15**(18): p. 3661-3669.

144. Breslauer, D.N., et al., *Mobile phone based clinical microscopy for global health applications.* PloS One, 2009. **4**(7): p. e6320.

145. Pirnstill, C.W. and G.L. Coté, *Malaria diagnosis using a mobile phone polarized microscope.* Scientific Reports, 2015. **5**, 13368.

146. Wei, Q., et al., *Plasmonics enhanced smartphone fluorescence microscopy.* Scientific Reports, 2017. **7**(1): p. 2124.

147. Brydegaard, M., et al., *Versatile multispectral microscope based on light emitting diodes.* Review of Scientific Instruments, 2011. **82**(12): p. 123106.

148. Demos, S.G., et al., *Imaging of tissue microstructures using a multimodal microscope design.* IEEE Journal of Selected Topics in Quantum Electronics, 2005. **11**(4): p. 752-758.

149. Salmon, E., et al., *High resolution multimode digital imaging system for mitosis studies in vivo and in vitro.* The Biological Bulletin, 1994. **187**(2): p. 231-232.

150. Nagano, T., Shimizu, K., Kawasaki, K., Kurata, K., & Shimada, M. (2000). U.S. Patent No. 6,025,956. Washington, DC: U.S. Patent and Trademark Office.

151. Li, C. and Y. Zhu. *Dual function microscope for quantitative DIC and birefringence imaging*. in *Three-Dimensional and Multidimensional Microscopy: Image Acquisition and Processing XXIII*. 2016. International Society for Optics and Photonics.

152. Patel, R., et al., *Multimodal optical imaging for detecting breast cancer.* Journal of Biomedical Optics, 2012. **17**(6): p. 066008.

153. Liu, Y., et al., *Complementary fluorescence-polarization microscopy using division-of-focal-plane polarization imaging sensor.* Journal of Biomedical Optics, 2012. **17**(11): p. 116001.

154. Yaroslavsky, A.N. and R.R. Anderson, *Apparatus for imaging a tissue region* (2012). US Patent Application No. US20120170037A1. Washington, DC: United States Patent and Trademark Office.

155. Mach, A.J., O.B. Adeyiga, and D. Di Carlo, *Microfluidic sample preparation for diagnostic cytopathology.* Lab on a Chip, 2013. **13**(6): p. 1011-1026.

156. Kosack, C.S., A.-L. Page, and P.R. Klatser, *A guide to aid the selection of diagnostic tests.* Bulletin of the World Health Organization, 2017. **95**(9): p. 639.

157. Dowling, M. and G. Shute, *A comparative study of thick and thin blood films in the diagnosis of scanty malaria parasitaemia.* Bulletin of the World Health Organization, 1966. **34**(2): p. 249.

158. Trape, J.-F., *Rapid evaluation of malaria parasite density and standardization of thick smear examination for epidemiological investigations.* Transactions of the Royal Society of Tropical Medicine and Hygiene, 1985. **79**(2): p. 181-184.

159. Bejon, P., et al., *Thick blood film examination for Plasmodium falciparum malaria has reduced sensitivity and underestimates parasite density.* Malaria Journal, 2006. **5**(1): p. 104.

160. White, N.J., et al., *Lethal malaria: Marchiafava and Bignami were right.* The Journal of Infectious Diseases, 2013. **208**(2): p. 192-198.

161. Forney, J.R., et al., *Devices for rapid diagnosis of malaria: evaluation of prototype assays that detect Plasmodium falciparum histidine-rich protein 2 and a Plasmodium vivax-specific antigen.* Journal of Clinical Microbiology, 2003. **41**(6): p. 2358-2366.

162. Doolan, D.L., C. Dobaño, and J.K. Baird, *Acquired immunity to malaria.* Clinical Microbiology Reviews, 2009. **22**(1): p. 13-36.

163. Erdogan, T. *Optical Filters Polarization and Filters*. [.pdf] 2011 [cited 2017 12/28/2017]; Presentation File]. Available from: https://www.semrock.com/Data/Sites/1/semrockpdfs/polarizationandfilters.pdf.

164. *Conn's Biological Stains*. 10th ed. 2002, Oxford, UK: BIOS Scientific Publishers Ltd.

165. Kitua, A.Y., et al., *Plasmodium falciparum malaria in the first year of life in an area of intense and perennial transmission.* Tropical Medicine & International Health, 1996. **1**(4): p. 475-484.

166. Smith, T., J.A. Schellenberg, and R. Hayes, *Attributable fraction estimates and case definitions for malaria in endemic.* Statistics in Medicine, 1994. **13**(22): p. 2345-2358.

167. Smith, T., et al., *Absence of seasonal variation in malaria parasitaemia in an area of intense seasonal transmission.* Acta Tropica, 1993. **54**(1): p. 55-72.

168. Modiano, D., et al., *Different response to Plasmodium falciparum malaria in west African sympatric ethnic groups.* Proceedings of the National Academy of Sciences, 1996. **93**(23): p. 13206-13211.

169. Koepfli, C., et al., *Blood-stage parasitaemia and age determine Plasmodium falciparum and P. vivax gametocytaemia in Papua New Guinea.* PLoS One, 2015. **10**(5): p. e0126747.

170. Felger, I., et al., *The dynamics of natural Plasmodium falciparum infections.* PloS One, 2012. **7**(9): p. e45542.

171. Gonçalves, B.P., et al., *Examining the human infectious reservoir for Plasmodium falciparum malaria in areas of differing transmission intensity.* Nature Communications, 2017. **8**(1): p. 1133.

172. Githeko, A., et al., *The reservoir of Plasmodium falciparum malaria in a holoendemic area of western Kenya.* Transactions of the Royal Society of Tropical Medicine and Hygiene, 1992. **86**(4): p. 355-358.

173. Mitran, C.J., et al., *Using Reference Quantitative Polymerase Chain Reaction to Assess the Clinical Performance of the Paracheck-Pf® Rapid Diagnostic Test in a Field Setting in Uganda.* The American Journal of Tropical Medicine and Hygiene, 2018. **99**(2): p. 357-359.

174. Swaroop, S., Gilroy, A. B., Uemura, K., & World Health Organization. (1966). Statistical methods in malaria eradication. World Health Organization: Geneva.

175. Williams, M. *Lab-in-a-Backpack goes to work in Ecuador*. Current News 2010 [cited 2018 18 November 2018]; Available from: http://news.rice.edu/2010/01/13/lab-in-a-backpack-goes-to-work-in-ecuador/.